Identifying Red Giant Progenitors of Hot Subdwarfs in Wide Binaries

---

Diego Benitez

Supervisor: Dr. Maja Vučković (UV)
Internal reviewer: Dr. Mónica Zorotovic (UV)
External reviewer: Dr. Murat Uzundag (KU Leuven)

Tesis para optar al grado de Magíster en Astrofísica
Instituto de Física y Astronomía
Facultad de Ciencias
Universidad de Valparaíso

Noviembre 2024
Valparaíso, Chile.

To Nilda and Nilan, for all the patience, inspiration, and love.

This thesis is solely my own composition,
except where specifically indicated in the text.

Diego Benitez
Noviembre 2024
Valparaíso, Chile.

Acknowledgements

This work is not solely my own; it is the culmination of a long effort, including stressful days and sleepless nights, but also wonderful moments and plenty of joy. I would like to express my deepest gratitude to all the people who made this journey more meaningful and rewarding.

To my friends, both old and new: I cannot list all of your names here, but please know that each of you was essential in helping me move forward, step by step.

To my family: thank you for your patience and understanding with this silly boy who wanted to explore the world. I am sure you missed me as much as I miss you.

I would also like to thank the members of my committee. Your support throughout this process has been invaluable. Thank you for the insightful discussions and thoughtful corrections. What I have learned from you extends beyond academia; you have inspired me profoundly, and I carry those lessons forward into my future.

A special mention goes to Maja, one of the most humble, caring, and kind-hearted people I have ever met, as well as an exceptionally brilliant scientist. Thank you so much for everything.

Finally, I gratefully acknowledge financial support from the Fondecyt Regular through grant 1211941 and Centro de Astrofísica de Valparaíso Proyect Cidi N°21.

Abstract

Modern statistical analyses reveal that up to one-third of observable stars are in binary systems, characterized by two stars orbiting each other. A thorough study of these binaries is essential for understanding the physics of binary interactions. Extensive investigations have associated them with crucial universal phenomena, such as the formation of type Ia supernovae, blue stragglers, hot subdwarfs, cataclysmic variable stars, etc.

Furthermore, binaries offer the unique opportunity to measure stellar masses with high precision, without relying on complex physical models of stellar evolution. Instead, we can apply Kepler's third law, a well-established principle. Thus, we employ these systems to calibrate measurements of stellar masses and mass-luminosity relations, a crucial component of the extragalactic cosmic ladder.

In addition to the fundamental applications mentioned above, binary systems serve as one of the most critical probes of stellar physics. This importance arises from the fact that a companion star can significantly alter the well-established evolutionary track of a single star, thereby prompting us to comprehend new physical phenomena associated with these systems.

This is the case for hot subdwarf B stars (sdBs) which are the naked helium cores of evolved stars, surrounded by a very thin hydrogen envelope, which puzzles researchers, as "canonical" stellar evolution scenarios cannot explain how the star lost almost all of its envelope.

Many evolutionary scenarios to explain the formation of these stars have been proposed over the years, while simultaneously, more and more observational evidence has been gathered. Today we believe that sdBs are solely formed by binary interactions, a topic that will be described in detail in the text.

Observationally, there are more sdB binaries in close systems (orbital periods of a few hours to a few days) compared to wide systems (orbital periods of 400 to 1600 days) because monitoring them with large programs is easier. However, in recent decades, a monitoring program of wide sdB binaries has been initiated. This thesis aims to complement this effort by focusing on the monitoring of progenitors of wide sdB binaries.

The main goal of this thesis is to identify all possible progenitors of sdBs in a volume-limited sample of stars up to 500 pc, which have been monitored by high-resolution spectroscopy, and determine their physical characteristics, such as surface temperature, surface gravity, mass, radius, etc.

Having a sample of progenitors of sdBs in wide binaries will help us to test the predicted correlations between sdB stars and their progenitors, and directly improve the theoretical models that predict the evolution of these fascinating objects.

Contents

List of Figures

List of Tables

Chapter 1

Introduction

Hot subdwarf B (sdB) stars were first observed back in the 1950s by Humason & Zwicky (1947), who reported a few sub-luminous blue stars in the photometric survey of the North Galactic Pole. The number of known objects increased in the next decades in the northern and southern hemispheres thanks to many surveys (e.g. Green et al., 1986; Downes, 1986; Markarian et al., 1989; Wisotzki et al., 1996; Hagen et al., 1995; Napiwotzki et al., 2001; Stepanian, 2005). However, the definition of sdBs comes from Sargent & Searle (1968), who defined an sdB as "A star which has colors corresponding to those of a B star and in which the Balmer lines are abnormally broad for the color, as compared to Population I[1] main-sequence B stars."

Greenstein & Sargent (1974) determined surface temperatures and gravities for sdBs and placed them in the Hertzsprung-Russell diagram (HRD) between the Main Sequence (MS) and the White Dwarf (WD) cooling track. Detail calculations done by Heber et al. (1984); Heber (1986) showed that sdBs are core-Helium-burning stars at the blue end of the Horizontal Branch (HB), the so-called Extreme Horizontal Branch (EHB) as shown in Fig. 1.1. These objects are characterized by an effective temperature in the range of $20000 \lesssim T_{\mathrm{eff}} \lesssim 40000$ K and surface gravities between $5 \lesssim \log g \lesssim 6$.

SdBs are known to be chemically peculiar stars with various abundance anomalies. Among all the peculiarities, the most striking one is their hydrogen content, showing a

---

[1] Population I, or Pop I stars are luminous, hot, and young stars with high metallicity. Population II, or Pop II stars are, on the other hand, less massive, less luminous, cooler old stars with low metallicity.

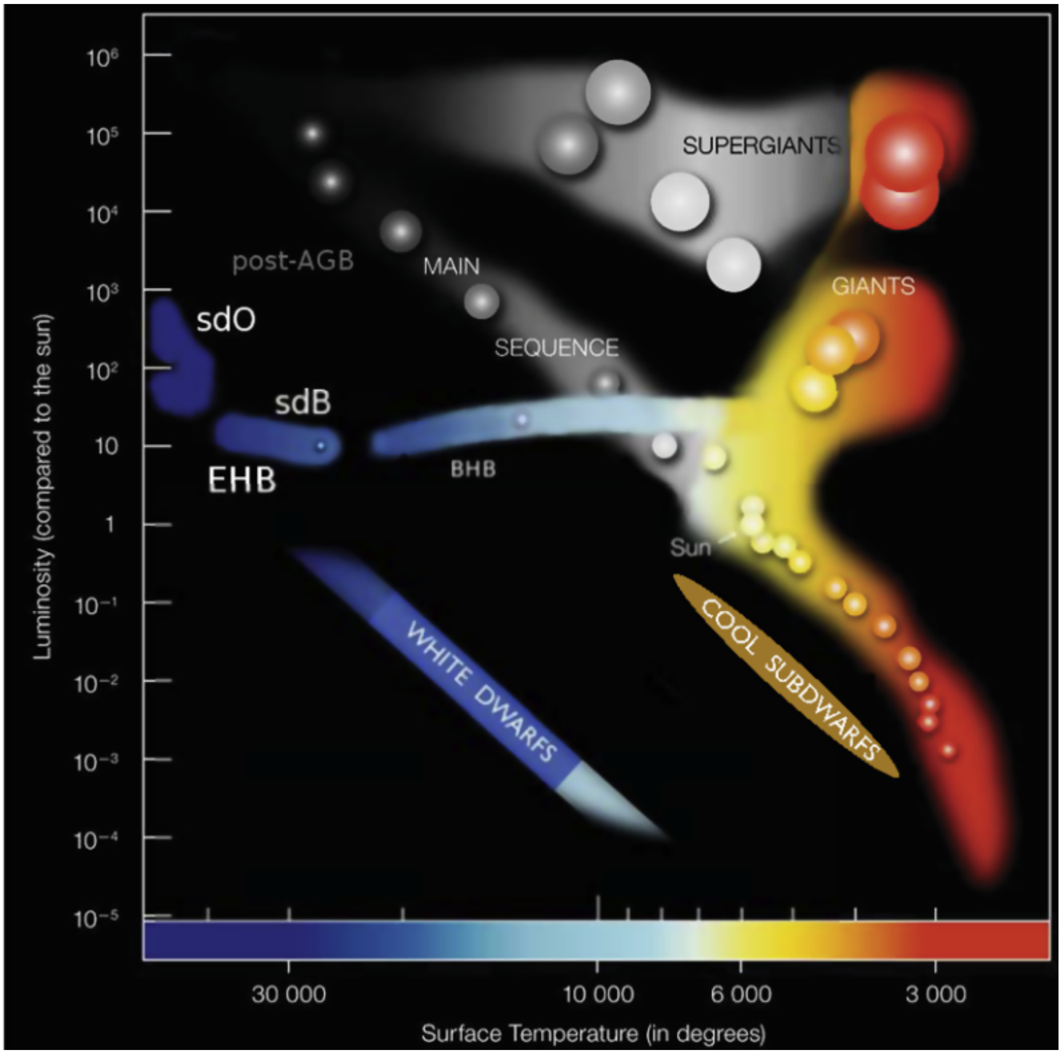

Figure 1.1: HRD showing the position of hot subdwarf stars at the extreme end of the blue horizontal branch. Since EHB stars are less luminous than the corresponding MS B type stars, they are called “subluminous” and because MS stars are typically referred as dwarf stars, EHB stars are also called “subdwarfs”. Figure taken from Heber (2016)

very thin H rich envelope ($< 0.01\,\mathrm{M}_\odot$), which is insufficient to sustain H shell burning. This feature cannot be directly explain by standard evolutionary scenarios, as will be discussed later in this chapter. Apart from hydrogen, helium abundance is also worth mentioning. In fact, the amount of He further divides sdBs into H-sdBs, showing prominent Balmer lines with weak He I lines, and He-sdBs, which also show strong Balmer lines, but are dominated by He I lines and sometimes He II 4686Å is also present. Hotter objects, like sdO stars, are completely dominated by He lines, and there is a transition state called sdOB (Heber, 2016).

The abundance of elements heavier than He was calculated by Geier (2013) in the optical range. It is quite different for H-sdBs and He-sdBs, although overall both populations exhibit traces of carbon, nitrogen, magnesium, silicon, sulfur, and to a lesser extent, iron. Trans-iron elements such as lead can also be found in the UV spectra of many sdBs, enabling the study of neutron-capture processes (Heber, 2016).

Regarding the mass distribution of sdBs, empirical studies based on different methodologies have found similar results. Fontaine et al. (2012) reported a mass range of $\sim 0.35\,\mathrm{M}_{\odot}$ to $\sim 0.62\,\mathrm{M}_{\odot}$ based on asteroseismology[2] of 15 pulsating stars and a somewhat broader distribution, ranging from $\sim 0.29\,\mathrm{M}_{\odot}$ to $\sim 0.62\,\mathrm{M}_{\odot}$, when including seven eclipsing binaries to the sample. In both cases, the distribution has a mean of $0.47\,\mathrm{M}_{\odot}$ which is consistent to the core mass for a solar mass giant at the tip of the Red Giant Branch (RBG) and is called the "canonical" sdB mass $M_{\mathrm{sdB}} \sim 0.47\,\mathrm{M}_{\odot}$.

Schaffenroth et al. (2022) found similar results to those of Fontaine et al. (2012). They studied close binary systems using space-based light curves (brightness variation over time) from the K2 (Howell et al., 2014) and the Transiting Exoplanet Survey Satellite (TESS; Ricker et al., 2015) space mission combined with parallaxes obtained by Gaia (Gaia Collaboration et al., 2016) and parameters from the literature. They derived masses for 39 sdB + low-mass companions and 29 sdB + WD companions. The mass distribution is similarly broad in both cases ($\sim 0.2\,\mathrm{M}_{\odot}$ to $0.8\,\mathrm{M}_{\odot}$) however the peak is located at $0.46\,\mathrm{M}_{\odot}$ for the sdB + low-mass companions and at $0.38\,\mathrm{M}_{\odot}$ for the sdB + WD systems.

Lei et al. (2023) analyzed 664 single-lined sdBs identified in The Large Sky Area Multi-Object Fiber Spectroscopic Telescope spectra survey (LAMOST; Luo et al., 2016). They found a wider distribution (from $\sim 0.1\,\mathrm{M}_{\odot}$ to $\sim 1\,\mathrm{M}_{\odot}$) but with a peak at $0.46\,\mathrm{M}_{\odot}$, which is consistent with the previous works.

While proposed mechanisms are trying to explain the formation of sdBs from the viewpoint of single stellar evolution, they require extremely high metallicity environments to expel almost all the envelope at the tip of the Red Giant Branch (RGB) or predict only massive sdBs (Sweigart, 1997; Castellani & Castellani, 1993; D'Cruz et al., 1996; Brown et al., 2001; Sweigart et al., 2002).

Observational evidence shows that a significant fraction of sdBs are found in close binary systems with WD or cool MS companions (Maxted et al., 2001; Napiwotzki et al., 2004; Copperwheat et al., 2011; Stark & Wade, 2003). Hence, it is essential to consider binary evolution as a potential formation channel for sdBs. Indeed, Pelisoli

---

[2] see Aerts (2021) for a full review in the subject

et al. (2020) argued that binary interaction is always required to form sdBs. This is still debated though (Aubrey & Napiwotzki, 2023).

Many formation channels for sdBs involving binary interactions have been proposed. Han et al. (2002, 2003) explored several of them and their relative importance through binary population synthesis (BPS) studies. They identified three main formation channels that can explain the entire distribution of sdBs, namely, Common Envelope (CE) evolution (Paczynski et al., 1976), stable Roche Lobe Overflow (RLOF) evolution (Han et al., 2002) and double WD merger (Webbink, 1984), accounting for close, wide and single sdBs, respectively. The channels that can form sdBs in binary systems are outlined in Fig. 1.2 and described below.

a) **CE evolution:** A dynamically unstable mass transfer phase leads to the formation of a CE, which results in a short-period sdB + MS binary (left panel in Fig. 1.2). This channel is favored for a high initial mass ratio, that is, the donor is considerably more massive than the accretor. If the naked core of the former giant is massive enough to ignite He after ejecting the envelope, it can become an sdB star. SdB + MS binaries formed through this channel have orbital periods typically ranging from a few hours to a few days (Han et al., 2002), with low-mass (M-dwarfs) MS companions or brown dwarfs.

b) **Stable RLOF:** Long-period sdB stars with MS or subgiant companions are predicted to form after a stable non-conservative mass transfer close to the tip of the RGB (middle panel in Fig. 1.2). This channel is favored for lower initial mass ratios, i.e., initial systems with similar masses during the MS. When enough mass is transferred, the mass ratio is inverted, which increases the orbital period, leading to relatively wide orbits, with periods on the order of years.

c) **Stable RLOF + CE channel:** A combination of the two previous channels is also possible (right panel in Fig. 1.2). First, a low-mass He-core WD is formed due to stable RLOF. Later, the sdB progenitor evolves and also fills its Roche lobe during the RGB phase. Given that the companion is a low-mass He-core WD, the mass ratio in this second mass transfer episode is high enough to ensure dynamically unstable mass transfer, leading to a CE phase that dramatically reduces the orbital period. If the core of the RGB star is massive enough to ignite helium after ejecting the CE, a close sdB + WD binary, with an orbital period of the order of hours, is formed.

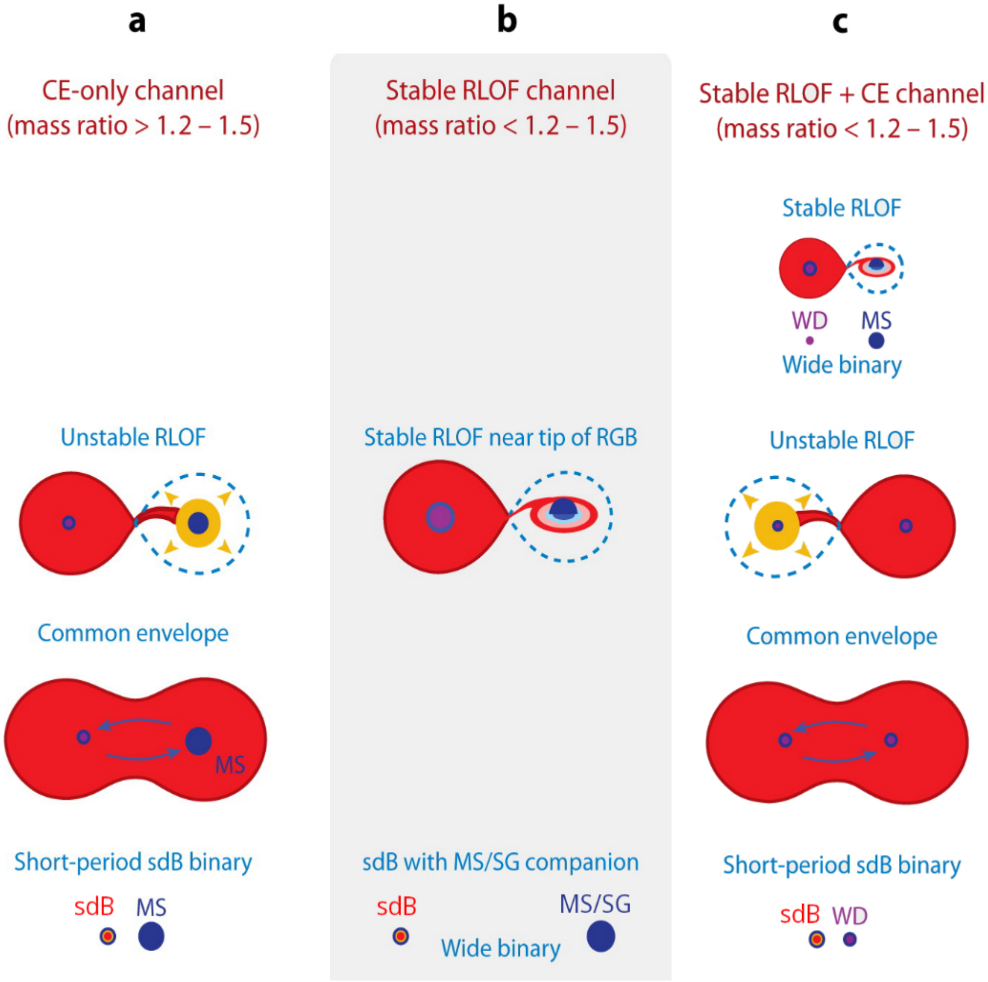

Figure 1.2: Three possible binary sdB formation channels. The evolution of the system proceeds from top to bottom. (a) CE evolution due to unstable RLOF resulting in a short-period sdB + MS binary. (b) Stable RLOF evolution near the tip of the RGB phase of the sdB progenitor, resulting in a long-period sdB binary with a MS or subgiant star companion. (c) Stable RLOF followed by a CE phase, leading the formation of a short-period sdB + WD binary. Adapted from Heber (2016)

d) **Helium WD merger channel:** In this channel, two He WDs formed after either two CE phases or one stable RLOF and a CE (Webbink, 1984). If the period of the system after the second mass transfer phase is short enough, gravitational wave radiation rapidly shrinks the orbit (Taylor et al., 1979) causing the merger. If the merger product ignites helium it results in a fast-rotating single sdB star with a wide mass distribution ($\sim 0.4 - 0.6\,\mathrm{M}_{\odot}$ Han et al., 2002, 2003). This channel is not shown in Fig. 1.2.

The different scenarios have been thoroughly examined based on observational findings, leading to revisions and adjustments to the models proposed by Han et al. (2002, 2003). Geier & Heber (2012) observed that apparent single sdB stars rotate slowly, while Fontaine et al. (2012) obtained a much narrower mass distribution through asteroseismic mass measurements, challenging the feasibility of the double He WD merger scenario in forming single sdBs.

Regarding the CE evolution, Arancibia-Rojas et al. (2024) revisited the models proposed by Han et al. (2002) using an updated version of the stellar evolution code *Modules for Experiments in Stellar Astrophysics* (MESA; Paxton et al., 2011). By refined recipes accounting for metallicity and overshooting effects, they found that lower metallicity models predict slightly more massive sdBs on average. Additionally, they predicted that core overshooting for high-mass progenitors results in a wider mass range compared to the simulations performed by Han et al. (2002). They also found a strong anti-correlation between the sdB mass and the duration of the sdB phase, with lower mass sdBs ($M_{\rm sdB} \sim 0.3\,{\rm M}_\odot$) exhibiting durations up to five times longer than canonical mass sdBs, and at least an order of magnitude longer than more massive sdBs ($M_{\rm sdB} \gtrsim 0.55\,{\rm M}_\odot$). Finally, they suggested that older populations should display a pronounced peak at the canonical mass in BPS simulations, while younger populations should exhibit a less pronounced peak.

Long-period sdB binary observation programs have discovered periods exceeding 1000 days, which are longer than those predicted by Han et al. (2002, 2003) (e.g. Barlow et al., 2012; Deca et al., 2012; Østensen & Van Winckel, 2012; Vos et al., 2012, 2013, 2014, 2017). To address this, Chen et al. (2013) revisited the models of Han et al. (2002) incorporating a more sophisticated treatment of angular momentum loss and atmospheric RLOF. They showed that the final mass – orbital period relation increases with composition, resulting in models with periods up to 1100 days for solar composition and up to 1600 days when atmospheric RLOF is considered.

However, observations of long-period sdB systems also show high eccentricity, indicating a need for improvement in the models. Vos et al. (2015) proposed three eccentricity pumping mechanisms that could be responsible for the observed distribution. While two of these mechanisms (phase-dependent RLOF and interaction between a circumbinary disk and the binary) could potentially result in eccentric binaries, their model fails to reproduce the observed trend between period and eccentricity. Additionally, the orbit must be eccentric prior to mass transfer, with the proposed mechanisms enhancing this eccentricity.

Vos et al. (2019) discovered a correlation between the orbital period and the mass ratio (defined as $M_{\mathrm{sdB}}/M_{\mathrm{MS}}$) in observed wide sdB + MS binaries, indicating lower mass ratios at longer orbital periods. They also identified a correlation between the initial mass ratio at the onset of RLOF and the core mass of the sdB progenitor using theoretical models. This correlation was used to test the stability of the RLOF, assuming that the companion has not accreted any material during RLOF. This assumption, supported by observational evidence (Vos et al., 2018), yielded the range of companion masses and mass ratios at the onset of RLOF to ensure the stability of mass transfer. They concluded that the initial mass ratio decreases with increasing core mass.

A significant step forward in understanding wide sdB systems was taken by Vos et al. (2020). Through a statistically significant BPS study using MESA, they achieved an excellent match with the observed period-mass ratio correlation without explicit parameter tuning. Furthermore, their study revealed a strong agreement with the observed period-metallicity correlation, highlighting the influence of the Milky Way's metallicity history on the properties of post-mass transfer binaries. Additionally, they predicted several new correlations that connect the observed sdB binaries with their progenitors. Here we outline their proposed formation channel for wide sdBs, depicted in Fig. 1.3:

Initially, a MS primary star with a mass between 0.7 and 2.0 $\mathrm{M}_{\odot}$ evolves to the RGB phase, triggering mass transfer through Roche lobe overflow. The secondary star, still on the MS, has a slightly lower mass, and the initial orbital period ranges from 100 to 800 days. Initially eccentric, these binaries circularize before the onset of mass transfer (Vos et al., 2015). The mass transfer rate is low and assumed conservative at the beginning. However, the mass transfer rate quickly increases and exceeds $10^{-5} M_{\odot}\mathrm{yr}^{-1}$, at which point the accretor becomes critically spun up (Popham & Narayan, 1991) and ejects the incoming mass in an outflow (illustrated in Fig. 1.3). Even though the red giant loses all its envelope, its degenerate core ignites helium and becomes a luminous sdB star. The companion MS star accretes only a small amount of mass ($\lesssim 0.05\ M_{\odot}$), but still becomes polluted (MS*).

The radius of the red giant strongly depends on the metallicity of the primary, which correlates with its age and mass due to Galactic evolution. The Galactic metallicity evolution was modeled using a Besanćon model (Robin et al., 2003). A system is considered stable as long as the donor mass-loss rate does not exceed $10^{-2}\ \mathrm{M}_{\odot}\mathrm{yr}^{-1}$; for rates beyond this threshold a CE phase is assumed (Pavlovskii & Ivanova, 2015).

With their model, Vos et al. (2020) found two robust correlations between sdB systems and their progenitors. Firstly, they observed a strong anti-correlation between the final mass ratio ($M_{\mathrm{sdB}}/M_{\mathrm{MS}}$) and the mass of the sdB progenitor. They explained this as follows: Lighter donors tend to have lower-mass companions, whereas heavier donors tend to have higher-mass companions[3]. However, the sdB mass only weakly depends on the initial mass of the progenitor. Additionally, since companions accrete only small amounts of mass, their final masses remain close to their initial masses. Therefore, lighter donors with lower-mass companions result in larger final mass ratios, while heavier donors with higher-mass companions lead to lower final mass ratios.

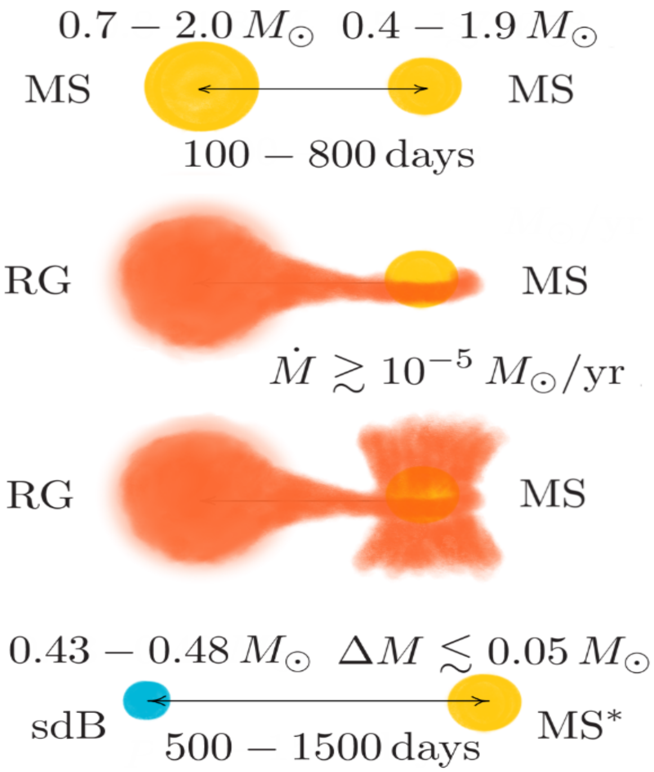

Figure 1.3: Detailed formation channel for wide sdB + MS systems. Taken from Vos et al. (2020)

A second robust correlation exists between the initial orbital period and the final mass ratio. This correlation suggests that systems with larger observed mass ratios originate from those with longer initial orbital periods. Furthermore, for a given observed mass ratio, the initial orbital period also varies with the metallicity of the system. Given that heavier donors generally have higher metallicities, they generate sdB binaries with longer final orbital periods compared to lighter donors. Hence, a correlation

---

[3] This condition is required to maintain $q_i = M_{\mathrm{primary}}/M_{\mathrm{comp}} \lesssim 2.0$. However, this constraint does not apply to other formation channels.

exists between the initial donor mass and the final orbital period.

Based on the effective temperature, surface gravity and radius of the MESA models, Vos et al. (2020) calculated a theoretical color-magnitude diagram for the wide sdB binaries and their progenitors at the moment they start the mass transfer phase (see Fig. 1.4).

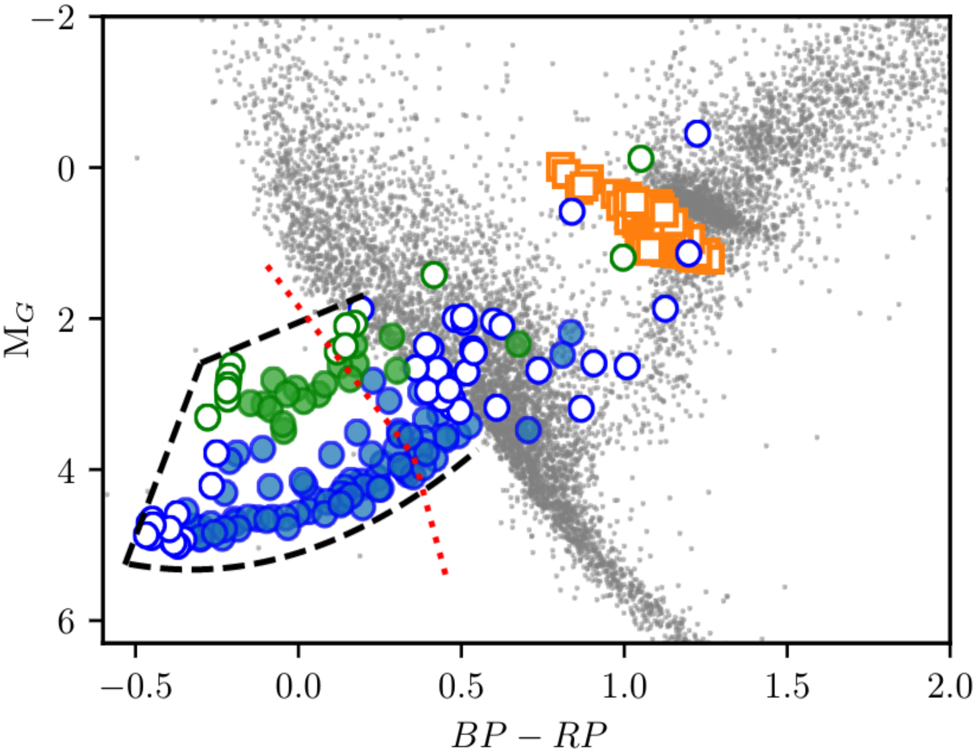

Figure 1.4: Theoretical Gaia color-magnitude diagram for composite (full circles) and single-lined (empty circles) sdB + MS binaries (blue circles), sdA + MS binaries (green circles) and their progenitors at the onset of mass transfer (orange squares). The Gaia color-magnitude diagram of the Hipparcos sample is shown in grey. Taken from Vos et al. (2020)

The predictions made by Vos et al. (2020) offer an opportunity to search for the progenitors of wide sdB + MS binaries. Comparing the population of progenitors with the population of long-period sdB binaries may provide further insights into the details of mass transfer in these systems, as well as on the nature of the observed period-eccentricity relation in long-period systems.

Dawson et al. (2024) have collected the first volume-limited sample of spectroscopically confirmed hot subluminous stars up to 500 pc. Their sample includes 397 members, with 305 identified as hot subdwarf stars. Additionally, Uzundag et al. (2022) initiated observations of sdB progenitors within the same volume as Dawson et al.

(2024). Having the same volume allows for a direct comparison of the properties of sdBs and their progenitors, helping to test theoretical models.

Uzundag et al. (2022) conducted a spectroscopic survey of low-mass red giants before the tip of the RGB using precise parallax measurements from Gaia Data Release 2 (DR2; Gaia Collaboration et al., 2018). They defined a robust binary classification method based on a combination of radial velocity (RV) measurements and astrometric quality indicators from Gaia. Chapter 2 provides a detailed review of their method.

However, Uzundag et al. (2022) conducted only a pilot study, observing targets up to 200 pc. Here, we aim to continue their work by updating the observations, reaching the 500 pc. Additionally, we want to provide a validation of their selected sample. Finally, we want to conduct a comprehensive analysis of the physical properties of the observed long-period sdB progenitors.

Chapter 2

Observations and data reduction

This chapter aims to summarize the observational efforts performed to identify low-mass RG binaries in a volume-limited sample. We begin by describing the target selection criteria and observation strategy, followed by the data reduction tools that we employed, and the classification method developed to detect binaries in the observed sample.

2.1 Target selection

Uzundag et al. (2022) defined a target selection criteria to search for low-mass RGB stars that could be potential progenitors of wide sdB + MS systems. They combined data from Gaia data released 2 (DR2, Gaia Collaboration et al., 2018) with synthetic colors for RGB stars obtained from the MESA Isochrones and Stellar Tracks (MIST; Choi et al., 2016) to select an astrometrically clean subset from Gaia within a volume of 500 pc, based on the recipe described by Lindegren et al. (2018, Appendix C).

Their selected sample is shown in the top panel of Fig. 2.1, where the color cut is defined by the equations

$$G_{\mathrm{abs}} = 2.19(G_{BP} - G_{RP}) - 1.95, \tag{2.1}$$

$$G_{\mathrm{abs}} = 1.86(G_{BP} - G_{RP}) + 0.10, \tag{2.2}$$

$$G_{\mathrm{abs}} = 45(G_{BP} - G_{RP}) - 43.9, \tag{2.3}$$

$$G_{\mathrm{abs}} = 28.33(G_{BP} - G_{RP}) - 38.28. \tag{2.4}$$

where G, G_{BP} and G_{RP} are, respectively, the white, blue and red broad-band passbands of Gaia, with a wavelength coverage of 330—1050 nm, 330—680 nm and 630—1050 nm respectively (Gaia Collaboration et al., 2018), and $G_{\mathrm{abs}} = G + 5\log_{10}(\mathrm{parallax}) + 5$, where the parallax must be in arcseconds.

These criteria target systems that have left the MS but have not yet reached the tip of the RGB. Equations 2.1 and 2.2 establish criteria to eliminate contaminants from the subgiant and HB phase, particularly Red Clump (RC) stars, which are HB stars that overlap with RGB stars in the Color-Magnitude Diagram (CMD). Equations 2.3 and 2.4 define criteria to exclude contaminants with UV and IR excess. UV excess indicates hot stellar objects, particularly WDs, while IR excess suggests the presence of disks and dust. We specifically aim to exclude these systems and focus on low-mass RGB + MS stars. To remove outliers from the sample, Uzundag et al. (2022) cross-matched it with several catalogs (such as GALEX DR5 and WISE; Bianchi et al., 2011; Wright et al., 2010) using TOPCAT (Taylor, 2005). Objects with UV and IR excess were discarded for the reasons previously discussed.

Their final sample contains 2 777 low-mass RGB candidates within 500 pc, covering both the southern and northern hemispheres (bottom panel of Fig. 2.1). However, selecting a sample purely based on photometric constraints suffers from degeneracies, as different stellar properties could produce similar colors. Additionally, photometry does not reveal detailed information such as spectral features, making accurate classification and characterization difficult. On the other hand, spectroscopic data, in particular, high-resolution spectra resolve these issues by allowing not only accurate spectral classification but also precise estimation of stellar parameters.

Hence, a spectroscopic monitoring campaign of stars in the selected sample was initiated in 2019 and is detailed in the next section. Originally, Uzundag et al. (2022) conducted a pilot study, observing a smaller volume sample up to 200 pc. In this thesis, we have further refined their sample and extended the observed volume to 500 pc.

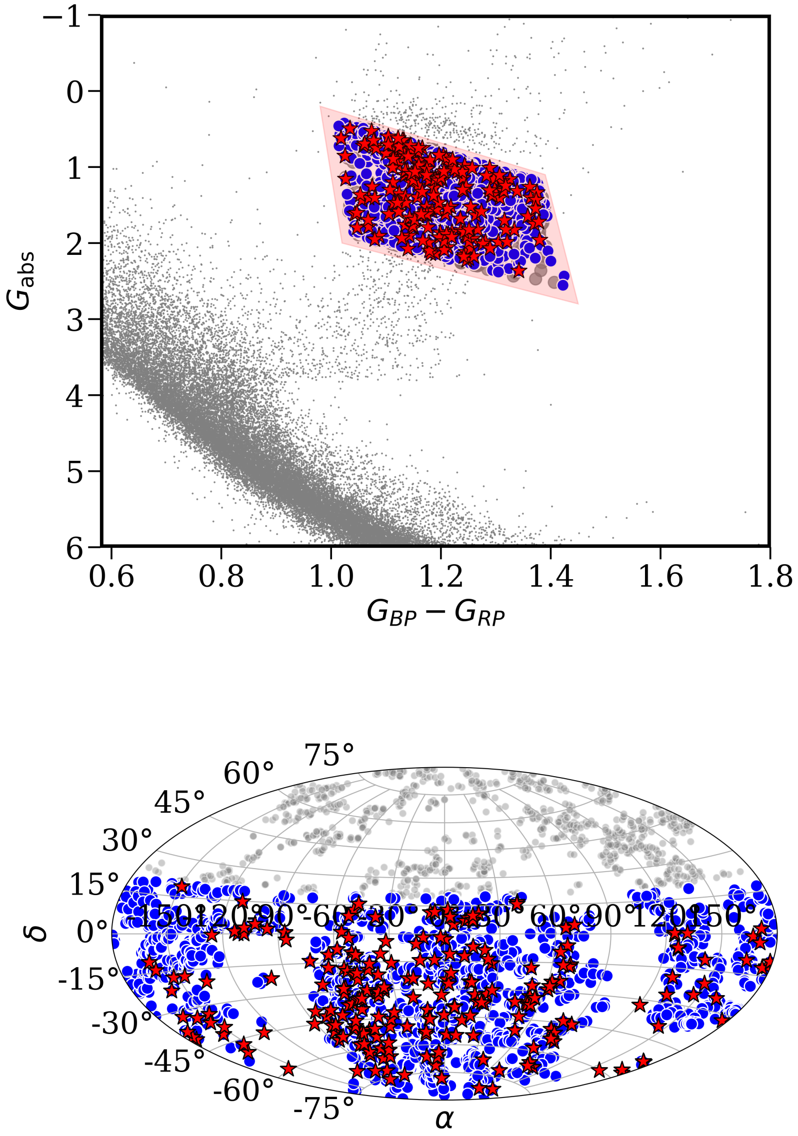

Figure 2.1: Upper panel: CMD of all low-mass (0.7–2.3 $M_\odot$) RG candidates within 500 pc. The CMD of the clean sample from Lindegren et al. (2018) within 100 pc is shown in gray. The slightly larger gray dots within the selected sample represent candidates with $\delta > 20°$, while the blue dots represent the ones with $\delta \leq 20°$. The red stars indicate the already observed low-mass RG candidates. **Lower panel:** Sky locations of the 500 pc volume-limited sample of low-mass RG stars with respect to the galactic coordinate system (Aitoff projection) using the same color coding. Adopted from Uzundag et al. (2022).

2.2 Observations and classification method

The observational campaign was initiated in 2019 using the CORALIE echelle spectrograph (Queloz et al., 2001), mounted on the Swiss 1.2-metre Leonhard Euler Telescope (La Silla, Chile), with a resolving power of $R \equiv \lambda/\Delta\lambda \sim 60\,000$, covering a wavelength range of 3 800Å—6 800Å, and allowing a long-term radial velocity (RV) precision up to 30 ms^{-1} (Queloz et al., 2001). CORALIE is fed by two fibers, one centered on the target, and the other on a reference lamp for wavelength calibration, which can be either a Thorium-Argon (ThAr) lamp or a Fabry-Perot (FP) etalon.

Observations are still ongoing with CORALIE. As of the time of writing this thesis, a total of five observing runs have been conducted, gathering a total of 419 high-resolution spectra for 235 different stars (including 5 RV standard stars[1]). A summary of the observing runs is provided in Table 2.1.

Instrument	Date	Range (Å)	S/N
CORALIE	15-16-17 June 2019	3800-6800	30-80
CORALIE	18-19-20 November 2021	3800-6800	50-100
CORALIE	4 April 2022	3800-6800	40-60
CORALIE	14-16-17 July 2023	3800-6800	10-60
CORALIE	6-7-8-9 October 2023	3800-6800	25-65

Table 2.1: Observing log of the spectroscopic data obtained for the low-mass RG stars studied in this work.

We reduced and analyzed the data using the customized `CERES` pipeline (Brahm et al., 2017), which performs all the extraction processes from basic bias, dark and flat-field corrections (including scattered light) to order tracing, wavelength calibration, and computation of precise RVs using the cross-correlation technique (see Sec. 3.1 for details). For 131 stars, we obtained at least two epoch spectra and measured their RV variations.

To complement our observations, the literature was searched for known low-mass RGB stars applying the criteria described in Sec. 2.1, restricting the orbital period to be in the range of 100 to 900 days. In this way, 33 RGB binary systems were identified in different spectroscopic surveys (Tables 1 and 2 in Uzundag et al., 2022). Some of these

---

[1] An RV standard is a star that exhibits minimal or no RV variation over time. It is used to assess the precision of the instrument or to verify the wavelength calibration.

known binaries were observed with CORALIE, and Uzundag et al. (2022) used them to define criteria for binarity. Additionally, we used them here to show the performance of our data reduction and analysis tools. As an example, their RV calculated using `CERES` are shown in Table 2.2.

We need to identify which stars in the selected sample are part of binary systems. We can achieve this by computing RV variations between different observing epochs, as significant RV variations can indicate the presence of an unseen companion. However, a low RV variation does not necessarily imply that the observed star is single. Consider, for instance, the star HD202470 in Table 2.2; the RV variation for the two observed epochs is quite low ($0.065\ \mathrm{km\,s^{-1}}$) compared to the other stars in the table. However, we know this star is in a binary system. Why is the RV variation so low then? Moreover, how low can the RV variation be to still consider the star to be part of a binary system? We shall address these questions before continuing.

We can estimate the minimum detectable RV variation from purely orbital motion in an orbit with period P, eccentricity e, size a, and inclination i, by interpreting the semi-amplitude K in the RV curve (Hilditch, 2001):

$$K = \frac{v_{\mathrm{r,max}} - v_{\mathrm{r,min}}}{2} = \frac{2\pi a \sin i}{P\sqrt{1-e^2}}, \tag{2.5}$$

as the minimum RV variation we can detect. Using Kepler's third law along with Eq. 2.5 we obtained

$$K = (2\pi G)^{1/3}(M_1 + M_2)^{1/3}P^{-1/3}(1-e^2)^{-1/2}\sin(i). \tag{2.6}$$

The above equation indicates that our minimum detectable RV variation decreases with decreasing inclination, eccentricity and total mass, and increasing period. The most extreme cases would be a face-on orbit ($\sin(i) = 0$) or the most eccentric orbit possible ($e \sim 1$). Therefore, to estimate lower limits in RV variation we assume a very low inclination ($\sin(i) = 0.01$), a circular orbit ($e = 0$), the lowest possible theoretical total mass $M_1 + M_2 = 1.1\,\mathrm{M}_\odot$ (see Fig. 1.3) and the largest searched period (900 days), which gives $K \sim 0.2\ \mathrm{km\,s^{-1}}$. However, CORALIE is sensitive to detect RV variations two orders of magnitude lower.

While it is possible to detect lower RV variations than the estimated value, associating them with orbital motion is questionable. Indeed, using G and K giants with periods greater than 100 days, Setiawan et al. (2004) argued that RV variations lower than $0.8\ \mathrm{km\,s^{-1}}$ could be better explained by other sources of variability, such as surface inhomogeneities (spots), pulsations, or sub-stellar companions. Consequently, Uzundag et al. (2022) established a threshold of RV variation greater than 0.1 km/s to consider the star a potential binary candidate. However, HD202470 exhibits an RV variation lower than this threshold. This can still be explained, for example, by an extremely low inclination or by the possibility that the second spectrum of this star was taken at an orbital phase very close to the first epoch, resulting in the star having almost the same RV in both measurements. We can investigate the latter possibility using the definition of phase:

$$\phi = \frac{t - T_0}{P} - \left[\frac{t - T_0}{P}\right] \tag{2.7}$$

where t is the time of a given measurement, T_0 is a reference time, P is the period and the brackets denote the integer part. For HD202470, the measurements were taken in $t_1 = 2459739.82$ JD and $t_2 = 2460140.63$ JD. Using t as t_2, T_0 as t_1, and $P = 488$ d, we calculate the phase of the second measurement as $\phi \approx 0.82$. Therefore, it was taken close in phase relative to the first measurement ($\Delta\phi \approx$0.18), leading to a similar RV for such a long period.

This strongly indicates that setting a threshold solely on RV variation is not sufficient to confirm binarity. Hence, Uzundag et al. (2022) proposed using the Renormalized Unit Weight Error (RUWE) and Astrometric Excess Noise (AEN) from Gaia. The former is used to filter out sources with potentially poor astrometry, in particular, spurious parallaxes or proper motions, while the latter measures the residuals in the five-parameter astrometric solution for the source (Lindegren et al., 2018). These two parameters have been previously used to indicate the presence of unresolved companions (see, for instance, Gandhi et al., 2022).

For single stars, values of the AEN are expected to be close to 0, while RUWE values are expected to be around 1.0. Uzundag et al. (2022) analyzed the AEN and RUWE values of the known binary systems and discovered that more than 90% of them have AEN ≥ 0.4 and more than 93% of them have RUWE ≥ 1.4. Therefore they used those values as thresholds.

Using the defined thresholds, namely, ΔRV ≥ 0.1 km s^{-1}, RUWE ≥ 1.4 and AEN ≥ 0.4, Uzundag et al. (2022) suggested a robust binary classification method:

- If at least two of the three parameters satisfy the threshold, the star is classified with the highest probability of being part of a binary system (1).

Star	RUWE	AEN	Category	JD -2450000	SNR	RV ($\mathrm{km\,s^{-1}}$)	RV Error ($\mathrm{km\,s^{-1}}$)	$\Delta\mathrm{RV}_{\mathrm{max}}$ ($\mathrm{km\,s^{-1}}$)
HD116338	1.445	0.211	1	8651.59	37	-30.528	0.004	6.192
				9673.73	43	-29.169	0.003	
				9737.70	62	-34.554	0.003	
				10140.55	62	-28.362	0.004	
HD36787	3.83	0.697	1	9537.71	61	53.483	0.003	3.015
				9673.50	32	52.634	0.003	
				10140.92	64	50.468	0.004	
HD9525	6.283	2.996	1	9538.58	60	12.333	0.004	1.422
				9739.93	63	12.478	0.004	
				10140.87	39	11.056	0.005	
HD190574	4.008	0.502	1	9738.93	52	22.455	0.003	3.652
				10140.61	37	26.107	0.004	
HD202470	1.888	0.345	2	9739.82	63	26.704	0.003	0.065
				10140.63	39	26.769	0.004	
HD2132	11.862	1.902	1	9537.54	57	49.697	0.003	8.458
				10140.84	38	41.239	0.004	
HD8410	9.195	1.325	1	9537.61	38	5.836	0.003	0.713
				10140.86	71	5.123	0.004	

Table 2.2: Radial velocities computed using `CERES` of known binary systems found by Uzundag et al. (2022). Observations were taken with CORALIE. RUWE and AEN values were obtained from Gaia. Stars are classified according to the definition in Uzundag et al. (2022). The last column shows the largest RV variation between different observed epochs. Note that the errors reported are formal statistical errors computed by `CERES` (see Sec. 3.1).

- If only one of the three parameters satisfies the threshold, the star is classified with a moderate probability of being part of a binary system (2).
- If none of the parameters satisfy the threshold, the star is classified with the lowest probability of being part of a binary system (3).

Following this classification method, stars categorized as 1 or 2 are considered potential binaries, and RV monitoring with CORALIE was continued during this thesis work. It will continue until the orbital periods of the confirmed binaries are determined. Given that stars classified as 3 may also be binaries (e.g., with low inclinations), they will be observed in the future, but with lower priority.

The complete sample of 2 777 low-mass RG candidates within 500 pc was further filtered out using the above-mentioned classification method, which resulted in a total of 193 top-priority binary candidates (i.e., classified as 1 or 2) among the stars observable with CORALIE ($\delta \leq 20°$). Our observation strategy involved collecting a first epoch spectra for all the targets up to 500 pc, followed by at least two additional epochs with a minimum separation of two months. This is necessary considering that we are searching for long-period systems.

2.3 Data reduction

The data reduction process is crucial for ensuring the accuracy and consistency of RV measurements, as well as for subsequent analyses involving the determination of physical properties. However, reducing data obtained from echelle spectrographs presents challenges due to the instrumental complexities. Echelle spectrographs introduce various instrumental artifacts, such as order tracing, order overlap, line bending, variable order intensities due to wavelength-dependent instrument efficiency, and scattered light.

These complexities can lead to inconsistencies in data reduction across different instruments and even when handled by different individuals using the same instrument. To avoid such discrepancies, we opted to use an automated modular code known as the Collection of Elemental Routines for Echelle Spectra (`CERES`, Brahm et al. (2017)). Mainly written in Python, `CERES` provides dedicated reduction pipelines for 13 different spectrographs, including CORALIE. The processing workflow for fiber-fed spectrographs is summarized in Figure 2.2 and detailed below. Further details regarding the RV computation are provided in Sec. 3.1.

After classifying the different input images (bias frames, dark frames, flat frames, wavelength calibration frames, and science images), `CERES` constructs the master CCD calibration images through median combination. However, for fiber-fed spectrographs, flat-field correction is not attempted due to the complexity of illuminating the border regions of each echelle order with high intensity. Instead, `CERES` co-adds the spectrum from a reference continuum lamp (ThAr lamp in the case of CORALIE) to produce the master fiber-flat, which is also used to identify and trace the orders. The algorithm then subtracts the bias and dark frames from both, the master fiber-flat and science images, and divides the science images by the normalized master fiber-flat.

To find the orders, the pipeline selects the central columns of the master fiber-flat

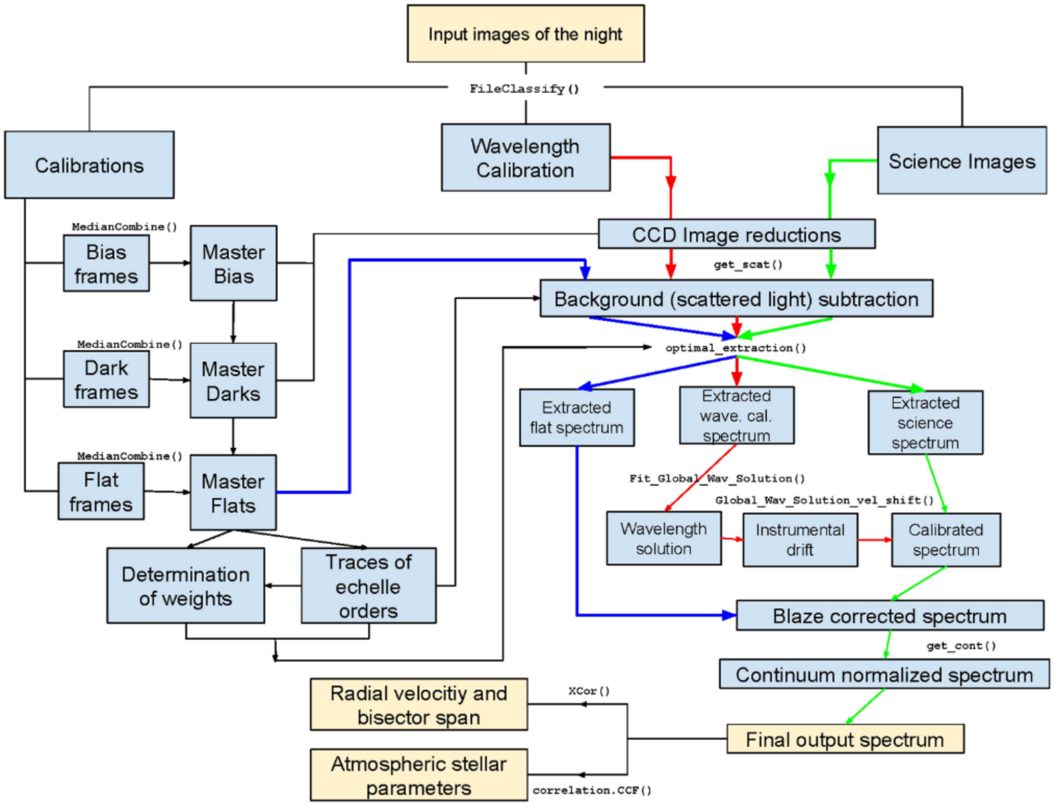

Figure 2.2: Flow diagram illustrating the images and processes generally used by the `CERES` pipelines for fiber-fed spectrographs. The most important functions at each step are also shown. Taken from Brahm et al. (2017)

(width of 10 pixels by default, which can be changed by the user), median combines them along the dispersion direction and convolves this reference column with a Gaussian kernel to smooth it. The peaks of the Gaussian correspond to the selected orders. However, an iterative procedure is applied to reject shallow peaks with counts smaller than N times the dispersion of the counts in the inter-order zones (where the width of the Gaussian and N are also adjustable parameters). Further cleaning is done by fitting a Gaussian to regions centered on the positions adjacent to the already identified order centers, thus identifying the vertical position of the orders in each column. A rejection algorithm is applied to avoid errors in the order tracing due to low S/N, cosmic rays, or instrumental artifacts. Finally, a high-order polynomial is fitted to the centroids computed for each order, and the coefficients of this fit are saved for extracting the science and calibration spectra.

An additional step for data reduction when working with echelle spectrographs comes from the scattered light generated by the echelle grating and the roughness of the optical surface. `CERES` corrects this effect by computing the median flux in each inter-order region and interpolating these values in the cross-dispersion direction. This procedure leads to a 2D map of the scattered light, and the pipeline applies a 2D median filter to smooth the effects of spurious signals. Finally, the filtered image is subtracted from each original science image.

The next step is to add up all the signal around the trace in the direction perpendicular to the dispersion, going thus from a 2D image to a 1D spectrum. `CERES` does this for each order using either a "rectangular extraction" algorithm (it sums the flux of all the pixels contained in a vertical window of width defined by the user) or a more complex "optimal extraction" algorithm (Horne, 1986). We chose to use the optimal extraction for this work.

For wavelength calibrations, a FP spectrum is taken simultaneously with the science image by CORALIE. However, FP interferometers do not directly deliver an absolute wavelength calibration; this is done with the spectrum from a ThAr lamp obtained before the beginning of the observations. The wavelength solution is then refined with the acquisition of a FP spectrum. `CERES` includes the functions required for handling FP calibration spectra. In the case of CORALIE, three images are required: the ThAr lamp at both fibers (TH2), the ThAr lamp at the object fiber while the FP is at the comparison fiber (THFP), and the stellar spectrum at the object fiber while the FP is at the comparison fiber (OBFP). The global absolute wavelength solution is computed for both fibers using the reduced spectrum of TH2. Then, the FP spectrum of the comparison fiber in THFP is calibrated in wavelength by computing the instrumental drift between the ThAr spectra of the TH2 and THFP images. Finally, the instrumental drift between the THFP and the OBFP images is calculated by computing the cross-correlation function between both FP spectra.

Another correction that has to be made is for the strong instrumental modulation, known as the blaze function. It is produced due to interferences in the echelle grating and therefore depends on its blaze angle[2]. `CERES` employs the fiber flat frames to correct this effect in fiber-fed spectrographs. After correcting for scattered light, the master fiber flat frame is extracted following the same procedure used for the science spectra, and then each extracted order of the flat frame is normalized by its maximum. This normalized flat spectrum is assumed to represent an approximation of the blaze function. The correction for the blaze function of the science spectra is performed by dividing the extracted spectrum of each order by the corresponding normalized flat spectrum. This

---

[2] For CORALIE $\tan\phi = 4$, where ϕ is the blaze angle.

procedure also corrects for the column-averaged pixel-to-pixel variations of the CCD.

Finally, the continuum normalization is obtained by fitting a low-order polynomial to the deblazed flux, including an iterative procedure that excludes absorption lines from the fit. The S/N is estimated by combining the contribution of (i) the expected Poisson error at each pixel given the extracted flux, (ii) the readout noise, and (iii) the expected Poisson error at each pixel produced by the scattered light.

The final `CERES` output is a 3D fits file with the general form `[data type, echelle order, pixel]`. The `data type` dimension has the following entries:

0. Matrix with the wavelengths of each pixel for each echelle order after computing all the instrumental velocity drifts.
1. Optimally extracted stellar flux
2. Error associated with the extracted flux (inverse variance).
3. Deblazed stellar flux.
4. Errors from the previous entry.
5. Continuum normalized flux
6. Errors from the previous entry.
7. Estimated continuum
8. Signal-to-noise ratio

We present the continuum-normalized flux of several orders obtained by `CERES` for the star HD202470 in Fig. 2.3. The top panel reveals that the initial orders exhibit low S/N, a common characteristic of echelle spectrographs, as they are optimized for higher S/N in the central orders. However, this poses no issue for our study, as the early orders of CORALIE lie within the near-UV region, whereas our focus lies primarily in the optical range of the spectra. Here, significantly higher S/N is observed, allowing for the identification of numerous spectral lines, as depicted in the middle panel of Fig. 2.3. The lower panel displays prominent telluric features, an anticipated outcome given the unavoidable influence of Earth's atmosphere.

In Figure 2.4, we present the continuum-normalized flux of all CORALIE orders for the star HD202470. Although `CERES` does not include the merged spectrum in its final output, it can be achieved using other programs. However, we chose to perform this process ourselves. To construct Figure 2.4, we interpolated the flux of adjacent orders using a Cubic Spline function and applied a rejection method based on the S/N. This procedure was repeated for the normalized flux. Finally, errors were propagated to determine the final S/N at each point.

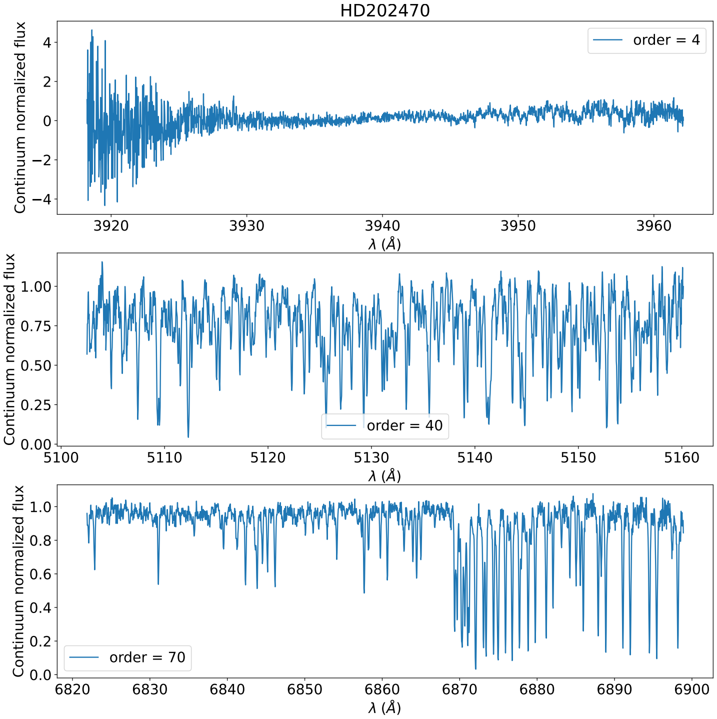

Figure 2.3: Comparison between different orders after the data reduction using `CERES` for the star HD202470. Top panel: Comparatively low S/N in the near-UV. Central panel: The middle orders of the spectrum show the highest S/N. Lower panel: Strong absorption lines from the Earth's atmosphere.

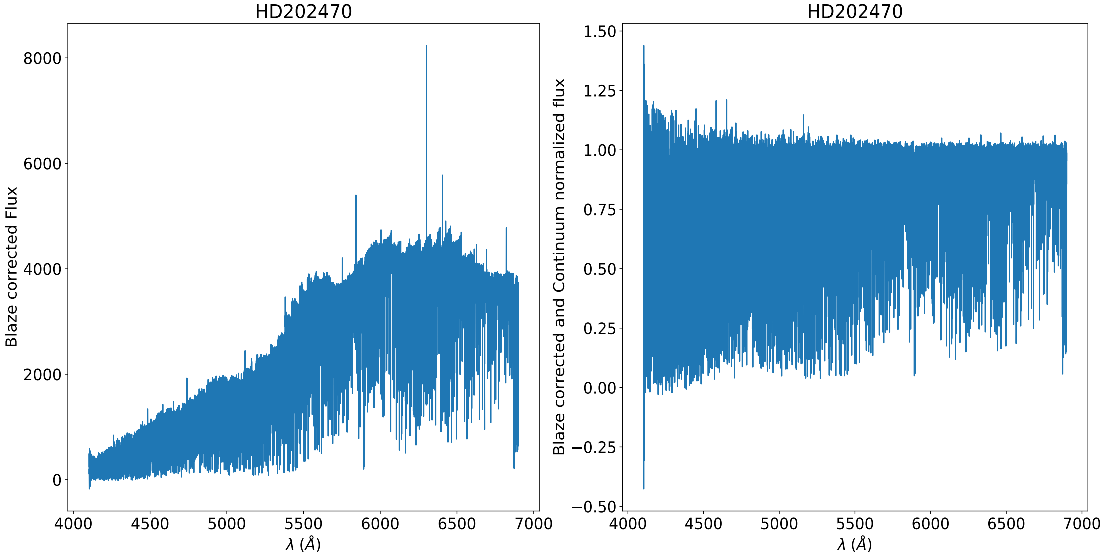

(a) Deblazed merged spectrum

(b) Continuum normalized spectrum

Figure 2.4: Merged spectrum for star HD202470, the first 10 orders are avoided due to the low S/N.

Chapter 3

Methods

In this chapter, we outline the derivation of RVs using `CERES`, as well as atmospheric and physical parameters for each observed star, alongside their distribution. Various derivation methods yield systematic discrepancies in these parameters. To ensure consistency across all measurements, we adopt the specialized pipeline known as Spectroscopic Parameters and atmosphEric ChemIstriEs of Stars (`SPECIES`; Soto & Jenkins, 2018; Soto et al., 2021). We provide a comprehensive overview of the code.

3.1 Radial velocity

`CERES` employs the cross-correlation function (CCF) technique (Griffin, 1967) to compute the RVs. The CCF is calculated for each extracted order using three available stellar masks (G2, K5, and M5), with the G2 mask being employed for all our targets. These masks assign values of 1 to regions where typical stellar spectra exhibit narrow absorption lines, and 0 elsewhere. `CERES` combines the CCF for each order through a weighted sum based on the median SNR of each order.

The CCF for the m-th order, with wavelength coverage from λ_i to λ_f, at a specific velocity v, is given by (Brahm et al., 2017):

$$CCF^m(v) = \frac{\int_{\lambda_i}^{\lambda_f} W(\lambda')F(\lambda)M(\lambda')d\lambda}{\sqrt{\int_{\lambda_i}^{\lambda f} W(\lambda')M(\lambda')^2 d\lambda}}, \tag{3.1}$$

where $F(\lambda)$ corresponds to the observed spectrum and $M(\lambda')$ to the selected mask shifted to the $\lambda' = \lambda\left(1+\frac{v}{c}\right)$ wavelength positions due to the Doppler displacement, where c represents the speed of light. Finally, $W(\lambda')$ corresponds to the weight assigned to each spectral zone according to the mask.

The CCF reaches its minimum value near the RV of the observed star. The actual RV is determined by fitting a Gaussian to the CCF, with the resulting mean considered as the RV of the star. A typical CCF for the star HD202470 is depicted in Fig. 3.1.

The uncertainties in the RVs are computed using empirical scaling relations derived from Monte Carlo simulations, incorporating the mean S/N near the Mg triplet zone as priors. These scaling relations are combined with the dispersion of the Gaussian fit to the CCF, σ_{ccf}, and the continuum S/N at 5130 Å, denoted as SN_{5130}. The exact equation is given by (Brahm et al., 2017):

$$\text{RV error} = b + \frac{a(1.6 + 0.2\sigma_{ccf})}{SN_{5130}}, \tag{3.2}$$

where a and b are the scaling parameters found with the Monte Carlo simulations.

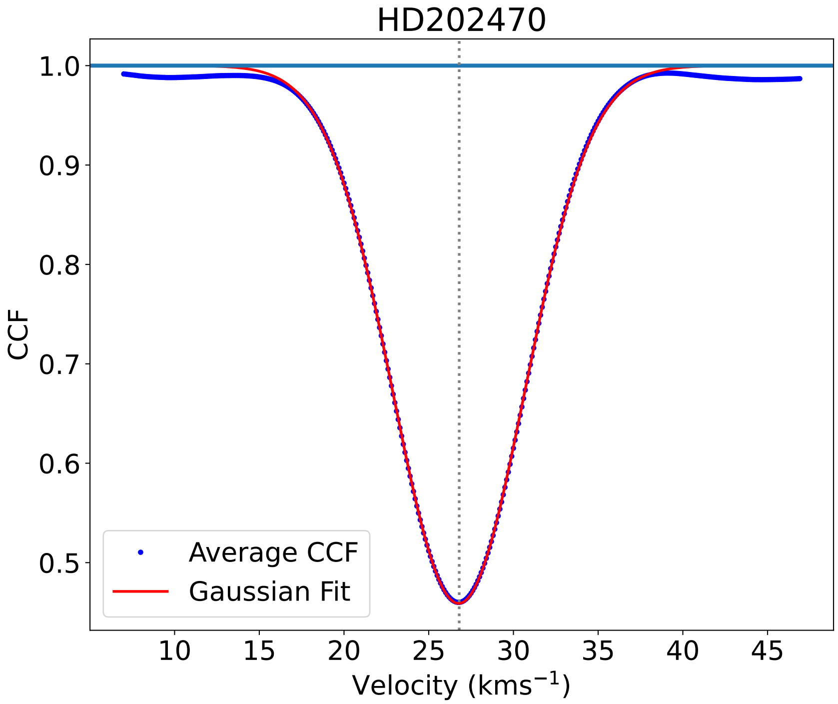

Figure 3.1: A typical cross-correlation function fit obtained with the `CERES` pipeline for the star HD202470. The mean of the Gaussian fit is taken to be the RV of the object.

3.2 Derivation of stellar parameters

We derived stellar parameters using `SPECIES`, a publicly available[1] code mostly written in Python, which uses high-resolution echelle spectra to estimate both atmospheric and physical parameters consistently and uniformly. It offers capabilities for determining effective temperature (T_{eff}), surface gravity ($\log g$), metallicity ([Fe/H]), microturbulent velocity (ξ_t), projected rotational velocity ($v \sin i$), macroturbulence velocity (v_{mac}), stellar mass, age, radius, and photometric surface gravity, as well as chemical abundances for 11 additional atomic elements. However, for our analysis, we chose not to calculate these additional abundances. The uncertainties associated with each parameter were computed consistently, addressing parameter correlations and propagating uncertainties accordingly.

3.2.1 Initial parameters

The code requires photometric and astrometric data as priors, which users can input manually. Alternatively, it uses parallaxes and proper motions from either Gaia DR2 (Gaia Collaboration et al., 2018) or the Hipparcos mission (van Leeuwen, 2007), while magnitudes in various bands are gathered from multiple surveys. Included bands are 2MASS JHK, *Tycho-2* $(\text{BV})_t$, Strömgren $b-y$, m_1, c_1 and Johnson BV(RI)_c.

The magnitudes are corrected for dust extinction using the `mwdust` python package (Bovy et al., 2016) and systematic corrections are applied to parallaxes from Gaia DR2 (Stassun & Torres, 2018).

Parallaxes and proper motions are used to estimate the evolutionary state of the stars following the classification scheme outlined in Collier Cameron et al. (2007). When classified as a giant, the temperature estimation follows the relationships provided by Alonso et al. (1999):

$$\frac{5\,040}{T_{\text{eff}}} = a_0 + a_1 X + a_2 X^2 - a_3 X[\text{Fe/H}] + a_4[\text{Fe/H}] + a_5[\text{Fe/H}]^2, \tag{3.3}$$

where X is a color index. Values for the coefficients using different colors are given in Tab. 2 of Alonso et al. (1999). The above equation was obtained using intrinsic colors of giants in the ranges $3\,500\text{ K} < T_{\text{eff}} < 8\,000\text{ K}$ and $-3.0 \leq [\text{Fe/H}] \leq +0.5$.

The initial $\log g$ is estimated as the minimum value between 3.5 and Eq. 3.4 (Soto & Jenkins, 2018)

---

[1] `https://github.com/msotov/SPECIES/wiki`

$$\log g = -2.8 \times 10^{-7} T^2 + 3.79 \times 10^{-3} T - 9.335. \tag{3.4}$$

Finally, the initial metallicity is set to zero for all stars classified as giants.

3.2.2 Atmospheric parameters

The code employs the equivalent widths (EWs) of Fe I and Fe II lines together with the 2017 version of `MOOG` (Sneden et al., 2012) and ATLAS9 model atmospheres (Castelli & Kurucz, 2003) to solve the radiative transfer equation under local thermodynamic equilibrium (LTE). Subsequently, it derives the effective temperature, surface gravity, metallicity, and microturbulent velocity.

The computation of EWs involves selecting a 3 Å-wide region around the line, normalizing the spectrum using a second-degree polynomial fit, and removing outliers based on S/N. Absorption lines within this region are identified by detecting regions where the derivative is zero and the second-degree derivative is positive (local minimum condition).

A Gaussian profile is subsequently fitted to the identified absorption lines, with the condition that uncertainties for all Gaussian parameters (normalization constant, mean, and standard deviation) remain below 0.12 dex. This restriction aids in identifying and fitting blended lines. We show the EW computation of the blended line Fe I 6297.80 Å for the star HD202470 in Fig. 3.2

The EW values, along with an interpolated atmosphere model obtained from a grid of ATLAS9 models (Castelli & Kurucz, 2003), are provided to the 2017 version of the MOOG code (Sneden et al., 2012). Using the *abfind* driver, the code addresses the radiative transfer equation under LTE conditions and adjusts species abundances to match computed equivalent widths with previously measured ones. Subsequently, the atmospheric parameters (T_{eff}, $\log g$, [Fe/H], and ξ_t) are determined iteratively. This process concludes when: (1) there is no correlation between individual Fe I line abundances with the excitation potential and the reduced equivalent width (EW/λ); (2) the average abundance of Fe I and Fe II matches; and (3) the Fe I abundance obtained aligns with that used to generate the model atmosphere of that iteration (Gray, 2005).

The uncertainty in the atmospheric parameters is estimated as follows:

- For the microturbulent velocity, it is determined as the value at which the slope of the linear fit performed between the individual Fe I abundances and the reduced equivalent width reaches zero.

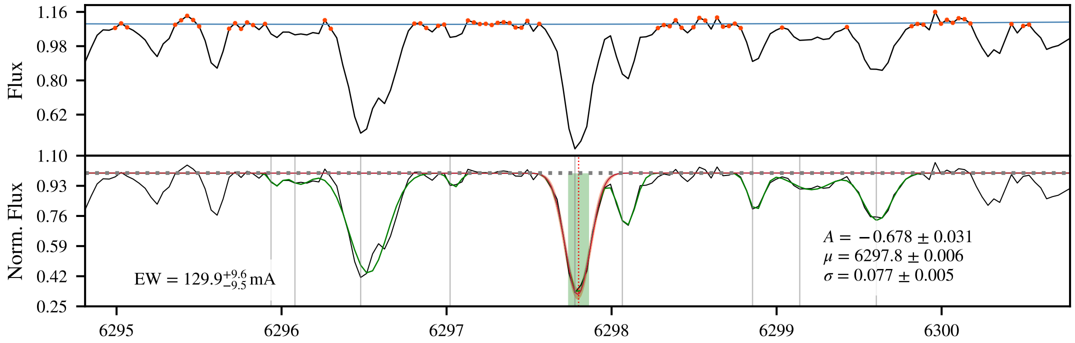

Figure 3.2: Fit performed using `SPECIES` to the blended line Fe I 6297.80 Å for the star HD202470 from a CORALIE observation. The upper panel shows the observed spectral region with the points used to estimate the continuum mark in red. The lower panel shows the normalized spectra with the detected absorption lines (gray vertical lines), the global fit (green line), and the fitted line (red line). The green block represents the EW, which is also quoted in the lower left corner of the panel. The parameters of the Gaussian fit to the line with their respective uncertainties are also shown.

- In the case of temperature, it is the value at which the slope of the dependence between the individual Fe I abundances and the excitation potential becomes zero. However, this determination is influenced by the uncertainty in microturbulent velocity, as all atmospheric parameters are derived simultaneously, and thus the uncertainty in temperature is propagated with the error in microturbulent velocity.

- The uncertainty in surface gravity is determined from the spread of the average abundance obtained for the Fe II lines, incorporating the propagated uncertainty from the final temperature determination.

- Finally, the uncertainty in metallicity is computed as the spread of abundances from the Fe I lines when the individual Fe I abundances match that of the input model atmosphere. These uncertainties are propagated to account for variations in microturbulent velocity and temperature.

As an illustration, we show the atmospheric parameters computing using `SPECIES` for the stars known to be in binary systems in Table 3.1. However, not all of these systems were observed with CORALIE. We searched for high-resolution spectra of the stars not observed with CORALIE in the European Southern Observatory (ESO) archive[2] to perform the computation. In cases where stars were observed multiple times, we selected the observation with the highest S/N.

Starname	Instrument	$T_{\rm eff}$ (K)	$\log g$ (cms^{-2})	[Fe/H] (dex)	ξ_t (kms^{-1})
HD5877	FEROS	4698±50	2.9±0.1	-0.02±0.04	1.14±0.06
HD14355	FEROS	4972±50	3.46±0.08	0.12±0.04	1.02±0.05
HD153438	FEROS	4834±50	2.95±0.10	0.04±0.04	1.21±0.05
HD179799	FEROS	4933±50	3.19±0.07	-0.06±0.04	1.09±0.04
HD27697	FEROS	5139±50	2.8±0.1	0.18±0.04	1.57±0.05
HD32008	FEROS	5390±50	3.50±0.07	-0.14±0.04	1.14±0.04
HD62644	UVES	5534±50	3.87±0.07	0.09±0.04	0.94±0.05
HD133166	FEROS	4780±79	3.3±0.2	0.43±0.04	1.0±0.2
HD9525	UVES	4658±56	2.5±0.1	0.00±0.04	1.07±0.09
HD116338	CORALIE	5126±50	3.1±0.1	0.15±0.04	1.34±0.05
HD36787	CORALIE	4739±56	2.8±0.1	0.11±0.04	1.19±0.08
HD9525	CORALIE	4709±55	2.6±0.1	0.04±0.04	1.13±0.09
HD190574	CORALIE	4793±52	2.9±0.1	0.06±0.04	1.21±0.07
HD202470	CORALIE	4726±56	2.9±0.1	0.13±0.04	1.0±0.1
HD2132	CORALIE	4911±50	2.9±0.1	-0.37±0.04	1.22±0.04
HD8410	CORALIE	4897±50	2.88±0.09	-0.04±0.04	1.07±0.05

Table 3.1: Atmospheric parameters calculated using `SPECIES` on the known binary systems. Publicly available data was retrieved for the stars not observed with CORALIE.

3.2.3 Physical parameters

For determining the physical parameters such as mass, radius, age, luminosity, and evolutionary stage, `SPECIES` relies on the `isochrones`[3] package (Morton, 2015). Using the estimated atmospheric parameters, `isochrones` constructs a model of the star and interpolates across a grid of MESA Isochrones and Stellar Tracks (`MIST`; Dotter, 2016) models using `MultiNest`[4] (Feroz et al., 2009), a Bayesian inference tool. The final values for each parameter are drawn from the obtained distributions.

---

[2] `http://archive.eso.org/eso/eso_archive_main.html`

[3] `https://github.com/timothydmorton/isochrones`

[4] `https://github.com/JohannesBuchner/PyMultiNest`

As discussed in Dotter (2016), `MIST` interpolates among a set of stellar evolution tracks. However, tracks spanning a range of initial masses are likely to have different lifetimes and numbers of time steps, making the interpolation process rather complex. To address this complexity, `MIST` employs a transformation that maps stellar mass to the corresponding evolutionary age. This transformation allows for the construction of an isochrone from a set of stellar evolutionary tracks spanning various initial masses but sharing the same chemical composition. The benefit of this approach is evident: it enables the representation of stellar evolution across different masses within a single framework.

`MIST` establishes a uniform temporal framework through the definition of Equivalent Evolutionary Phases (EEPs). These EEPs ensure that each stage of stellar evolution is represented by a fixed number of points, allowing consistent interpretation across different tracks and enabling the description of stellar evolution for all stars. EEPs are categorized into primary and secondary types, with primary EEPs being motivated by physical considerations. The most relevant primary EEPs for this study are:

- Terminal age main sequence (TAMS): When the central Hydrogen mass fraction (X_c) decreases to[5] $X_c = 10^{-12}$.
- The tip of the RGB (RGBTip): The point at which the stellar luminosity reaches its maximum (or $T_{\rm eff}$ reaches its minimum) after core H burning is complete but before core He burning has significantly progressed. Specifically, the central He mass fraction (Y_c) must satisfy the relation $Y_c > Y_{c,\rm TAMS} - 0.01$.
- The zero-age core He burning (ZACHeB): Marks the onset of sustained core He burning, indicating the HB phase. It is identified as a minimum in the core temperature while $Y_c > Y_{c,\rm RGBTip} - 0.03$.
- Terminal age core He burning (TACHeB): When the central He mass fraction decreases to $Y_c = 10^{-4}$, marking the end of core He burning.

Once the primary EEPs are determined, each segment is filled with a set of evenly distributed secondary EEPs. This dynamic sampling ensures precise interpolation between evolutionary tracks, even during phases of rapid evolution, such as post-MS phases. An illustration of this approach for the star HD202470 is depicted in Figure 3.3.

---

[5] Here we followed the definition given in Dotter (2016). Soto et al. (2021) defined the TAMS when the central Hydrogen mass fraction reaches $X_c = 10^{-2}$.

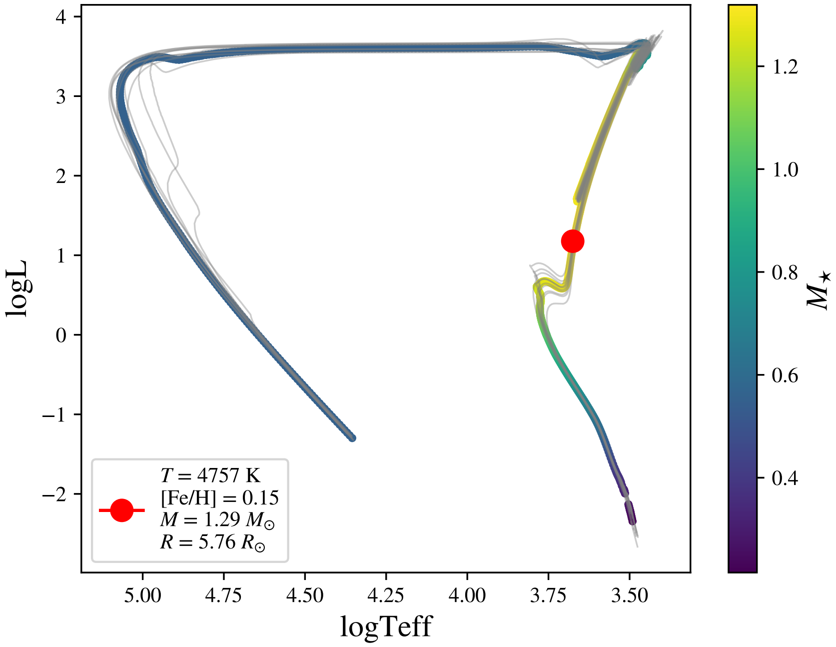

Figure 3.3: Isochrones for the star HD202470 computed using `SPECIES`. An initial model is built using pre-determined atmospheric parameters, then interpolated across a grid of `MIST` models using `Multinest`, facilitated by the `isochrones` Python package. Grey lines represent various isochrones, while the colored line denotes the most probable model. The red dot indicates the current evolutionary phase of the star based on the EEPs. Luminosity is expressed in solar units and effective temperature in Kelvin.

The `isochrones` package allows the creation of initial evolutionary tracks through a Bayesian framework. Users can specify distributions for mass, metallicity, age, and EEPs, among other parameters. Using these priors, a grid of `MIST` stellar models is generated, and `Multinest` is employed for interpolation and parameter fitting. The final values are determined from the posterior distributions.

`SPECIES` adopts initial parameters including a Salpeter initial mass function (IMF) with $\alpha = 2.35$, a metallicity distribution based on the local disk (Casagrande et al., 2016), a logarithmically flat prior for stellar age spanning 10^5–$10^{10.15}$ years, and uniform probability distribution for EEP between 200 and 1710, ensuring no pre-main sequence stages. The likelihood function incorporates atmospheric parameters derived previously, along with photometric magnitudes and parallax.

One of the outputs of `SPECIES` is the distribution of EEPs for each star. According to Soto et al. (2021), we define the MS as $202 < \text{EEP} < 454$, the RGB phase as

$454 < \mathrm{EEP} < 631$, and the HB phase as $631 \leq \mathrm{EEP} \leq 707$. Additionally, `SPECIES` estimates the probability of a star being in a particular evolutionary state based on its EEP distribution as follows:

$$P_{\mathrm{state}} = \frac{\sum \mathrm{EEP}_{\mathrm{state}}}{\sum N}, \tag{3.5}$$

where N is the total size of the EEP distribution.

Starname	Instrument	Mass	Radius	log L	Age	EEP	P_{MS}	P_{RGB}	P_{HB}
		($M_\odot$)	($R_\odot$)	(L$_\odot$)	(Gyr)				
HD5877	FEROS	$1.04^{+0.06}_{-0.06}$	$6.3^{+0.1}_{-0.1}$	$1.23^{+0.01}_{-0.01}$	9^{+2}_{-2}	505^{+1}_{-1}	0	1	0
HD14355	FEROS	$1.30^{+0.06}_{-0.06}$	$3.16^{+0.06}_{-0.06}$	$0.73^{+0.02}_{-0.02}$	$4.4^{+0.8}_{-0.6}$	480^{+1}_{-1}	0	1	0
HD153438	FEROS	$1.36^{+0.08}_{-0.07}$	$7.87^{+0.10}_{-0.09}$	$1.43^{+0.01}_{-0.01}$	$3.8^{+0.7}_{-0.6}$	511^{+1}_{-1}	0	1	0
HD179799	FEROS	$1.12^{+0.09}_{-0.08}$	$4.0^{+0.1}_{-0.1}$	$0.93^{+0.02}_{-0.02}$	7^{+2}_{-1}	490^{+2}_{-2}	0	1	0
HD27697	FEROS	$3.10^{+0.04}_{-0.04}$	$12.2^{+0.3}_{-0.3}$	$1.97^{+0.02}_{-0.02}$	$0.36^{+0.01}_{-0.01}$	535^{+2}_{-2}	0	1	0
HD32008	FEROS	$1.90^{+0.03}_{-0.03}$	$4.9^{+0.1}_{-0.1}$	$1.27^{+0.02}_{-0.01}$	$1.14^{+0.04}_{-0.03}$	488^{+2}_{-2}	0	1	0
HD62644	UVES	$1.26^{+0.02}_{-0.02}$	$2.34^{+0.06}_{-0.05}$	$0.67^{+0.01}_{-0.01}$	$4.7^{+0.2}_{-0.2}$	463^{+2}_{-2}	0	1	0
HD133166	FEROS	$1.33^{+0.07}_{-0.07}$	$4.09^{+0.04}_{-0.04}$	$0.88^{+0.01}_{-0.01}$	$5.0^{+1.0}_{-0.8}$	$488.6^{+0.7}_{-0.5}$	0	1	0
HD9525	UVES	$1.3^{+0.1}_{-0.1}$	$8.8^{+0.4}_{-0.3}$	$1.51^{+0.02}_{-0.02}$	5^{+2}_{-1}	515^{+2}_{-1}	0	1	0
HD116338	CORALIE	$2.57^{+0.03}_{-0.04}$	$8.6^{+0.1}_{-0.1}$	$1.64^{+0.01}_{-0.01}$	$0.58^{+0.02}_{-0.01}$	527^{+1}_{-1}	0	0.98	0.02
HD36787	CORALIE	$1.24^{+0.09}_{-0.08}$	$6.9^{+0.1}_{-0.1}$	$1.31^{+0.01}_{-0.01}$	5^{+1}_{-1}	$506.6^{+0.9}_{-0.7}$	0	1	0
HD9525	CORALIE	$1.4^{+0.1}_{-0.1}$	$8.6^{+0.3}_{-0.3}$	$1.51^{+0.02}_{-0.02}$	$3.1^{+1}_{-0.7}$	514^{+1}_{-2}	0	1	0
HD190574	CORALIE	$0.98^{+0.03}_{-0.02}$	$5.15^{+0.08}_{-0.08}$	$1.05^{+0.01}_{-0.01}$	$12.6^{+0.7}_{-1}$	$499.6^{+0.5}_{-0.6}$	0	1	0
HD202470	CORALIE	$1.2^{+0.1}_{-0.1}$	$5.8^{+0.1}_{-0.1}$	$1.17^{+0.02}_{-0.02}$	6^{+2}_{-2}	501^{+1}_{-1}	0	1	0
HD2132	CORALIE	$1.49^{+0.09}_{-0.09}$	$9.0^{+0.1}_{-0.1}$	$1.61^{+0.01}_{-0.01}$	$2.1^{+0.5}_{-0.3}$	$518.6^{+0.7}_{-0.8}$	0	1	0
HD8410	CORALIE	$1.4^{+0.1}_{-0.1}$	$6.2^{+0.2}_{-0.2}$	$1.28^{+0.02}_{-0.02}$	$3.0^{+0.9}_{-0.6}$	503^{+1}_{-1}	0	1	0

Table 3.2: Physical parameters calculated using `SPECIES` for the known binary systems. P_{MS}, P_{RGB} and P_{HB} are the probabilities for the star to be on the MS, RGB or HB, respectively.

We present the physical parameters derived with `SPECIES` for the known binaries in Table 3.2 as an example. For those not observed with CORALIE, we retrieved publicly available high-resolution spectra from the ESO archive.

3.2.4 Macroturbulence and rotational velocity

Macroturbulence velocity is measured using the Eq. (1) from dos Santos et al. (2016), given by:

$$v_{\mathrm{mac},\lambda} = v^{\odot}_{\mathrm{mac},\lambda} - 0.00707T_{\mathrm{eff}} + 9.2422\times10^{-7}T^2_{\mathrm{eff}} + 10.0 + k_1(\log g - 4.44) + k_2, \quad (3.6)$$

where λ represents the wavelength specific to the lines n$vwpvwv^{\odot}_{\mathrm{mac},\lambda}$ are the velocities obtained for each line in the solar spectra, T_{eff} and $\log g$ are the ones produced by `SPECIES` (see Sec. 3.2.2) and k_1, k_2 are constants equal to -1.81 ± 0.26 and -0.05 ± 0.03, respectively. The uncertainty for each line is given by:

$$\sigma^2_{\mathrm{vmac},\lambda} = \sigma^2_{\mathrm{vmac}\odot,\lambda} + (1.848\times10^{-6}T_{\mathrm{eff}} - 0.00707)^2\sigma^2_{T_{\mathrm{eff}}} + k_1^2\sigma^2_{\log g} + (\log g - 4.44)^2\sigma^2_{k_1} + \sigma^2_{k_2}. \quad (3.7)$$

The final v_{mac} corresponds to the average of the individual results, weighted by their uncertainties. If the value is too small or negative, Eq. (2) from Brewer et al. (2016) is used:

$$v_{\mathrm{mac}} = \begin{cases} 2.202\exp(0.0019(T_{\mathrm{eff}}-5777)+1.30) & \log g \geq 4.0 \\ 1.166\exp(0.0028(T_{\mathrm{eff}}+3.30)) & 3 \leq \log g < 4.0. \\ 4.0 & \log g < 3.0 \end{cases} \quad (3.8)$$

For the rotational velocity, rotationally broadened synthetic profiles are fitted to the same absorption lines used to compute v_{mac}, while uncertainties are computed by varying the normalized flux of each line by a fixed amount and recomputing the rotational velocity through a total of 1000 iterations, resulting in a distribution of rotational velocities.

Chapter 4

Results and Discussion

This chapter aims to present and discuss the results obtained by applying the methods described in Chapter 3. We start by presenting the outcomes of `CERES` and `SPECIES`, providing a detailed discussion of them. Subsequently, we compare the outcomes from `SPECIES` with other techniques reported in the literature to validate our findings. Finally, we address the consistency between our results and those from the literature.

4.1 Results from `CERES`

Using the CCF technique implemented in `CERES`, we computed the RV for 419 high-resolution spectra of 235 different stars. Subsequently, we classified them according to the method explained in Sec. 2.2. The results are presented in Table A.1. The first five stars correspond to the RV standards used in different runs, followed by known binaries observed with CORALIE (Table 2.2). Subsequent stars are ordered first by category, then by number of epochs, and finally by alphabetical order. Multiple epochs for the same star are ordered by date. It is critical to recall that the errors presented in Table A.1 are formal statistical errors computed by eq. 3.2. Other sources of error are not taken into account.

From stars in Table A.1, 112 have the highest probability of being part of a binary system (i.e., they are categorized as 1), 66 of which already have multiple epoch observations. Follow-up observations after having the final sample will focus primarily on these stars in order to construct RV curves and finally confirm binarity.

From the remaining targets, 60 have a medium probability of being part of a binary system (i.e., categorized as 2), 16 of which already have multi-epoch observations. These stars will be followed up when possible since they also have good probabilities of being part of a binary system.

The remaining 58 targets, which have quite low probabilities of being part of a binary system (i.e., classified as 3), will still be followed up. However, we will assign them a low priority.

In total, $\sim 75\%$ of the stars in the observed sample have a high probability of being binaries and $\sim 48\%$ of these already have multi-epoch observations. Therefore, we are confident that the project is in a strong position. Additionally, since we only have 193 top-priority candidates left to observe, we expect to achieve our first main goal after just a few more observing runs.

4.2 Results from `SPECIES`

After running `SPECIES` for all stars in our sample (excluding RV standards), we obtained the distribution for each stellar parameter. We omitted the stars 29PSC, HD103433, HD177668, HD219470, and HD220096. For 29PSC, HD103433, HD219470, and HD220096, `SPECIES` failed to find sufficient Fe I and Fe II lines for a good fit in these three cases. According to the literature, 29PSC is a MS magnetic star with $T_{\rm eff} = 13\,400$ K, $\log g = 3.85$, $\mathrm{R} = 3.68\ \mathrm{R}_\odot$ and $\mathrm{M} = 3.86\ \mathrm{M}_\odot$ (Glagolevskij, 2019). Therefore, we can safely discard this star from our sample. HD219470 is a G6 IV star according to Houk (1978), while Hon et al. (2021) determined its stellar parameters using asteroseismology, they found a $T_{\rm eff} = 4\,845 \pm 96$ K, $\log g = 2.48 \pm 0.06$ dex, $\mathrm{R} = 9.6 \pm 0.5\ \mathrm{R}_\odot$ and $\mathrm{M} = 1.02 \pm 0.12\ \mathrm{M}_\odot$. Based on these parameters, this star cannot be discarded from our sample, indeed, it has high values of RUWE (4.383) and AEN (0.508); therefore, we decided to exclude it from the current analysis and obtain more spectra to re-analyzed it. HD220096 has been cataloged as a G4 III star by Cutispoto et al. (2001), while Günther et al. (2020) identified it as an eruptive star with $T_{\rm eff} = 5\,192$ K and $\mathrm{R} = 9.26\ \mathrm{R}_\odot$. This star has low RUWE (0.926) and AEN (0.306) values, and given its eruptive nature, it is not clear whether this star is suitable to be analyzed with our tools, therefore, we decided to exclude it from this analysis and re-analyzed it using alternative methodologies in the future.

For HD177668, the `SPECIES` results were contradictory: the higher SNR spectrum obtained (SNR = 40) classifies it as MS star with $T_{\rm eff} = 4\,518$ K and $\log g = 4.128$, while the lower SNR spectrum (SNR = 28) suggests it is a RG with $T_{\rm eff} = 4\,826$ K and $\log g = 2.676$. According to the literature, it is a K2/3 III star with $T_{\rm eff} = 4\,659$ K and IR extend measurements (Cruzalèbes et al., 2019). Given that we cannot explain such a discrepancy obtained from our spectra, and that this star has a high RUWE value (3.098), and a AEN value close to the threshold (0.347) we decided to exclude it from the current analysis and obtain more spectra in order to examine the cause of the underlying discrepancies. The case of HD 103433 is particularly interesting, as it is identified as a spectroscopic binary in the literature (Gaia Collaboration, 2022). The inability of `SPECIES` to analyze this star may stem from contamination of the spectral lines by the companion, as the code cannot fit a composite spectrum. Stellar parameters for HD103433 have been determined by Hon et al. (2021), yielding $T_{\rm eff} = 4,711 \pm 94$ K, L= $59 \pm 3\,{\rm L}_{\odot}$, and R= $11.6 \pm 0.6\,{\rm R}_{\odot}$.

For the stars with multi-epoch spectra, we used the highest SNR observation instead of stacking the spectra due to the complexity of the stacking process. Different epochs have many lines and varying exposure times, making careful interpolation necessary. The parameters from individual epochs were consistent within their errors, thus we opted for the higher SNR results.

As discussed in Sec. 3.2.3, EEPs serve to describe the evolutionary state of the stars. Consequently, we can further separate RGB stars from potential contaminants by using the distribution of EEPs and selecting targets within the range $454 < \text{EEP} < 631$. This process is illustrated in Figure 4.1, where various evolutionary states are highlighted with vertical lines. In this figure, ZAMS stands for zero-age MS, while the rest of the acronyms were defined in Sec. 3.2.3. Notice that we do not have any stars in the MS stage, on the other hand, we do have some stars already in the He burning stage.

Following the exclusion of stars lying outside the RGB zone, the final sample consists of 184 stars with a high probability of being in the RGB phase. The distribution of stellar parameters is depicted in Figure 4.2 (blue histograms), with RGB stars highlighted separately (red histograms) as discussed above. The complete list with derived parameters can be found in Table A.2. The first 7 entries are the known binaries observed with CORALIE, while the remaining stars are arranged alphabetically.

According to Fig. 4.1, approximately 82% of the stars in our sample are in the early stages of the RGB phase, way before the tip of the RGB. We also identified some contamination from core-He burning (CHeB) stars, accounting for about 18% of the sample, likely due to RC stars, which is expected (Girardi, 2016).

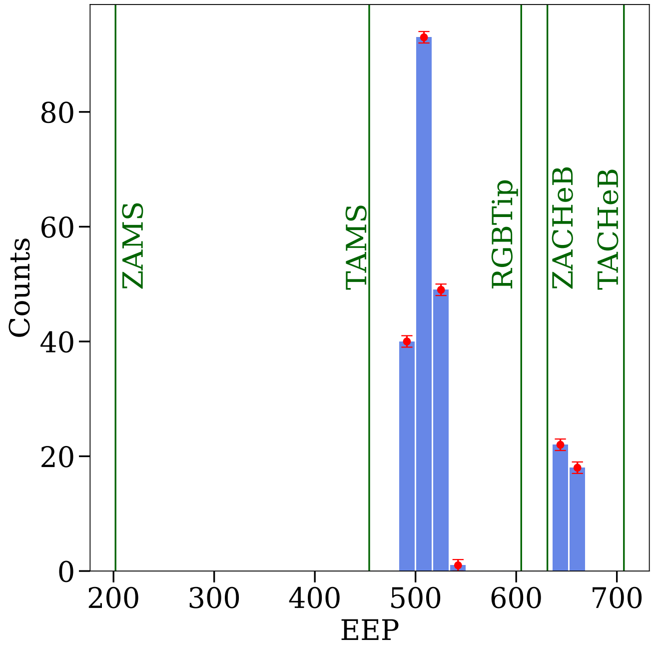

Figure 4.1: Distribution of Equivalent Evolutionary Phases for the CORALIE sample. Evolutionary states determined based on the EEPs are labeled. The error bars in each bin represent the uncertainty in the number of stars with the corresponding EEP range, given as the 16% and 84% percentiles of the EEP distribution for each star.

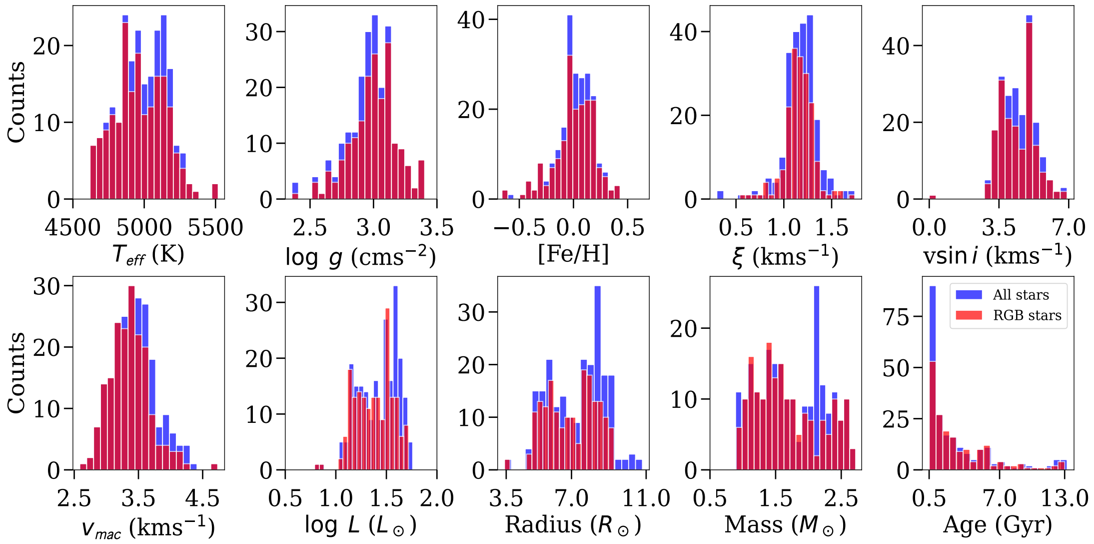

Figure 4.2: Distribution of atmospheric and fundamental stellar parameters calculated using `SPECIES` for all stars (226) in our sample. The RG sample (red histograms) is a subsample of 184 stars with $454 < \mathrm{EEP} < 631$.

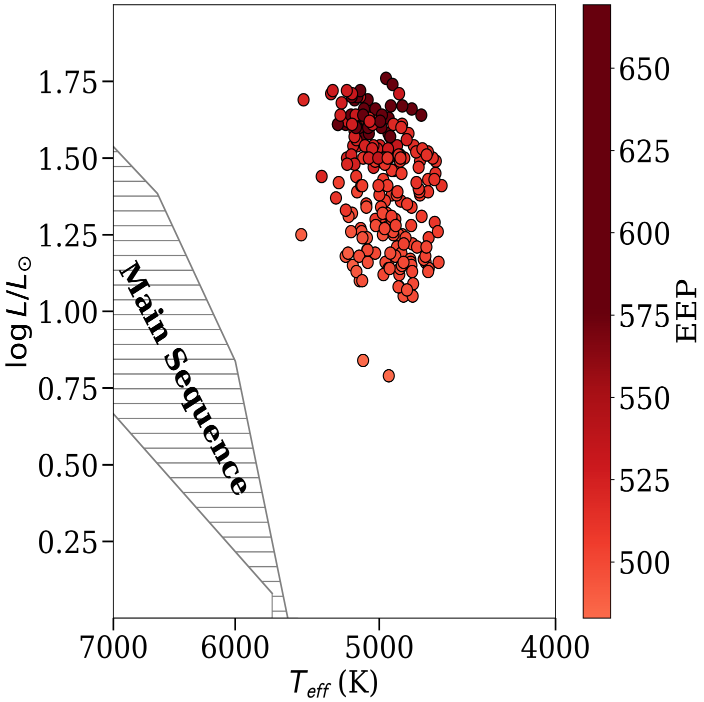

Figure 4.3: HRD for stars analyzed in this work. The temperature axis is on a logarithmic scale. The different red intensities indicate the EEP of each target, as given by the color bar on the right. As a comparison, a theoretical MS band computed with MESA is shown in gray.

Given that `SPECIES` provides luminosity alongside effective temperature, we can confirm the evolutionary state of the stars by plotting an HRD, as shown in Fig. 4.3. For comparison, a theoretical MS band computed with MESA is shown as the gray area. This MS band extends from ZAMS to the TAMS, and was constructed using stellar tracks for masses between $1\,\mathrm{M}_\odot$ and $15\,\mathrm{M}_\odot$, although we show only a small portion in the figure.

From Fig. 4.3, it is clear that all stars in our sample are indeed beyond the MS, showing lower effective temperatures and higher luminosities, confirming their status as giants. Additionally, we mapped the intensity of the red color of each target to its corresponding EEP, demonstrating that stars with EEP > 631 overlap with the identified RGBs, indicating RC contamination. Thus, we conclude that the selection criteria detailed in Chapter 2 were effective in selecting RGB stars in the early stages of their evolutionary phase, successfully filtering out MS stars and more evolved systems, with the expected minor contamination from RC stars.

Regarding Fig. 4.2, we observe that the T_{eff} and $\log g$ are consistent with the subgiant and early giant phases. Fig. 4.4 presents a Kiel diagram for the sample, showing that hotter stars have higher surface gravity and it steadily decreases for cooler stars. This trend is also observed for CHeB stars in the sample, which are consistent with the theoretical results presented in Girardi (2016). Stars with $454 < \mathrm{EEP} < 631$ and $\log g \gtrsim 3$ are most likely in the sub-giant phase.

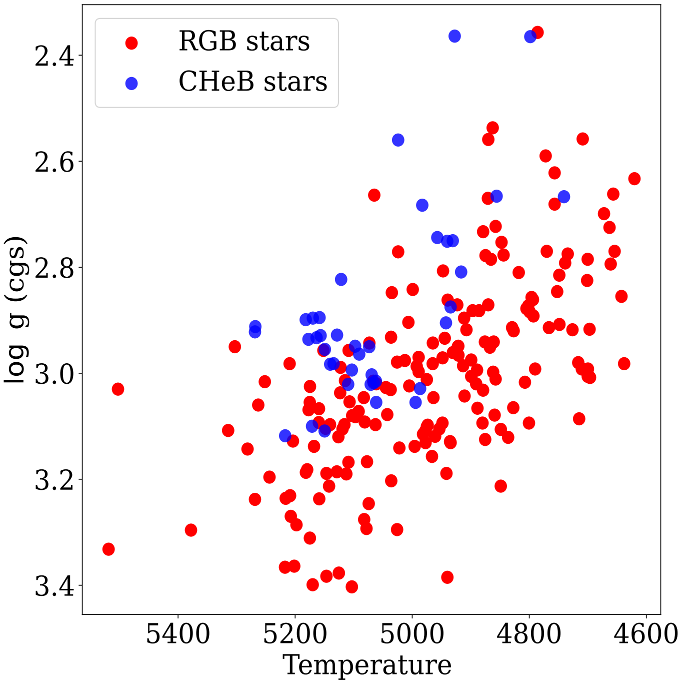

Figure 4.4: Kiel diagram for stars in our sample. RGB stars are those with $454 < \mathrm{EEP} < 631$ while core helium-burning (CHeB) stars are those with $\mathrm{EEP} > 631$.

The effective temperature distribution in Fig. 4.2 has a mean of 4 985 K and a standard deviation of 172 K. However, it is not entirely symmetrical, showing a steep drop at about 5 000 K, followed by a quick rise. This pattern suggests a bimodal distribution rather than a Gaussian.

In contrast, the $\log g$ distribution is more symmetrical, with a mean of 3.0 dex (cgs) and a standard deviation of 0.2 dex. However, there is a small asymmetry towards higher $\log g$ values, which is consistent with the presence of sub-giant stars.

The metallicity distribution shows a pronounced peak at -0.07 dex. However, the overall distribution is quite symmetrical around 0.0, with the presence of a few metal-poor stars. This can be explained by the fact that RGB stars are systematically older than typical unevolved stars in the solar neighborhood. Therefore, RGB stars in our sample reflect the lower metallicity the Galaxy had at the time of their formation.

The microturbulent velocity distribution is quite symmetric, concentrated around a mean of 1.2 kms^{-1}, with a standard deviation of 0.2 kms^{-1}, while the distribution of rotational velocity is clearly non-symmetric, with a mean of 4.5 kms^{-1} and a standard deviation of 0.9 kms^{-1}. One star rotates at $v \sin i = 0$ kms^{-1}, which is only possible if the inclination is ~ 0. However, this is an artifact from the code, since the measurement error is also 0. Inspecting the star (BD+004462), we realized that the code could not fit the lines used to derive the rotational velocity. There is no obvious reason for this failure from the visual inspection, we will investigate it further in the future.

Macroturbulent velocity shows a symmetric distribution around a mean of 3.4 kms^{-1} with a standard deviation of 0.4 kms^{-1} and a small asymmetry towards higher values. Regarding luminosity, the distribution shows a mean of $\log L\,(L_\odot)$ =1.4 with a standard deviation of 0.2. CHeB stars exhibit higher luminosities than those on the RGB, as shown in Fig. 4.3. This is consistent with the selection criteria (Sec. 2.1), where the uppercut in the Gaia CMD ensures that contamination from the RC is limited to the most luminous objects.

The radius distribution also seems to present a bimodality. For stars with a radius lower than $\sim 7.5\,\mathrm{R}_\odot$, the mean is $6.0\,\mathrm{R}_\odot$, and the standard deviation is $0.8\,\mathrm{R}_\odot$, while for stars with radii larger than $\sim 7.5\,\mathrm{R}_\odot$, the mean and standard deviation are $8.5\,\mathrm{R}_\odot$ and $0.7\,\mathrm{R}_\odot$. Notably, CHeB stars exhibit larger radii than RGB stars in the sample, which is expected given their higher luminosity and similar surface temperature. Observations of RC stars through interferometry and spectroscopy indicate that they can easily reach sizes up to $10\,\mathrm{R}_\odot$ (Gallenne et al., 2018).

The mass distribution also appears to be bimodal with masses $\lesssim 2\,\mathrm{M}_\odot$ having a mean of $1.4\,\mathrm{M}_\odot$ and a standard deviation of $0.3\,\mathrm{M}_\odot$, while for masses $\gtrsim 2\,\mathrm{M}_\odot$ the distribution has a mean of $2.3\,\mathrm{M}_\odot$ with a standard deviation of $0.2\,\mathrm{M}_\odot$. However, there is no physical reason to think that RGB stars should have two different populations at low and intermediate-mass. Furthermore, one has to be very careful when interpreting the mass distribution of stars in an evolving stage. It might be tempting to say that one expects to have many more low-mass stars due to the behavior of the initial mass function. However, stellar main-sequence lifetimes, as well as the duration of the evolved phases, RGB and CHeB in our case, depend non-trivially on the initial mass. Therefore, the mass function of the RGBs should not be proportional or depend in any obvious way on the initial mass function. Given that our sample is not yet complete, a deeper analysis of the mass distribution will have to wait until we compile the full 500 pc RG sample.

On the other hand, CHeB stars also exhibit a bimodality in the mass distribution, as shown in Fig. 4.5. However, in contrast to the RGB stars, RC stars do have a physical reason for this bimodality. As explained by Girardi (2016), this arises from a combination of the initial mass function, which causes the first peak, and the fact that stars more massive than $\sim 2\,\mathrm{M}_\odot$ do not experience the helium core flash at the tip of the RGB. As a consequence, they have more helium available in their cores during the CHeB phase, leading to a longer lifetime; hence making them more probable to be detected, explaining the second peak. Fig. 4.5 shows this different behavior between RGB and CHeB stars more clearly. The RBG population is distributed over the entire mass-logg plane, while the CHeB population shows two distinct peaks around 1.0 and $2.0\,\mathrm{M}_\odot$. This is consistent with the expected distribution of RC stars shown in Fig. 4(a) of Girardi (2016), which has peaks at these values, strengthening the fact that the CHeB stars found in our sample are the expected RC contaminants.

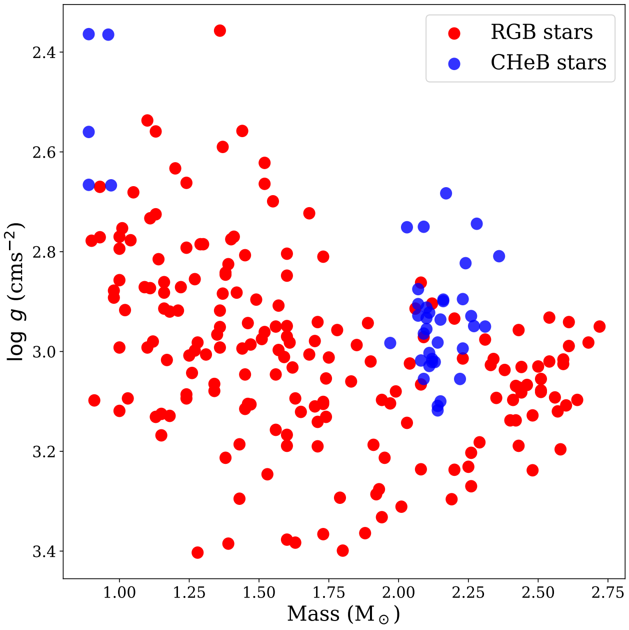

Figure 4.5: Correlation between mass and surface gravity for stars in our sample. RGB stars with masses above $\sim 2\ \mathrm{M}_\odot$will probably not ignite helium under degenerate conditions. CHeB stars show two distinct populations.

Concerning the age distribution, there is a significant presence of relatively young stars in the sample. However, very old stars are also present. This observation aligns with the range of masses. Moreover, Fig. 4.6 confirms that the more massive stars are the younger and low-mass stars the older, as they should be. However, estimating the age of stars, particularly during the giant phases, is challenging and subject to significant uncertainties (Martig et al., 2015; Warfield et al., 2021; Valle et al., 2024). Therefore, while these results serve as a rough check for consistency, they cannot be interpreted as precise indicators of stellar age.

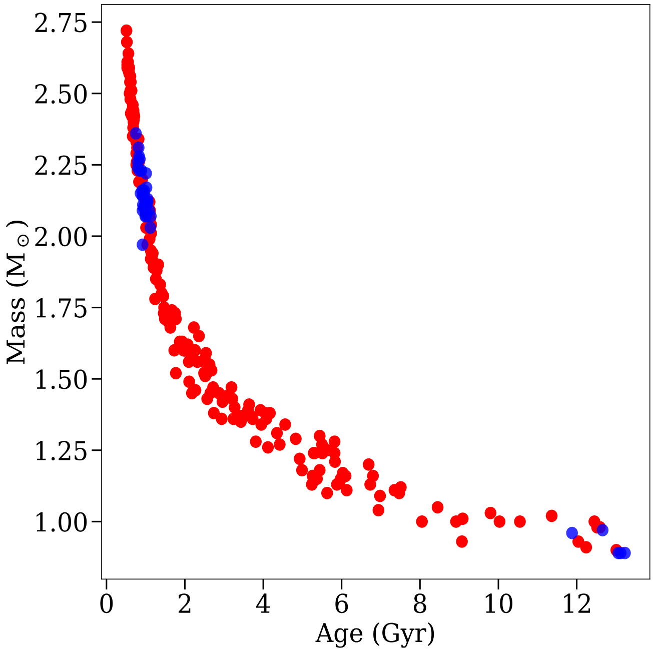

Figure 4.6: Correlation between mass and age showing that high-mass stars are younger than low-mass stars, as expected.

An essential prediction made by Vos et al. (2020) is the correlation between mass and metallicity for progenitors of wide sdB binaries. Our results, as depicted in Fig. 4.7, align well with their predictions, showing that wide sdB progenitor masses increase with metallicity. For the comparison, we excluded targets with masses exceeding 2.0 M$_\odot$, since Vos et al. (2020) limited their study to this mass value.

4.3 Comparison with the literature

We searched the literature for atmospheric and fundamental parameters of stars in our sample. We found 60 matched targets with the sample of Hon et al. (2021) and 27 with the one of Zhou et al. (2024), 20 targets are present in both works. Both authors used asteroseismology, one of the most powerful tools to derive stellar parameters and probe stellar interiors. The technique is based on measuring stellar oscillations via Fourier analysis. Specifically, the frequency at maximum oscillation power, $\nu_{\rm max}$, and large frequency separation, $\Delta\nu$, are measured from precise light curves obtained with

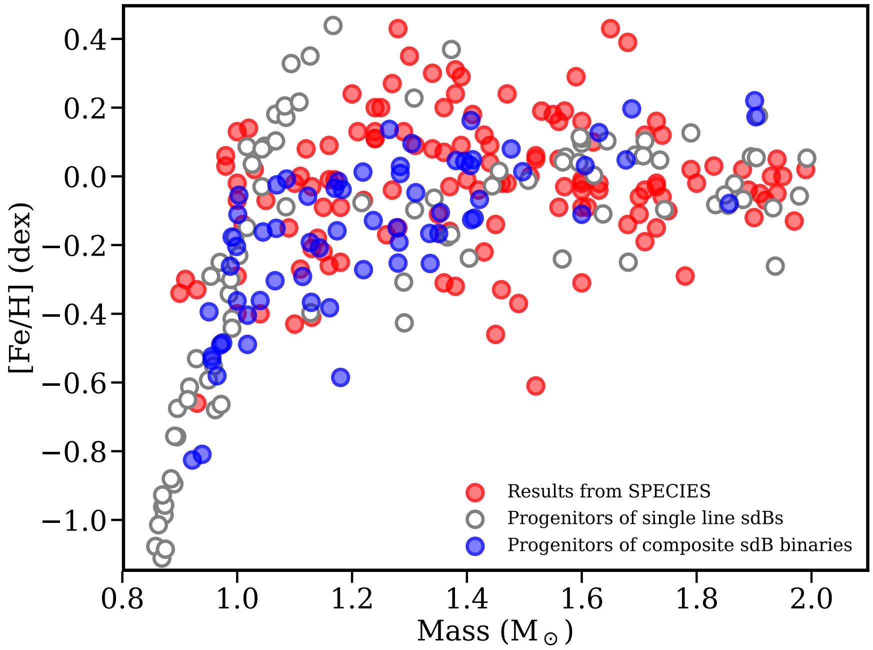

Figure 4.7: Correlation between metallicity and mass for our potential sdB progenitors (red circles) compared with the theoretical predictions of Vos et al. (2020). Filled blue circles are systems that can be identified as composite sdB binary systems. Open grey circles are those where only one component is visible. Filled red circles are the `SPECIES` results for RGB stars in our sample with masses $< 2\,\mathrm{M}_\odot$.

space-based missions such as K2 (Howell et al., 2014) and TESS (Ricker et al., 2015). Using these parameters, scaling relations (Ulrich, 1986; Brown et al., 1991; Kjeldsen & Bedding, 1995; Belkacem et al., 2011) can be used to measure absolute mass and radius for stars that exhibit oscillations similar to those observed in the Sun (solar-like oscillators), among which low-mass RGs are included (see Aerts, 2021, for a review).

Hon et al. (2021) detected 158 000 RGs using long-cadence (30 min) TESS data and measured their ν_{max} using machine-learning techniques. Afterward, they combined Gaia parallaxes with 2MASS JHK photometry to estimate effective temperatures and luminosities. They calculated the radius using the Stefan-Boltzmann relation:

$$L = 4\pi\sigma \mathrm{R}^2 T_{\mathrm{eff}}^4, \tag{4.1}$$

where σ is the Stefan-Boltzmann constant. They estimated the surface gravity using the scaling relation:

$$\frac{g}{g_\odot} = \frac{\nu_{\rm max}}{\nu_{\rm max,\odot}} \left(\frac{T_{\rm eff}}{T_{\rm eff,\odot}}\right)^{1/2}. \tag{4.2}$$

Hon et al. (2021) used $\log g_\odot = 4.44$, $\nu_{\rm max,\odot} = 3\,090$ μHz and $T_{\rm eff,\odot} = 5\,777$ K. Finally, they estimated masses using the relation between radius, mass, and surface gravity:

$$\frac{\rm M}{\rm M_\odot} = \frac{g}{g_\odot} \left(\frac{\rm R}{\rm R_\odot}\right)^{2}. \tag{4.3}$$

On the other hand, Zhou et al. (2024) computed $\nu_{\rm max}$ and $\Delta\nu$ for 8 651 solar-like oscillators using 2-minute cadence TESS light curves and derived seismic surface gravities using Eq. 4.2. They also calculated mass and radius using the scaling relations:

$$\frac{\rm M}{\rm M_\odot} = \left(\frac{\nu_{\rm max}}{\nu_{\rm max,\odot}}\right)^{3} \left(\frac{\Delta\nu}{\Delta\nu_\odot}\right)^{-4} \left(\frac{T_{\rm eff}}{T_{\rm eff,\odot}}\right)^{3/2}, \tag{4.4}$$

$$\frac{\rm R}{\rm R_\odot} = \left(\frac{\nu_{\rm max}}{\nu_{\rm max,\odot}}\right) \left(\frac{\Delta\nu}{\Delta\nu_\odot}\right)^{-2} \left(\frac{T_{\rm eff}}{T_{\rm eff,\odot}}\right)^{1/2}, \tag{4.5}$$

where $\Delta\nu_\odot = 135.1$ μHz, while $\nu_{\rm max,\odot}$ and $T_{\rm eff,\odot}$ are the same as in Hon et al. (2021). They used the $T_{\rm eff}$ reported in Gaia DR3 Radial Velocity Spectrometer (RVS; Recio-Blanco et al., 2023) data. Additionally, Zhou et al. (2024) also performed spectral energy distribution (SED) fitting as an independent method to validate their seismic results. They employed the SEDEX pipeline[1] (Yu et al., 2021, 2023) along with MARCS model spectra (Gustafsson et al., 2008). They used $T_{\rm eff}$, $\log g$, metallicity, and parallaxes derived from Gaia DR3 RVS spectra as priors, in combination with apparent magnitudes from available photometric databases.

It is informative to check whether the results from Hon et al. (2021) agree with those from Zhou et al. (2024) for the 20 stars the two studies have in common with `SPECIES`. Since both use the same method to derive surface gravities and luminosities, but different methods to derive radius and masses, high dispersion is expected in the latter measurements. The comparison plot is shown in Fig. 4.8, confirming this expectation.

Panels (a), (b), and (c) in Fig. 4.8 show the good agreement between the effective temperatures, surface gravities, and luminosities reported by both studies. Fractional residuals for these quantities, computed as $\frac{X_{\rm Zhou}-X_{\rm Hon}}{X_{\rm Hon}}$, where X represents a stellar

---

[1] `https://github.com/Jieyu126/SEDEX`

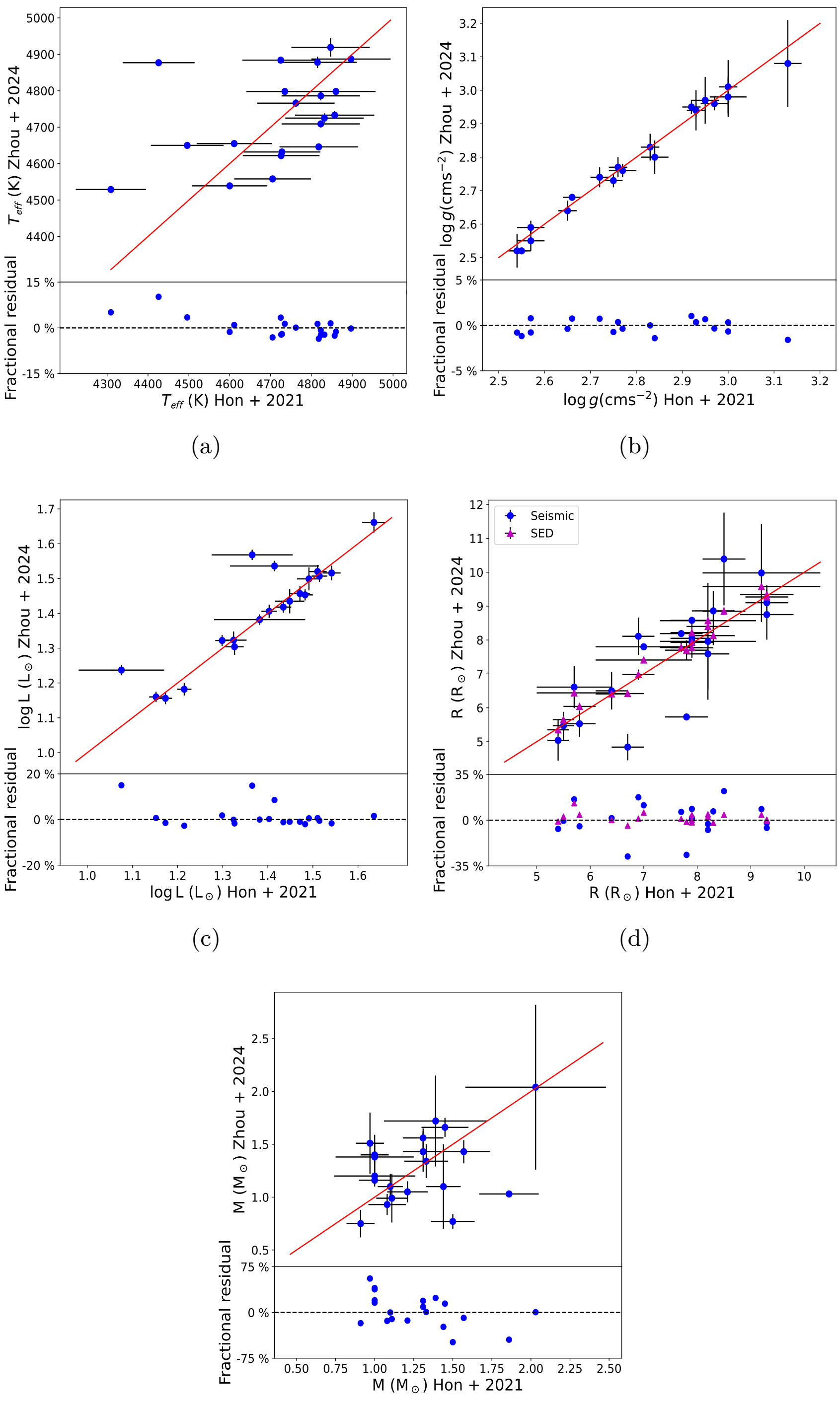

(a) (b)

(c) (d)

(e)

Figure 4.8: Comparison between stellar parameters reported by Hon et al. (2021) and Zhou et al. (2024). The red solid line in the upper panels indicates the one-to-one relation. The fractional residuals are calculated as $\frac{X_{\text{Zhou}}-X_{\text{Hon}}}{X_{\text{Hon}}}$, where X represents a stellar parameter.

	$T_{\rm eff}$	$\log g$	logL	$\rm R_{seismic}$	$\rm R_{SED}$	M
MFR	-0.49%	-0.17%	-0.05%	1.03%	1.10%	0.62%
Scatter	3.24%	0.77%	5.01 %	12.36%	3.62%	26.13%

Table 4.1: Comparison of parameters from Hon et al. (2021) and Zhou et al. (2024). MFR stands for median fractional residual.

parameter, do not exceed 20%, and the median fractional residual is close to zero in all three cases, as shown in Table 4.1.

In Panel (d) of Fig. 4.8, where we compare the radii derived by both studies, we have also distinguished between those derived by Zhou et al. (2024) using asteroseismic scaling relations from those derived using SED fitting. We can see that the radius determined by Zhou et al. (2024) using SED fitting agrees better with the radius estimated by Hon et al. (2021), with a scatter in the median fractional residual more than three times higher for the seismic radius compared to the SED radius. This result is expected, since Hon et al. (2021) also used photometric methods to derive the radius.

The mass, shown in Fig. 4.8 Panel (e), has the largest errors and discrepancies between the two studies, as expected. The median fractional residual is 26%, highlighting the difficulty in estimating stellar masses, even using similar techniques.

Comparison of the results from Hon et al. (2021) and Zhou et al. (2024) with the parameters obtained with `SPECIES` is shown in Fig. 4.9, where it can be seen that `SPECIES` reports larger (formal) errors in general. Panels (a) and (b) in Fig. 4.9 show that `SPECIES` gives slightly larger values for both $T_{\rm eff}$ and $\log g$. This can also be seen in Table 4.2 by the relatively large negative median fractional residual for these parameters (-2.28% for $T_{\rm eff}$ and -3.56% for $\log g$). Systematic biases in $T_{\rm eff}$ determination for RGs using different approaches is a known issue in the literature (e.g., Salaris et al., 2018; Hegedűs et al., 2023; Yu et al., 2023; Valle et al., 2024), which can bias the estimated mass, and thus the age (e.g., Martig et al., 2015; Warfield et al., 2021). However, investigating this discrepancy further is out of the scope of this work, and according to Table 4.2, the scatter is $< 4\%$ for both, $T_{\rm eff}$ and $\log g$ for our case. Hence, the atmospheric parameters calculated by `SPECIES` are in good agreement with those found in the literature.

Additionally, Fig. 4.9 Panel (c) shows very good agreement in luminosity, with `SPECIES` results having relatively lower errors. The median fractional residual is 1.88%, with a scatter of 5.79%. Results from Zhou et al. (2024) appear to align better with `SPECIES` than those from Hon et al. (2021). However, there are fewer points to compare with Zhou et al. (2024), which might cause this apparent agreement.

	Hon+2021		Zhou+2024	
Parameter	MFR	Scatter	MFR	Scatter
T_{eff}	-2.09%	2.86%	-2.41%	1.50%
$\log g_{\text{seismic}}$	-3.93%	3.79%	-2.65%	3.38%
logL	1.53%	6.08%	2.12%	4.82%
R_{seismic}	—	—	4.91%	13.15%
R_{SED}	2.60%	11.87%	6.21%	7.90%
M	-11.95%	16.97%	-2.07%	23.09%

Table 4.2: Comparison of `SPECIES` results with those from Hon et al. (2021) and Zhou et al. (2024).

It is also notable that the apparent overestimation seen in values of T_{eff} and $\log g$ calculated by `SPECIES` is not as large for the luminosity. This may come from the method used by `SPECIES` to estimate parameters. While T_{eff} and $\log g$ are derived from colors and spectral equivalent widths, luminosity, and other physical parameters, are determined by fitting a stellar model using `isochrones`. This could also explain why errors appear smaller for physical parameters compared to atmospheric ones.

Panel (d) in Fig. 4.9, which compares the radii, shows a pattern similar to Panel (c) in Fig. 4.9, which is expected due to the strong correlation between radius and luminosity. Considering the seismic radius from Zhou et al. (2024), the median fractional residual is 2.76% with a scatter of 12.22%. This changes to 3.54% with a scatter of 11.01% for the SED radius. The scatter in the results is bigger for $R > 8\,\mathrm{R}_\odot$, although the sample size is too small to draw robust conclusions for this regime.

For mass, Panel (e) in Fig. 4.9 shows good agreement at the low-mass end. However, for $M \gtrsim 1.25\,\mathrm{M}_\odot$, there is a notable discrepancy between the seismic masses and our results, with `SPECIES` systematically overestimating the mass. Mass discrepancy is a known issue in RG stars (e.g., Salaris et al., 2018; Valle et al., 2024), as well as in intermediate and high-mass stars (e.g., Herrero et al., 1992; Tkachenko et al., 2020). As we mentioned, a bias in effective temperature can lead to a bias in the mass, and since we obtained overall higher effective temperatures using `SPECIES` in comparison to Hon et al. (2021) and Zhou et al. (2024), this could lead to the apparent overestimation in mass. These discrepancies can be used to test and calibrate the evolutionary models currently used to model RG stars, since, for example, mixing, enhancement of α elements, and boundary conditions have a huge impact on constraining stellar parameters during the RGB phase (Salaris et al., 2018; Martig et al., 2015; Valle et al., 2024). Moreover, mixing also plays a crucial role in the formation of sdBs (Arancibia-Rojas et al., 2024). Therefore, we plan to investigate these discrepancies further with more data and refined models to have more robust constraints on the physics of sdB formation.

The median fractional residual for mass is -11.55%, with a scatter of 18.87%, which is larger than for other stellar parameters. However, most residuals in panel (e) of Fig. 4.9 are within one standard deviation, indicating overall good agreement.

From this analysis, we conclude that atmospheric parameters from `SPECIES` are less precise but more accurate, as errors in these parameters are typically higher than those reported in Hon et al. (2021) and Zhou et al. (2024), but the dispersion in the residuals is low. Conversely, physical parameters are less accurate but more precise, with lower errors reported by `SPECIES` compared to Hon et al. (2021) and Zhou et al. (2024), but with higher dispersion in the residuals.

In general, our estimates align well with those from Hon et al. (2021) and Zhou et al. (2024). Even though the dispersion in mass is higher, the overall results are still within one standard deviation. Therefore we conclude that the results from `SPECIES` are reliable.

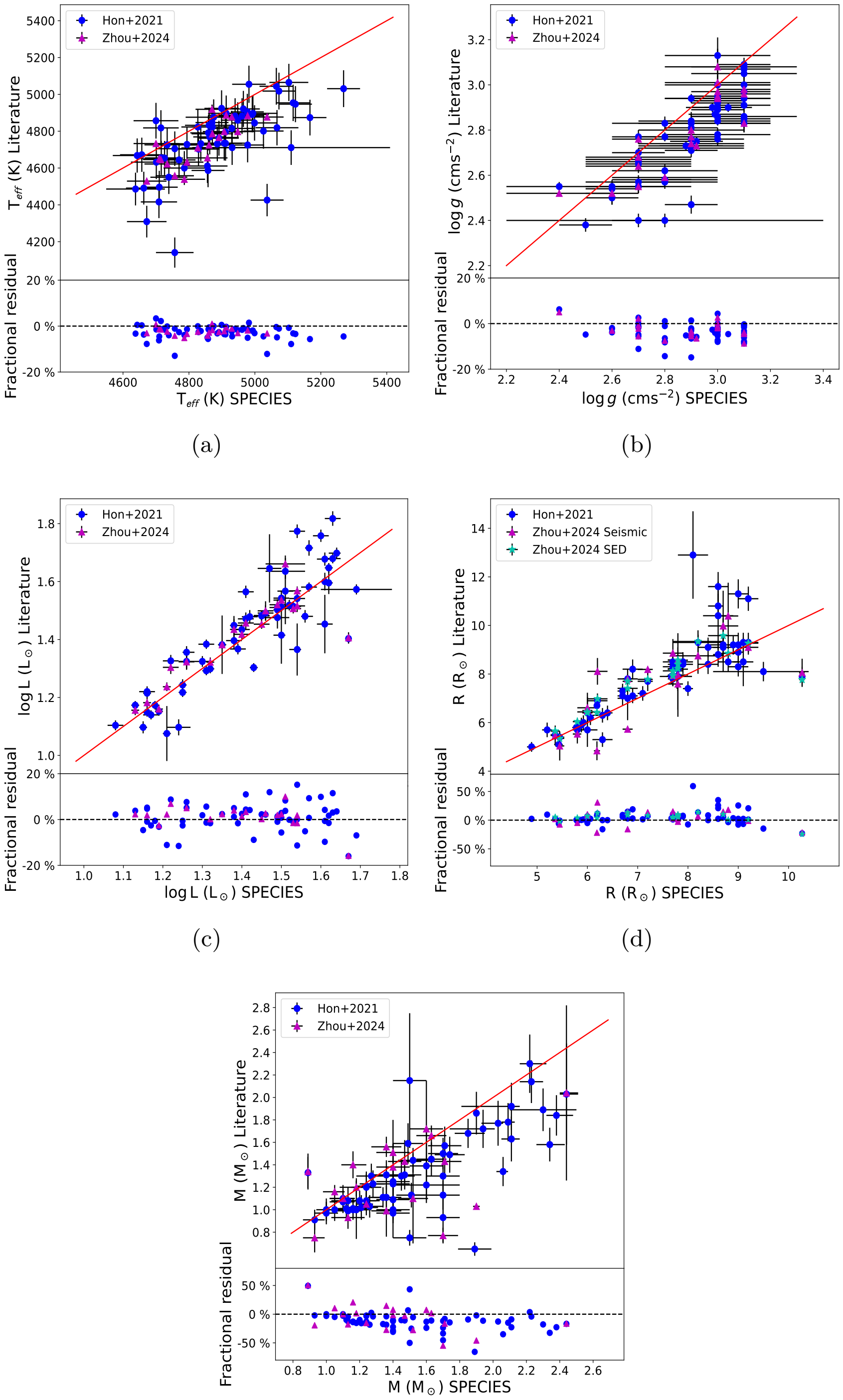

(a) (b)

(c) (d)

(e)

Figure 4.9: Comparison of stellar parameters from Hon et al. (2021), Zhou et al. (2024), and `SPECIES`. The red solid line in the upper panels shows the one-to-one relation. Fractional residuals are computed as $\frac{X_{\text{Literature}} - X_{\texttt{SPECIES}}}{X_{\texttt{SPECIES}}}$, where X denotes a stellar parameter and "Literature" refers to the studies by Hon et al. (2021) and Zhou et al. (2024).

Chapter 5

Summary and conclusion

In this work, we continued the spectroscopic observations of potential progenitors of wide sdB binaries initiated by Uzundag et al. (2022), extending the observed volume-limited sample from 200 to 500 pc. We collected, reduced, and analyzed 419 high-resolution spectra of 235 different stars, with 131 stars observed in multiple epochs. All observations were made using the CORALIE echelle spectrograph at the Swiss 1.2-metre Leonhard Euler Telescope at La Silla observatory. Data reduction was performed using the `CERES` pipeline (Brahm et al., 2017).

After data reduction, we computed radial velocities for each target using `CERES` and measured the radial velocity variations for stars with multi-epoch observations. Following Uzundag et al. (2022), we classified each star based on their RUWE and AEN values, combined with radial velocity variations (if available), into three categories: 1) Potential binary system members, high priority for follow-up; 2) Lower probability binary system members, medium priority; 3) Very low probability binary system members, low priority for follow-up.

We then processed the reduced spectra using the `SPECIES` pipeline (Soto & Jenkins, 2018; Soto et al., 2021), which estimates atmospheric and fundamental physical parameters uniformly using the equivalent width method. The code solves the radiative transfer equation under local thermodynamic equilibrium conditions using ATLAS9 model atmospheres (Castelli & Kurucz, 2003). Physical parameters are derived using the `isochrones` package (Morton, 2015) and MIST stellar models (Dotter, 2016).

We classified evolutionary phases for our stars based on the equivalent evolutionary phases and found that, excluding five stars with problematic spectra, approximately 82% of stars in our sample are RGB stars, while the remaining 18% are on the CHeB phase. The distribution of their atmospheric and physical parameters was also analyzed.

We validated our results by comparing them with the literature, finding good overall agreement, with scatter $\lesssim 13\%$, except for mass, for which the scatter was $\sim 23\%$. This mass discrepancy has also been noted in other systems (Herrero et al., 1992; Martig et al., 2015; Salaris et al., 2018; Tkachenko et al., 2020; Hegedűs et al., 2023; Valle et al., 2024), and we will investigate it further with more data and different mass estimation methods in a future work. Finally, we confirmed the theoretical prediction from Vos et al. (2020) regarding the correlation between sdB progenitor mass and metallicity.

Future work will focus on completing multi-epoch observations for all stars in the 500 pc volume-limited sample and confirming binary systems through radial velocity curve analysis. In fact, four more nights of observations were carried out at the Swiss telescope from October 11 to October 15, 2024. Having a clean sample of binary low-mass red giants within 500 pc is the first intermediate result of this project. The final goal of this work is to obtain their orbital parameters so that they can be used as input for binary population synthesis studies to better understand the stability of the mass transfer.

After having a final sample of confirmed binaries with orbital parameters calculated for both, the possible progenitors (our sample) and the wide sdB stars (sample from Dawson et al., 2024), we will be able to perform a direct comparison of both populations in the same volume. Combining observational results with simulations from theoretical models will further help to understand the physics of mass transfer in the stable RLOF case. Additionally, our results could be used to investigate the observed mass discrepancy between different estimation methods, shedding light on poorly understood processes in the red giant phase for low-mass stars.

APPENDIX A

Final tables

A.1 Radial Velocity measurements

Table A.1: Radial velocity measurements for all stars that are presented in this work. All the stars listed here were observed using the CORALIE instrument. The category is based on the classification method from Uzundag et al. (2022).

Star	RUWE	AEN	Category	JD -2450000	SNR	RV (kms^{-1})	RV error (kms^{-1})
*BCAP	2.027	0.836	1	8650.82	64	-20.962	0.003
				9538.57	62	-20.994	0.005
				9673.89	62	-20.974	0.003
				9737.90	66	-20.976	0.003
				9739.91	29	-20.973	0.003
HD131900	0.907	0.137	2	10140.49	11	-5.87	0.01
				10140.50	35	-6.00	0.03
				10140.50	44	-5.83	0.02
HD196800	0.875	0.11	3	10224.50	31	-63.653	0.008
				10225.49	44	-63.650	0.007
				10227.49	28	-63.644	0.006

HD1000	1.078	0.134	3	10140.93	38	-13.83	0.02
				10140.93	10	-13.84	0.03
*TAUCET	2.634	1.107	1	9537.56	66	-16.505	0.007
				8650.91	25	-16.539	0.004
HD116338	1.445	0.211	1	8651.59	37	-30.528	0.004
				9673.73	43	-29.169	0.003
				9737.70	62	-34.554	0.003
				10140.55	62	-28.362	0.004
HD36787	3.83	0.697	1	9537.71	61	53.483	0.003
				9673.50	32	52.634	0.003
				10140.92	64	50.468	0.004
HD9525	6.283	2.996	1	9538.58	60	12.333	0.004
				9739.93	63	12.478	0.004
				10140.87	39	11.056	0.005
HD190574	4.008	0.502	1	9738.93	52	22.455	0.003
				10140.61	37	26.107	0.004
HD202470	1.888	0.345	2	9739.82	63	26.704	0.003
				10140.63	39	26.769	0.004
HD2132	11.862	1.902	1	9537.54	57	49.697	0.003
				10140.84	38	41.239	0.004
HD8410	9.195	1.325	1	9537.61	38	5.836	0.003
				10140.86	71	5.123	0.004
HD112521	3.899	0.684	1	8651.57	43	7.057	0.004
				9673.73	61	10.772	0.003
				9737.68	61	9.135	0.003
				9738.66	36	9.129	0.003
				10142.56	60	4.130	0.005
HD201013	4.128	0.7	1	8650.86	30	-20.155	0.003
				9538.56	61	-25.732	0.005
				9737.89	41	-18.775	0.003
				9739.90	66	-18.738	0.003
				10140.64	61	-20.557	0.004
HD206005	1.814	0.374	1	8650.85	67	-9.750	0.003
				9539.52	30	-9.257	0.005
				9737.90	63	-8.922	0.003

				9739.91	58	-8.897	0.003
				10140.68	38	-7.801	0.004
HD217614	10.68	2.035	1	8650.79	60	-13.932	0.004
				9538.56	58	-24.688	0.004
				9737.92	60	-11.049	0.004
				9739.93	55	-10.764	0.004
				10140.82	39	-12.981	0.005
HD167936	8.646	1.416	1	8651.70	46	-21.101	0.006
				9673.86	44	-37.331	0.006
				9737.79	57	1.288	0.006
				10140.65	57	3.970	0.007
HD101744	2.788	0.366	1	9738.60	25	0.046	0.003
				10140.53	37	-2.094	0.004
				10142.49	61	-2.014	0.006
HD214941	2.446	0.431	1	8650.91	62	5.070	0.005
				9538.57	28	1.631	0.008
				9737.91	59	0.627	0.005
HD305357	2.447	0.457	1	8650.52	42	-0.737	0.006
				9673.58	53	3.540	0.004
				9737.58	60	0.042	0.005
HD74686	19.337	3.417	1	9673.52	60	47.065	0.003
				9738.45	32	46.279	0.005
				9738.50	62	46.288	0.004
HD83674	2.651	0.475	1	9538.84	57	-3.253	0.004
				9673.55	60	-3.017	0.004
				9738.52	60	-2.894	0.004
HD85885	1.872	0.243	1	8650.55	42	27.063	0.006
				9673.56	58	26.865	0.005
				9738.53	58	34.680	0.005
HD92944	3.552	0.531	1	9738.57	58	18.797	0.003
				10143.48	47	11.942	0.004
				10140.51	41	12.141	0.004
TYC5464-59-1	5.437	0.894	1	9538.83	57	-1.186	0.004
				9673.54	59	-3.504	0.004
				9738.51	60	-4.587	0.004

*14SER	2.567	0.314	1	8650.69	69	-39.984	0.006
				9673.82	58	-39.029	0.007
*29PSC	0.821	0.628	1	8650.92	85	7	2
				10224.71	46	31	1
*PI.SCL	5.214	3.614	1	9537.62	63	5.546	0.003
				10226.63	65	13.259	0.003
BD-025297	3.255	0.464	1	10143.72	28	-4.476	0.004
				10143.83	10	-4.50	0.01
BD-103347	2.558	0.327	1	9739.56	63	23.204	0.003
				10142.50	29	23.656	0.005
BD+003544	5.921	0.82	1	9739.64	60	-6.853	0.003
				10140.58	42	-24.464	0.004
BD+003886	3.225	0.5	1	9738.84	63	-32.587	0.003
				10225.53	31	-32.501	0.005
BD+023359	1.829	0.216	1	9738.80	62	-26.056	0.003
				10225.51	26	-24.729	0.006
BD+124422	1.515	0.227	1	10140.80	37	-61.772	0.004
				9739.86	64	-62.325	0.003
BD+154266A	3.519	0.469	1	9739.88	65	1.380	0.003
				10140.79	37	1.807	0.004
CD-329820	2.094	0.277	1	9739.53	54	-0.311	0.003
				10140.56	44	12.667	0.004
CD-711504	1.786	0.198	1	10143.67	26	22.15	0.01
				10225.55	23	80.85	0.01
CD-75996	1.546	0.158	1	10143.65	29	6.208	0.005
				10225.50	29	6.311	0.005
HD103433	2.318	0.478	1	9739.59	31	120.640	0.004
				10142.52	60	128.284	0.006
HD108047	1.911	0.235	1	9738.64	37	-0.189	0.005
				10142.54	58	-3.438	0.006
HD122602	2.19	0.337	1	9739.58	29	-72.190	0.003
				10142.54	61	-68.323	0.005
HD167108	4.008	0.76	1	9738.82	26	-57.576	0.003
				10225.49	61	-57.938	0.006
HD172039	3.06	0.477	1	9738.86	49	-24.685	0.004

				10140.66	44	-27.331	0.004
HD172642	5.34	0.595	1	10143.74	28	28.97	0.01
				10225.54	14	28.981	0.006
HD176830	1.403	0.152	1	10143.71	25	-54.886	0.005
				10225.58	34	-55.289	0.006
HD177057	7.308	1.081	1	10143.77	14	6.853	0.009
				10225.59	29	0.573	0.005
HD181405	3.312	0.416	1	10143.75	32	-36.085	0.008
				10225.65	19	-38.752	0.005
HD182393	5.635	0.729	1	10226.50	40	-14.023	0.004
				10143.78	14	-16.055	0.009
HD18278	5.464	1.036	1	9537.59	76	21.402	0.003
				10140.90	37	21.781	0.004
HD183249	4.444	0.5	1	9738.89	56	-24.630	0.003
				10140.67	44	-26.000	0.004
HD185051	6.96	0.796	1	9739.71	62	-50.742	0.003
				10140.78	43	-44.309	0.004
HD185452	4.55	0.484	1	10143.79	34	2.827	0.004
				10226.53	38	10.766	0.004
HD185490	6.774	0.92	1	9739.68	38	-89.551	0.003
				10140.81	60	-97.615	0.005
HD186611	6.336	0.959	1	10143.68	41	24.232	0.006
				10226.51	33	21.905	0.005
HD188921	2.038	0.281	1	10143.83	20	-25.93	0.01
				10227.51	33	15.350	0.007
HD190122	5.245	0.999	1	9738.92	63	7.207	0.003
				10140.73	62	3.648	0.003
HD193359	2.157	0.26	1	9739.76	40	43.238	0.003
				10140.61	61	43.437	0.004
HD195326	2.887	0.458	1	9739.83	66	-45.899	0.003
				10140.73	38	-32.890	0.004
HD202714	1.461	0.209	1	9739.84	38	5.251	0.003
				10140.64	60	6.599	0.004
HD21340	2.95	0.498	1	9537.70	58	21.265	0.003
				10140.88	33	21.619	0.005

HD220864	3.578	0.633	1	9538.62	60	2.166	0.003
				10140.84	38	1.597	0.004
HD2259	2.695	0.455	1	9537.55	59	19.789	0.003
				10140.84	39	17.633	0.004
HD29821	3.027	0.533	1	9537.68	59	25.571	0.003
				10225.85	41	26.503	0.004
HD5676	2.104	0.32	1	9537.63	67	83.026	0.003
				10140.85	35	80.847	0.004
HD6019	3.323	0.646	1	9537.57	34	-23.732	0.004
				10140.87	56	-23.188	0.005
HD6030	1.984	0.292	1	9537.58	34	-13.489	0.003
				10140.88	58	-22.646	0.005
HD6254	2.6	0.496	1	9537.66	37	56.734	0.003
				10140.86	58	50.423	0.004
HD73070	2.452	0.265	1	9739.47	41	7.149	0.003
				10226.88	61	6.645	0.004
HD95624	5.923	1.165	1	9738.54	30	-80.716	0.003
				10143.48	59	-71.737	0.005
HD99005	3.129	0.491	1	9738.58	62	1.793	0.003
				10143.49	17	4.335	0.008
HD99330	5.288	0.701	1	9738.55	38	-5.533	0.003
				10143.47	64	-6.037	0.004
TYC5312-953-1	3.077	0.384	1	10224.87	30	-5.993	0.007
				10227.75	38	-5.858	0.006
BD-1119	4.458	0.422	1	10224.69	28	-2.199	0.005
BD-17922	3.873	0.5	1	10224.83	35	43.396	0.004
BD+003575	4.252	0.522	1	9738.76	63	7.324	0.003
BD+02694	3.605	0.511	1	10224.85	36	58.550	0.005
BD+05136	5.644	0.749	1	10224.73	25	-1.85	0.01
BD+153012	3.257	0.496	1	9739.66	66	-20.116	0.003
CD-251745	5.415	0.713	1	10227.78	39	45.458	0.005
CD-3018265	7.218	0.981	1	10224.56	27	70.001	0.005
CD-331236	6.679	0.917	1	10224.77	26	-7.920	0.005
CD-339045	4.688	0.577	1	10143.50	16	-22.026	0.008
CD-371312	3.949	0.477	1	10225.82	38	71.490	0.004

CD-3913785	4.16	0.573	1	10227.59	38	12.734	0.004
CD-431047	4.716	0.745	1	10224.80	32	14.204	0.005
CD-452254	4.204	0.522	1	10226.73	39	33.814	0.004
CD-5012869	9.626	1.085	1	10227.57	38	-24.084	0.004
CD-5112230	5.627	0.674	1	10143.80	39	-22.126	0.004
CD-662575	4.612	0.625	1	10225.69	40	11.258	0.004
HD11664	2.813	0.449	1	10226.79	44	8.546	0.004
HD118601	5.307	0.478	1	9738.71	62	7.346	0.004
HD120	4.638	0.626	1	10227.71	37	15.444	0.005
HD155046	4.55	0.782	1	9738.78	61	-79.815	0.004
HD18416	5.646	0.857	1	10224.78	26	21.523	0.006
HD190896	4.331	0.519	1	10224.51	27	-13.475	0.005
HD196248	3.789	0.552	1	10224.55	32	14.323	0.006
HD197254	3.88	0.608	1	10225.66	31	23.246	0.006
HD197579	4.114	0.668	1	10226.54	43	16.044	0.004
HD2009	3.185	0.429	1	10226.59	40	22.728	0.004
HD201846	5.559	0.985	1	10224.58	27	-13.885	0.007
HD20186	3.364	0.492	1	10225.81	39	29.116	0.004
HD204649	3.696	0.556	1	10224.59	34	60.328	0.005
HD210070	6.199	0.777	1	10225.67	33	26.598	0.005
HD219470	4.383	0.508	1	10225.76	39	-17.98	0.01
HD219775	4.085	0.521	1	10226.58	37	38.476	0.004
HD22176	4.317	0.71	1	10224.81	33	9.716	0.006
HD222051	5.253	0.734	1	10226.76	42	24.118	0.004
HD223619	5.082	0.67	1	10226.77	40	8.144	0.004
HD23213	8.085	1.122	1	10227.84	34	4.784	0.005
HD270913	4.752	0.844	1	10227.87	33	53.417	0.004
HD274522	6.486	0.843	1	10226.70	35	-4.768	0.005
HD43375	4.57	0.536	1	10226.74	38	19.101	0.004
HD4952	4.248	0.616	1	10224.68	30	-1.634	0.009
HD7039	5.945	0.905	1	10225.80	35	7.161	0.004
HD71562	2.914	0.47	1	10226.87	40	2.869	0.004
HD84804	4.201	0.516	1	9739.50	62	19.929	0.003
HD9567	6.408	0.888	1	10224.72	27	-6.356	0.007
TYC8519-263-1	3.865	0.476	1	10226.71	38	28.380	0.004

HD102805	0.924	0.087	2	8651.54	44	-11.575	0.004
				9673.64	61	-11.058	0.003
				9737.53	61	-11.015	0.003
				10142.53	36	-10.802	0.004
HD170105	0.897	0.098	2	8651.66	45	30.608	0.004
				9673.86	61	31.675	0.003
				9737.81	62	31.736	0.003
				10140.65	45	32.271	0.004
HD99891	1.352	0.167	2	8651.50	45	-14.337	0.004
				9673.62	60	-14.473	0.003
				9737.50	32	-14.449	0.003
				10142.51	61	-14.481	0.005
HD202704	1.027	0.141	2	8650.84	56	3.234	0.004
				9737.89	60	3.160	0.004
				10140.63	39	3.110	0.005
HD4145	0.993	0.2	2	9537.53	61	-8.590	0.003
				9739.94	37	-8.495	0.003
				10140.85	61	-8.284	0.004
CD-529252	2.403	0.258	2	10143.81	36	-69.357	0.005
				10227.50	31	-69.302	0.005
CD-581114	1.403	0.162	2	10225.87	35	67.847	0.004
				10227.76	35	67.864	0.004
HD100409	1.724	0.298	2	9738.62	62	2.197	0.003
				10142.52	36	2.209	0.005
HD10268	1.719	0.276	2	9537.62	37	-11.248	0.003
				10140.87	69	-11.257	0.004
HD115541	2.871	0.344	2	9738.68	58	-5.578	0.004
				10142.55	39	-5.563	0.005
HD185544	2.237	0.279	2	9739.79	43	12.965	0.003
				10140.75	61	12.969	0.004
HD22792	1.229	0.171	2	9537.65	60	24.127	0.003
				10140.89	38	23.286	0.004
TYC8373-756-1	1.603	0.148	2	10143.73	26	54.175	0.007
				10225.57	19	54.240	0.006
BD-06908	2.266	0.247	2	10227.81	35	7.919	0.004

BD-09279	1.493	0.181	2	10226.62	37	-3.376	0.004
BD-14302	3.005	0.374	2	10224.74	26	-40.780	0.006
BD-15833	1.819	0.203	2	10225.83	41	17.128	0.004
BD+002249	1.863	0.27	2	10226.85	36	-40.232	0.004
BD+002251	2.98	0.376	2	10226.86	38	-13.727	0.004
BD+0696	1.566	0.178	2	10224.64	32	22.227	0.005
BD+084680	2.341	0.314	2	10224.62	27	-59.605	0.005
BD+09139	1.894	0.211	2	10227.72	36	-45.980	0.004
BD+125070	2.238	0.277	2	10227.68	35	-20.460	0.005
BD+16328	1.597	0.178	2	10227.74	36	-6.828	0.006
CD-242335	2.144	0.24	2	10227.80	40	32.556	0.006
CD-2516784	1.924	0.221	2	10227.69	37	-7.699	0.004
CD-2613981	2.386	0.26	2	10225.62	32	-56.654	0.006
CD-2718	1.896	0.224	2	10225.76	37	-11.169	0.005
CD-2816392	2.428	0.316	2	10227.53	34	-14.939	0.004
CD-3018710	1.738	0.201	2	10224.60	29	7.173	0.005
CD-361284	2.119	0.289	2	10227.83	36	14.723	0.005
CD-3613943	1.898	0.236	2	10227.55	35	-31.937	0.004
CD-66436	2.119	0.287	2	10226.83	40	84.653	0.005
CD-79305	2.945	0.388	2	10226.84	35	17.730	0.006
CD-81204	2.334	0.3	2	10226.80	36	5.258	0.005
CPD-5011378	2.444	0.275	2	10227.61	40	-45.511	0.004
HD120301	2.027	0.22	2	10143.55	14	6.092	0.009
HD148035	2.626	0.341	2	9738.73	60	-17.624	0.004
HD151220	1.797	0.185	2	10143.60	34	-43.220	0.004
HD177668	3.098	0.347	2	10143.69	28	4.700	0.004
HD177668	3.098	0.347	2	10225.60	40	4.717	0.005
HD194898	1.648	0.237	2	10224.49	24	-38.629	0.006
HD195899	2.16	0.222	2	10227.63	40	-30.225	0.004
HD196997	2.408	0.318	2	10227.64	38	8.852	0.004
HD199554	2.31	0.312	2	10224.54	33	78.719	0.004
HD206757	2.051	0.288	2	10224.63	33	-91.930	0.005
HD215767	1.882	0.216	2	10225.72	39	7.443	0.004
HD217365	1.782	0.205	2	10225.74	37	46.883	0.004
HD218120	2.317	0.319	2	10225.75	35	-30.497	0.005

HD221059	1.679	0.241	2	10227.65	39	5.374	0.004
HD221897	1.413	0.144	2	10226.60	37	-7.998	0.004
HD221921	2.182	0.222	2	10224.64	25	-7.296	0.006
HD224485	2.193	0.32	2	10226.78	41	-2.973	0.005
HD25872	2.401	0.238	2	10227.85	34	49.463	0.004
HD34246	1.959	0.234	2	10225.86	37	8.675	0.005
HD45616	1.796	0.258	2	10226.81	39	39.030	0.004
HD7381	2.176	0.279	2	10224.79	29	-22.706	0.005
HD74993	1.589	0.255	2	9738.50	61	5.741	0.003
TYC1172-588-1	1.811	0.191	2	10227.66	34	-12.653	0.005
CD-397574	0.984	0.08	3	8650.60	52	6.018	0.004
				9673.67	41	5.972	0.004
				10140.54	60	5.992	0.005
HD107045	0.975	0.118	3	8650.57	59	-11.651	0.003
				9673.68	60	-11.653	0.003
				9737.64	61	-11.639	0.003
HD114430	0.966	0.123	3	8651.58	41	-15.857	0.004
				9673.72	60	-15.854	0.004
				9737.63	60	-15.842	0.003
HD116845	0.924	0.098	3	8649.54	67	-6.378	0.004
				9673.74	60	-6.380	0.004
				9737.69	60	-6.368	0.004
HD120144	1.373	0.19	3	8650.65	65	-0.653	0.003
				9673.76	63	-0.639	0.003
				9737.70	63	-0.599	0.003
HD122568	1.253	0.111	3	8651.61	40	17.947	0.004
				9673.78	61	17.929	0.003
				9737.72	61	17.940	0.003
HD124461	1.097	0.139	3	8650.67	69	-40.668	0.003
				9673.79	61	-40.676	0.003
				9739.61	60	-40.664	0.003
HD149649	0.954	0.107	3	8651.64	36	7.936	0.005
				9673.82	61	7.982	0.004
				9737.76	61	7.974	0.004
HD157527	0.724	0.208	3	9673.85	62	-52.481	0.003

				9737.77	44	-52.457	0.003
				10140.65	62	-52.529	0.004
HD162157	0.966	0.105	3	8651.68	41	-21.039	0.004
				9673.84	61	-21.038	0.003
				9737.78	61	-21.039	0.003
HD168839	0.828	0.081	3	8650.89	55	14.440	0.003
				9673.87	68	14.418	0.003
				9737.80	62	14.436	0.003
HD171864	1.041	0.125	3	8650.70	71	-17.281	0.003
				9673.87	63	-17.296	0.003
				9737.82	61	-17.280	0.003
HD191716	1.02	0.12	3	8650.80	68	-7.836	0.003
				9673.88	62	-7.843	0.003
				9737.85	61	-7.817	0.003
HD193407	1.013	0.121	3	8651.73	41	-21.182	0.004
				9737.87	41	-21.243	0.003
				10140.74	61	-21.209	0.004
HD195189	0.966	0.127	3	8650.72	62	-24.592	0.003
				9737.88	42	-24.604	0.003
				10140.75	60	-24.592	0.004
HD197790	1.033	0.126	3	8650.89	58	-16.329	0.004
				9737.88	60	-16.345	0.003
				10140.77	44	-16.369	0.004
HD4737	1.093	0.159	3	8650.90	58	12.501	0.004
				9737.92	60	12.463	0.004
				10140.85	38	12.473	0.005
HD96627	1.259	0.157	3	8651.47	51	3.203	0.004
				9673.60	61	3.193	0.003
				9737.47	60	3.216	0.003
HD102216	1.027	0.092	3	9673.70	61	17.875	0.003
				9737.56	61	17.902	0.003
HD116948	0.878	0.107	3	8651.56	44	-18.511	0.004
				9673.75	61	-18.498	0.003
HD119483	1.207	0.146	3	9673.76	62	11.776	0.003
				9737.71	62	11.779	0.003

HD136350	0.998	0.088	3	9673.81	60	-6.101	0.003
				9737.75	60	-6.111	0.003
HD162984	0.945	0.113	3	9673.85	61	-10.015	0.003
				9737.80	60	-10.010	0.003
HD16665	1.154	0.153	3	9538.60	35	11.079	0.003
				10140.91	61	11.104	0.004
HD167768	0.872	0.177	3	8650.81	53	1.622	0.005
				9673.89	61	1.624	0.005
HD176771	1.003	0.161	3	9673.88	61	-10.194	0.004
				9737.82	60	-10.212	0.004
HD188476	0.987	0.108	3	8650.83	58	-22.687	0.003
				9737.84	62	-22.690	0.003
HD189365	0.96	0.114	3	8650.84	54	21.509	0.004
				9737.84	60	21.574	0.004
HD192232	0.986	0.152	3	9538.52	59	-2.543	0.004
				9739.74	53	-2.573	0.003
HD193937	1.354	0.157	3	9538.54	60	-22.422	0.004
				9739.81	47	-22.433	0.003
HD195980	1.193	0.17	3	9739.92	38	-32.273	0.003
				10140.60	64	-32.188	0.004
HD203086	1.044	0.132	3	9737.85	61	-19.470	0.004
				8650.74	61	-19.481	0.003
HD207920	0.937	0.115	3	8650.82	64	9.016	0.003
				9737.90	61	9.008	0.004
HD209154	0.997	0.128	3	8650.78	58	6.350	0.004
				9737.90	59	6.343	0.004
HD213986	0.914	0.182	3	9539.52	62	-1.971	0.003
				9739.91	59	-1.975	0.003
HD219263	1.212	0.321	3	9538.57	65	3.437	0.003
				9739.91	63	3.432	0.003
HD220096	0.926	0.306	3	8650.88	65	16.181	0.008
				10140.83	37	16.16	0.01
HD223700	1.13	0.132	3	8650.92	56	-1.780	0.003
				9737.92	61	-1.797	0.003
HD27956	1.089	0.155	3	9537.69	58	46.109	0.003

				10140.91	36	46.096	0.004
HD3303	0.888	0.152	3	9537.55	59	-9.689	0.003
				9739.93	62	-9.677	0.003
HD745	1.05	0.172	3	9537.54	35	-2.089	0.003
				10140.83	58	-2.076	0.005
HD99783	0.959	0.12	3	9673.61	61	12.558	0.003
				9737.48	54	12.565	0.004
BD-025910	1.317	0.138	3	10226.55	43	-1.569	0.004
BD-07164	1.323	0.125	3	10225.78	35	3.900	0.005
BD+004462	1.329	0.136	3	10225.64	29	-50.72	0.01
BD+0431	1.317	0.129	3	10224.70	27	13.132	0.007
CD-324787	0.981	0.09	3	9738.49	35	0.721	0.003
HD179120	0.995	0.112	3	9737.83	61	-7.142	0.003
HD187562	0.982	0.068	3	10140.76	43	-2.496	0.006
HD194536	1.355	0.128	3	10224.52	28	-21.146	0.005
HD205588	1.005	0.122	3	9737.86	61	5.746	0.003
HD217053	1.317	0.146	3	10225.73	37	2.578	0.004
HD219026	1.149	0.155	3	8650.87	56	-2.864	0.003
HD219026	1.149	0.155	3	9737.93	61	-2.870	0.003
HD26120	1.351	0.161	3	10225.85	41	19.200	0.004
HD40525	1.319	0.207	3	10226.72	36	-0.913	0.005
HD71464	1.285	0.145	3	9673.53	53	39.480	0.005
TYC6951-496-1	1.005	0.122	3	8650.77	62	5.741	0.003

A.2 Atmospheric and physical parameter measurements

Table A.2: `SPECIES` results for stars observed with CORALIE. $P_{\rm MS}$, $P_{\rm RGB}$ and $P_{\rm HB}$ correspond to the probability of the star being on the MS, RGB, or HB, respectively.

Starname	$T_{\rm eff}$ (K)	$\log g$ (cgs)	[Fe/H] (dex)	ξ_t (kms^{-1})	$v_{\rm mac}$ (kms^{-1})	$v \sin i$ (kms^{-1})	Mass ($M_\odot$)	Radius ($R_\odot$)	$\log L$ ($L_\odot$)	Age (Gyr)	EEP	$P_{\rm MS}$	$P_{\rm RGB}$	$P_{\rm HB}$
HD116338	5126±50	3.12±0.12	0.15±0.04	1.34±0.05	3.48±0.43	5.27±0.44	$2.57^{+0.03}_{-0.04}$	$8.56^{+0.11}_{-0.11}$	$1.64^{+0.01}_{-0.01}$	$0.58^{+0.02}_{-0.01}$	$527.2^{+1.2}_{-1.2}$	0	0.98	0.02
HD36787	4739±56	2.79±0.14	0.11±0.04	1.19±0.08	3.28±0.51	5.07±0.52	$1.24^{+0.09}_{-0.08}$	$6.94^{+0.12}_{-0.12}$	$1.31^{+0.01}_{-0.01}$	$5.31^{+1.29}_{-0.99}$	$506.6^{+0.9}_{-0.7}$	0	1	0
HD9525	4709±55	2.56±0.13	0.04±0.04	1.13±0.09	3.66±0.56	5.69±0.57	$1.44^{+0.12}_{-0.13}$	$8.58^{+0.31}_{-0.29}$	$1.51^{+0.02}_{-0.02}$	$3.07^{+1.05}_{-0.73}$	$514.2^{+1.3}_{-1.5}$	0	1	0
HD190574	4793±52	2.89±0.13	0.06±0.04	1.21±0.07	3.20±0.49	4.96±0.51	$0.98^{+0.03}_{-0.02}$	$5.15^{+0.08}_{-0.08}$	$1.05^{+0.01}_{-0.01}$	$12.59^{+0.65}_{-1.17}$	$499.6^{+0.5}_{-0.6}$	0	1	0
HD202470	4726±56	2.92±0.13	0.13±0.04	1.04±0.10	3.04±0.48	5.03±0.49	$1.21^{+0.12}_{-0.10}$	$5.78^{+0.14}_{-0.13}$	$1.17^{+0.02}_{-0.02}$	$5.83^{+1.97}_{-1.54}$	$501.1^{+1.1}_{-1.0}$	0	1	0
HD2132	4911±50	2.90±0.10	-0.37±0.04	1.22±0.04	3.41±0.46	4.69±0.48	$1.49^{+0.09}_{-0.09}$	$8.97^{+0.13}_{-0.12}$	$1.61^{+0.01}_{-0.01}$	$2.11^{+0.46}_{-0.34}$	$518.6^{+0.7}_{-0.8}$	0	1	0
HD8410	4897±50	2.88±0.09	-0.04±0.04	1.07±0.05	3.41±0.46	5.07±0.46	$1.42^{+0.11}_{-0.10}$	$6.17^{+0.17}_{-0.16}$	$1.28^{+0.02}_{-0.02}$	$2.96^{+0.86}_{-0.64}$	$503.4^{+1.0}_{-1.2}$	0	1	0
*14SER	4957±59	2.74±0.13	-0.09±0.04	0.30±0.28	3.78±0.53	5.19±0.54	$2.28^{+0.12}_{-0.13}$	$9.92^{+0.16}_{-0.15}$	$1.76^{+0.01}_{-0.01}$	$0.83^{+0.18}_{-0.17}$	$669.3^{+1.1}_{-2.6}$	0	0	1
*PI.SCL	4858±50	2.72±0.11	-0.14±0.04	1.23±0.05	3.62±0.51	5.06±0.52	$1.68^{+0.11}_{-0.11}$	$9.08^{+0.23}_{-0.24}$	$1.61^{+0.01}_{-0.01}$	$1.63^{+0.35}_{-0.28}$	$516.5^{+1.4}_{-1.3}$	0	0.98	0.01
BD+002249	4927±57	2.36±0.15	-0.05±0.04	1.41±0.07	4.41±0.63	3.54±0.78	$0.89^{+0.01}_{-0.01}$	$10.29^{+0.07}_{-0.05}$	$1.67^{+0.00}_{-0.00}$	$13.06^{+0.31}_{-0.45}$	$660.9^{+0.7}_{-0.9}$	0	0	1
BD+002251	4888±51	3.07±0.12	0.07±0.04	1.15±0.07	3.06±0.44	3.79±0.50	$2.08^{+0.04}_{-0.05}$	$8.53^{+0.16}_{-0.16}$	$1.54^{+0.02}_{-0.02}$	$1.09^{+0.05}_{-0.08}$	$532.5^{+110.9}_{-15.3}$	0	0.7	0.3
BD+003544	4875±50	2.78±0.12	-0.34±0.04	1.00±0.07	3.56±0.50	4.92±0.51	$0.90^{+0.01}_{-0.01}$	$5.27^{+0.11}_{-0.10}$	$1.12^{+0.02}_{-0.02}$	$13.01^{+0.36}_{-0.66}$	$501.3^{+0.7}_{-0.7}$	0	1	0
BD+003575	4802±50	2.87±0.10	-0.00±0.04	1.13±0.05	3.25±0.46	5.05±0.47	$1.11^{+0.08}_{-0.07}$	$6.61^{+0.32}_{-0.28}$	$1.28^{+0.04}_{-0.04}$	$7.35^{+1.94}_{-1.50}$	$506.3^{+1.3}_{-1.2}$	0	1	0
BD+003886	4748±60	2.91±0.14	0.19±0.04	1.18±0.09	3.09±0.50	5.16±0.51	$1.57^{+0.12}_{-0.14}$	$7.31^{+0.22}_{-0.20}$	$1.38^{+0.03}_{-0.03}$	$2.51^{+0.95}_{-0.52}$	$507.2^{+1.4}_{-2.0}$	0	1	0
BD+004462	5519±300	3.33±0.24	-0.05±0.15	0.81±1.00	4.19±0.48	0.00±0.00	$1.94^{+0.05}_{-0.06}$	$5.00^{+0.11}_{-0.09}$	$1.25^{+0.02}_{-0.02}$	$1.15^{+0.04}_{-0.03}$	$489.2^{+3.2}_{-3.0}$	0	1	0
BD+023359	4921±50	2.97±0.10	-0.11±0.04	1.18±0.05	3.31±0.45	5.03±0.45	$1.35^{+0.08}_{-0.08}$	$7.05^{+0.14}_{-0.12}$	$1.38^{+0.01}_{-0.01}$	$3.43^{+0.74}_{-0.56}$	$508.1^{+0.8}_{-0.8}$	0	1	0

Continued on next page

Starname	$T_{\rm eff}$ (K)	$\log g$ (cgs)	[Fe/H] (dex)	ξ_t (kms^{-1})	$v_{\rm mac}$ (kms^{-1})	$v \sin i$ (kms^{-1})	Mass ($M_\odot$)	Radius ($R_\odot$)	$\log L$ ($L_\odot$)	Age (Gyr)	EEP	$P_{\rm MS}$	$P_{\rm RGB}$	$P_{\rm HB}$
BD+02694	5170±50	3.40±0.12	-0.02±0.04	1.14±0.07	3.09±0.38	3.93±0.49	$1.80^{+0.06}_{-0.07}$	$4.73^{+0.11}_{-0.11}$	$1.15^{+0.03}_{-0.03}$	$1.41^{+0.16}_{-0.10}$	$489.1^{+1.5}_{-1.5}$	0	1	0
BD+0431	4935±82	3.13±0.20	-0.09±0.05	1.20±0.12	3.04±0.54	4.45±0.72	$1.18^{+0.09}_{-0.09}$	$5.53^{+0.14}_{-0.13}$	$1.17^{+0.02}_{-0.02}$	$5.44^{+1.68}_{-1.18}$	$499.8^{+1.2}_{-1.1}$	0	1	0
BD+05136	5062±102	3.06±0.21	-0.12±0.05	0.70±0.30	3.45±0.58	3.95±0.72	$2.09^{+0.13}_{-0.06}$	$8.27^{+0.32}_{-0.76}$	$1.60^{+0.03}_{-0.06}$	$0.92^{+0.08}_{-0.17}$	$644.6^{+6.6}_{-117.0}$	0	0.34	0.67
BD+0696	4870±62	2.87±0.15	-0.15±0.04	1.16±0.09	3.38±0.51	3.30±0.67	$1.09^{+0.15}_{-0.11}$	$5.29^{+0.37}_{-0.55}$	$1.14^{+0.06}_{-0.10}$	$6.98^{+3.24}_{-2.48}$	$499.0^{+2.2}_{-3.3}$	0	1	0
BD+084680	4700±76	2.79±0.19	0.13±0.04	1.23±0.12	3.23±0.57	4.27±0.73	$1.29^{+0.08}_{-0.06}$	$7.74^{+0.14}_{-0.14}$	$1.39^{+0.02}_{-0.01}$	$4.83^{+0.80}_{-0.81}$	$510.0^{+0.7}_{-0.6}$	0	1	0
BD+09139	4889±64	2.99±0.15	0.09±0.04	1.01±0.11	3.19±0.49	3.38±0.59	$1.44^{+0.10}_{-0.12}$	$5.78^{+0.14}_{-0.14}$	$1.21^{+0.02}_{-0.02}$	$3.12^{+1.10}_{-0.63}$	$500.6^{+1.1}_{-1.2}$	0	1	0
BD+124422	4697±56	2.92±0.13	0.14±0.04	1.11±0.09	2.99±0.48	4.94±0.49	$1.02^{+0.05}_{-0.03}$	$6.66^{+0.09}_{-0.09}$	$1.24^{+0.01}_{-0.01}$	$11.36^{+1.36}_{-1.58}$	$507.2^{+0.6}_{-0.6}$	0	1	0
BD+125070	4749±50	2.81±0.12	-0.18±0.04	1.07±0.08	3.26±0.49	4.78±0.58	$1.14^{+0.08}_{-0.08}$	$8.39^{+0.23}_{-0.22}$	$1.49^{+0.02}_{-0.02}$	$5.95^{+1.61}_{-1.11}$	$513.8^{+1.0}_{-0.9}$	0	1	0
BD+153012	4620±73	2.63±0.17	0.24±0.04	1.27±0.11	3.43±0.41	5.10±0.41	$1.20^{+0.09}_{-0.10}$	$8.27^{+0.12}_{-0.12}$	$1.41^{+0.01}_{-0.01}$	$6.69^{+2.17}_{-1.31}$	$512.3^{+1.1}_{-0.8}$	0	1	0
BD+154266A	4661±53	2.79±0.13	0.13±0.04	1.20±0.08	3.15±0.51	4.97±0.51	$1.00^{+0.03}_{-0.02}$	$7.24^{+0.16}_{-0.15}$	$1.29^{+0.02}_{-0.01}$	$12.45^{+0.73}_{-1.26}$	$509.9^{+0.7}_{-0.7}$	0	1	0
BD+16328	5378±50	3.30±0.12	-0.02±0.04	1.29±0.06	3.83±0.41	4.69±0.52	$2.19^{+0.04}_{-0.07}$	$6.62^{+0.13}_{-0.12}$	$1.44^{+0.02}_{-0.02}$	$0.83^{+0.05}_{-0.03}$	$519.8^{+1.9}_{-2.0}$	0	1	0
BD-025297	5036±67	3.20±0.16	0.17±0.04	1.23±0.10	3.12±0.47	3.64±0.58	$2.26^{+0.08}_{-0.13}$	$7.36^{+0.24}_{-0.23}$	$1.47^{+0.03}_{-0.03}$	$0.83^{+0.13}_{-0.07}$	$522.3^{+2.8}_{-2.7}$	0	1	0
BD-025910	5175±50	3.31±0.12	0.13±0.04	1.20±0.06	3.26±0.40	3.80±0.43	$2.01^{+0.11}_{-0.03}$	$5.97^{+0.13}_{-0.13}$	$1.32^{+0.02}_{-0.02}$	$1.14^{+0.04}_{-0.15}$	$497.9^{+17.6}_{-2.2}$	0	1	0
BD-06908	4862±57	3.00±0.14	-0.04±0.04	1.16±0.08	3.13±0.48	3.57±0.55	$1.27^{+0.09}_{-0.09}$	$5.64^{+0.14}_{-0.13}$	$1.19^{+0.02}_{-0.02}$	$4.42^{+1.25}_{-0.86}$	$500.2^{+1.0}_{-1.0}$	0	1	0
BD-07164	5125±57	3.38±0.14	-0.04±0.04	1.08±0.09	3.02±0.41	3.76±0.55	$1.60^{+0.07}_{-0.09}$	$4.67^{+0.09}_{-0.09}$	$1.10^{+0.02}_{-0.02}$	$1.98^{+0.37}_{-0.22}$	$491.8^{+1.7}_{-1.6}$	0	1	0
BD-09279	5077±53	3.17±0.12	-0.01±0.04	1.10±0.08	3.28±0.43	3.71±0.53	$1.60^{+0.09}_{-0.08}$	$5.38^{+0.14}_{-0.14}$	$1.20^{+0.02}_{-0.02}$	$2.00^{+0.36}_{-0.27}$	$496.8^{+1.6}_{-1.8}$	0	1	0
BD-103347	4715±54	3.09±0.13	0.20±0.04	1.06±0.09	2.71±0.44	4.95±0.45	$1.24^{+0.06}_{-0.04}$	$5.80^{+0.09}_{-0.08}$	$1.16^{+0.01}_{-0.01}$	$5.82^{+0.58}_{-0.80}$	$500.6^{+0.6}_{-0.6}$	0	1	0
BD-1119	4934±64	2.88±0.18	0.12±0.04	1.54±0.10	3.55±0.39	4.15±0.43	$2.07^{+0.06}_{-0.08}$	$8.79^{+0.33}_{-0.24}$	$1.57^{+0.03}_{-0.02}$	$1.13^{+0.07}_{-0.09}$	$639.8^{+5.7}_{-126.7}$	0	0.39	0.61
BD-14302	4807±68	3.02±0.16	-0.01±0.04	1.14±0.10	3.00±0.50	3.67±0.66	$1.17^{+0.07}_{-0.08}$	$5.61^{+0.12}_{-0.11}$	$1.17^{+0.02}_{-0.02}$	$6.03^{+1.57}_{-1.08}$	$500.3^{+1.1}_{-1.0}$	0	1	0

Continued on next page

Starname	$T_{\rm eff}$ (K)	$\log g$ (cgs)	[Fe/H] (dex)	ξ_t (kms^{-1})	$v_{\rm mac}$ (kms^{-1})	$v \sin i$ (kms^{-1})	Mass ($M_\odot$)	Radius ($R_\odot$)	$\log L$ ($L_\odot$)	Age (Gyr)	EEP	$P_{\rm MS}$	$P_{\rm RGB}$	$P_{\rm HB}$
BD-15833	4982±51	3.12±0.12	-0.02±0.04	1.09±0.07	3.16±0.43	3.43±0.50	$1.45^{+0.09}_{-0.08}$	$6.42^{+0.13}_{-0.12}$	$1.31^{+0.02}_{-0.02}$	$2.87^{+0.59}_{-0.47}$	$504.6^{+0.9}_{-1.0}$	0	1	0
BD-17922	4790±58	2.99±0.14	-0.07±0.04	1.08±0.09	3.01±0.48	3.06±0.59	$1.00^{+0.06}_{-0.05}$	$5.15^{+0.09}_{-0.10}$	$1.09^{+0.02}_{-0.02}$	$10.03^{+2.05}_{-1.84}$	$499.2^{+0.8}_{-0.8}$	0	1	0
CD-242335	5142±58	3.21±0.14	-0.00±0.04	1.03±0.09	3.35±0.44	4.79±0.57	$1.95^{+0.12}_{-0.08}$	$6.57^{+0.21}_{-0.20}$	$1.39^{+0.03}_{-0.03}$	$1.13^{+0.12}_{-0.15}$	$502.0^{+18.8}_{-2.0}$	0	1	0
CD-2516784	4899±52	2.98±0.13	-0.00±0.04	1.14±0.07	3.25±0.47	3.20±0.62	$1.51^{+0.09}_{-0.09}$	$6.32^{+0.15}_{-0.15}$	$1.30^{+0.02}_{-0.02}$	$2.52^{+0.57}_{-0.40}$	$503.7^{+1.1}_{-1.4}$	0	1	0
CD-251745	5119±61	3.10±0.14	-0.33±0.05	1.08±0.09	3.49±0.47	3.60±0.62	$1.46^{+0.10}_{-0.11}$	$5.70^{+0.17}_{-0.16}$	$1.27^{+0.02}_{-0.02}$	$2.27^{+0.67}_{-0.41}$	$502.1^{+1.2}_{-1.2}$	0	1	0
CD-2613981	4805±96	2.88±0.21	0.03±0.04	0.76±0.26	3.25±0.60	3.61±0.70	$0.98^{+0.03}_{-0.02}$	$5.97^{+0.15}_{-0.13}$	$1.16^{+0.02}_{-0.02}$	$12.52^{+0.65}_{-1.11}$	$504.2^{+0.8}_{-0.8}$	0	1	0
CD-2718	5198±50	3.29±0.12	-0.07±0.04	1.08±0.07	3.36±0.40	3.79±0.47	$1.92^{+0.04}_{-0.05}$	$5.79^{+0.15}_{-0.14}$	$1.31^{+0.03}_{-0.02}$	$1.13^{+0.07}_{-0.03}$	$497.5^{+1.5}_{-1.4}$	0	1	0
CD-2816392	4899±54	3.01±0.13	0.09±0.04	1.18±0.08	3.19±0.47	3.76±0.52	$1.31^{+0.09}_{-0.08}$	$5.72^{+0.13}_{-0.13}$	$1.18^{+0.02}_{-0.02}$	$4.35^{+0.99}_{-0.79}$	$500.4^{+0.9}_{-0.9}$	0	1	0
CD-3018265	4948±76	2.97±0.17	0.15±0.04	1.14±0.13	3.35±0.53	3.59±0.62	$2.09^{+0.04}_{-0.04}$	$8.55^{+0.38}_{-0.57}$	$1.52^{+0.05}_{-0.05}$	$1.11^{+0.05}_{-0.06}$	$530.4^{+113.0}_{-8.8}$	0	0.65	0.35
CD-3018710	4799±60	2.88±0.14	-0.16±0.04	1.12±0.09	3.22±0.50	3.23±0.69	$1.37^{+0.04}_{-0.01}$	$6.95^{+0.10}_{-0.12}$	$1.34^{+0.01}_{-0.01}$	$3.68^{+0.12}_{-0.41}$	$507.5^{+0.5}_{-0.7}$	0	1	0
CD-324787	5209±50	3.23±0.09	-0.04±0.04	1.14±0.05	3.49±0.39	5.04±0.41	$2.25^{+0.04}_{-0.05}$	$7.02^{+0.12}_{-0.12}$	$1.50^{+0.01}_{-0.02}$	$0.76^{+0.04}_{-0.03}$	$522.0^{+1.6}_{-1.6}$	0	1	0
CD-329820	4849±68	3.21±0.16	0.31±0.04	1.04±0.12	2.72±0.46	4.85±0.47	$1.38^{+0.09}_{-0.09}$	$4.98^{+0.09}_{-0.09}$	$1.05^{+0.01}_{-0.01}$	$4.17^{+1.08}_{-0.78}$	$495.4^{+0.7}_{-0.7}$	0	1	0
CD-331236	4800±65	3.09±0.15	0.11±0.04	1.09±0.11	2.84±0.47	3.63±0.63	$1.24^{+0.09}_{-0.09}$	$5.52^{+0.13}_{-0.12}$	$1.15^{+0.02}_{-0.02}$	$5.29^{+1.43}_{-1.07}$	$499.3^{+1.1}_{-0.9}$	0	1	0
CD-339045	5026±111	3.29±0.27	0.12±0.06	1.44±0.25	2.98±0.44	3.82±0.69	$1.43^{+0.11}_{-0.13}$	$5.71^{+0.14}_{-0.12}$	$1.19^{+0.02}_{-0.02}$	$3.21^{+1.24}_{-0.67}$	$500.2^{+1.0}_{-1.2}$	0	1	0
CD-361284	5097±55	3.08±0.14	0.06±0.04	1.14±0.08	3.48±0.46	4.33±0.50	$2.44^{+0.05}_{-0.05}$	$8.00^{+0.16}_{-0.16}$	$1.59^{+0.02}_{-0.02}$	$0.65^{+0.03}_{-0.02}$	$525.9^{+1.3}_{-1.3}$	0	1	0
CD-3613943	4954±59	3.10±0.14	0.16±0.04	1.14±0.09	3.12±0.46	3.56±0.54	$1.73^{+0.11}_{-0.12}$	$6.50^{+0.21}_{-0.20}$	$1.32^{+0.03}_{-0.03}$	$1.75^{+0.42}_{-0.26}$	$500.7^{+2.1}_{-2.0}$	0	1	0
CD-371312	4786±63	2.36±0.16	0.07±0.04	1.33±0.09	4.15±0.64	4.11±0.74	$1.36^{+0.09}_{-0.09}$	$9.20^{+0.20}_{-0.21}$	$1.54^{+0.02}_{-0.02}$	$3.73^{+0.96}_{-0.72}$	$516.3^{+1.0}_{-1.0}$	0	1	0
CD-3913785	4798±71	2.37±0.18	0.16±0.04	1.32±0.10	4.16±0.65	3.88±0.68	$0.96^{+0.06}_{-0.03}$	$10.70^{+0.26}_{-0.11}$	$1.66^{+0.02}_{-0.01}$	$11.88^{+1.25}_{-2.18}$	$663.0^{+2.9}_{-3.0}$	0	0	1
CD-397574	5269±50	3.24±0.10	0.04±0.04	1.33±0.05	3.63±0.40	6.31±0.44	$2.48^{+0.04}_{-0.05}$	$7.98^{+0.22}_{-0.22}$	$1.61^{+0.02}_{-0.02}$	$0.61^{+0.02}_{-0.02}$	$525.1^{+1.6}_{-1.7}$	0	1	0

Continued on next page

Starname	T_{eff} (K)	$\log g$ (cgs)	[Fe/H] (dex)	ξ_t (kms^{-1})	v_{mac} (kms^{-1})	$v \sin i$ (kms^{-1})	Mass ($M_{\odot}$)	Radius ($R_{\odot}$)	$\log L$ ($L_{\odot}$)	Age (Gyr)	EEP	P_{MS}	P_{RGB}	P_{HB}
CD-431047	5146±68	3.38±0.16	-0.04±0.04	1.08±0.10	3.06±0.45	3.05±0.69	$1.63^{+0.08}_{-0.09}$	$4.82^{+0.17}_{-0.16}$	$1.13^{+0.03}_{-0.03}$	$1.87^{+0.34}_{-0.23}$	$492.5^{+1.8}_{-1.8}$	0	1	0
CD-452254	4859±55	3.08±0.13	0.08±0.04	1.07±0.08	2.98±0.45	3.37±0.59	$1.34^{+0.09}_{-0.09}$	$5.43^{+0.09}_{-0.08}$	$1.15^{+0.01}_{-0.01}$	$3.95^{+1.05}_{-0.75}$	$498.7^{+0.7}_{-0.7}$	0	1	0
CD-5012869	4752±86	2.85±0.21	0.24±0.04	1.34±0.12	3.26±0.41	4.25±0.44	$1.38^{+0.14}_{-0.13}$	$7.77^{+0.62}_{-0.54}$	$1.39^{+0.07}_{-0.06}$	$4.05^{+1.60}_{-1.13}$	$510.0^{+2.4}_{-2.3}$	0	1	0
CD-5112230	5103±56	3.40±0.13	-0.15±0.04	0.93±0.09	2.92±0.39	3.29±0.55	$1.28^{+0.18}_{-0.17}$	$3.41^{+0.66}_{-0.55}$	$0.84^{+0.15}_{-0.15}$	$3.81^{+2.46}_{-1.35}$	$483.1^{+5.9}_{-5.5}$	0	1	0
CD-529252	4961±54	3.12±0.12	-0.40±0.05	1.00±0.08	3.11±0.43	3.33±0.62	$1.00^{+0.07}_{-0.07}$	$5.24^{+0.12}_{-0.11}$	$1.16^{+0.02}_{-0.02}$	$8.05^{+2.07}_{-1.59}$	$499.5^{+1.1}_{-1.0}$	0	1	0
CD-581114	4930±67	2.96±0.17	0.05±0.04	1.20±0.10	3.33±0.52	5.01±0.54	$1.52^{+0.09}_{-0.09}$	$5.45^{+0.09}_{-0.09}$	$1.19^{+0.01}_{-0.01}$	$2.49^{+0.51}_{-0.41}$	$498.2^{+1.2}_{-1.8}$	0	1	0
CD-662575	4942±55	2.90±0.14	-0.05±0.04	1.25±0.07	3.46±0.50	4.44±0.57	$2.07^{+0.04}_{-0.03}$	$8.36^{+0.19}_{-0.36}$	$1.58^{+0.02}_{-0.04}$	$1.01^{+0.08}_{-0.05}$	$643.1^{+1.6}_{-110.8}$	0	0.26	0.74
CD-66436	4875±85	3.12±0.20	-0.09±0.04	0.69±0.21	2.93±0.53	4.34±0.58	$1.15^{+0.11}_{-0.10}$	$4.89^{+0.09}_{-0.08}$	$1.08^{+0.02}_{-0.02}$	$5.98^{+2.18}_{-1.65}$	$496.0^{+1.4}_{-1.2}$	0	1	0
CD-711504	5024±193	2.77±0.20	-0.33±0.08	0.98±0.31	3.88±0.51	5.62±0.74	$0.93^{+0.05}_{-0.03}$	$6.69^{+0.13}_{-0.12}$	$1.30^{+0.01}_{-0.01}$	$12.04^{+1.03}_{-1.76}$	$508.5^{+0.8}_{-0.8}$	0	1	0
CD-75996	5074±69	3.25±0.17	0.19±0.04	1.16±0.11	3.13±0.48	4.93±0.53	$1.53^{+0.08}_{-0.08}$	$5.79^{+0.14}_{-0.13}$	$1.20^{+0.02}_{-0.02}$	$2.68^{+0.50}_{-0.38}$	$499.8^{+1.3}_{-1.6}$	0	1	0
CD-79305	5148±73	3.10±0.17	-0.13±0.04	0.91±0.12	3.56±0.51	4.45±0.59	$1.97^{+0.10}_{-0.17}$	$6.84^{+0.16}_{-0.15}$	$1.44^{+0.02}_{-0.03}$	$1.04^{+0.28}_{-0.13}$	$509.5^{+13.0}_{-4.4}$	0	1	0
CD-81204	5129±52	3.19±0.13	-0.22±0.04	1.12±0.07	3.37±0.43	3.32±0.53	$1.43^{+0.08}_{-0.09}$	$5.15^{+0.10}_{-0.10}$	$1.18^{+0.02}_{-0.02}$	$2.57^{+0.56}_{-0.41}$	$497.8^{+0.9}_{-0.9}$	0	1	0
CPD-5011378	4858±66	3.01±0.15	0.29±0.04	1.06±0.12	3.10±0.49	3.19±0.62	$1.59^{+0.08}_{-0.09}$	$6.23^{+0.13}_{-0.13}$	$1.25^{+0.02}_{-0.02}$	$2.54^{+0.53}_{-0.38}$	$501.2^{+1.5}_{-1.7}$	0	1	0
HD100409	5063±50	3.10±0.12	0.24±0.04	1.27±0.07	3.38±0.44	5.66±0.45	$2.64^{+0.07}_{-0.37}$	$9.00^{+0.15}_{-0.15}$	$1.66^{+0.03}_{-0.02}$	$0.56^{+0.33}_{-0.03}$	$528.3^{+129.2}_{-2.0}$	0	0.69	0.31
HD101744	4964±50	3.05±0.13	-0.09±0.04	1.17±0.06	3.25±0.46	4.91±0.47	$1.56^{+0.08}_{-0.09}$	$6.68^{+0.13}_{-0.13}$	$1.36^{+0.02}_{-0.02}$	$2.10^{+0.41}_{-0.30}$	$505.6^{+1.1}_{-1.3}$	0	1	0
HD102216	5140±50	3.10±0.11	0.14±0.04	1.26±0.05	3.56±0.44	4.07±0.46	$2.41^{+0.05}_{-0.06}$	$7.73^{+0.18}_{-0.19}$	$1.54^{+0.02}_{-0.02}$	$0.70^{+0.04}_{-0.03}$	$523.5^{+1.5}_{-1.5}$	0	1	0
HD10268	4700±71	3.01±0.16	0.39±0.04	1.18±0.12	2.88±0.35	5.36±0.35	$1.68^{+0.09}_{-0.09}$	$8.13^{+0.12}_{-0.12}$	$1.43^{+0.01}_{-0.01}$	$2.23^{+0.44}_{-0.33}$	$508.7^{+1.6}_{-1.9}$	0	1	0
HD102805	5168±50	3.14±0.10	0.10±0.04	1.22±0.05	3.55±0.41	5.47±0.42	$2.40^{+0.04}_{-0.05}$	$7.62^{+0.14}_{-0.14}$	$1.54^{+0.02}_{-0.02}$	$0.69^{+0.03}_{-0.02}$	$523.1^{+1.3}_{-1.3}$	0	1	0
HD107045	5156±50	2.93±0.09	-0.04±0.04	1.26±0.04	3.90±0.46	5.22±0.47	$2.26^{+0.08}_{-0.10}$	$9.30^{+0.20}_{-0.24}$	$1.70^{+0.02}_{-0.02}$	$0.80^{+0.15}_{-0.10}$	$662.5^{+4.8}_{-4.2}$	0	0.08	0.92

Continued on next page

Starname	$T_{\rm eff}$ (K)	$\log g$ (cgs)	[Fe/H] (dex)	ξ_t (kms^{-1})	$v_{\rm mac}$ (kms^{-1})	$v \sin i$ (kms^{-1})	Mass ($M_\odot$)	Radius ($R_\odot$)	$\log L$ ($L_\odot$)	Age (Gyr)	EEP	$P_{\rm MS}$	$P_{\rm RGB}$	$P_{\rm HB}$
HD108047	5112±50	3.19±0.10	-0.19±0.04	0.84±0.08	3.32±0.40	5.28±0.42	$1.71^{+0.10}_{-0.10}$	$5.52^{+0.10}_{-0.10}$	$1.26^{+0.02}_{-0.02}$	$1.49^{+0.28}_{-0.22}$	$498.2^{+1.4}_{-1.3}$	0	1	0
HD112521	5217±50	3.12±0.10	-0.01±0.04	1.36±0.04	3.71±0.42	5.56±0.43	$2.14^{+0.21}_{-0.07}$	$8.48^{+0.23}_{-0.31}$	$1.61^{+0.03}_{-0.02}$	$0.92^{+0.09}_{-0.23}$	$646.3^{+6.8}_{-117.4}$	0	0.31	0.69
HD114430	5158±50	2.90±0.11	-0.04±0.04	1.34±0.04	3.97±0.47	4.40±0.51	$2.23^{+0.07}_{-0.09}$	$9.22^{+0.15}_{-0.16}$	$1.69^{+0.01}_{-0.02}$	$0.84^{+0.14}_{-0.09}$	$661.4^{+4.2}_{-3.1}$	0	0.01	0.99
HD115541	5217±50	3.37±0.11	-0.15±0.04	0.81±0.09	3.27±0.38	5.08±0.40	$1.73^{+0.05}_{-0.07}$	$4.94^{+0.10}_{-0.10}$	$1.18^{+0.02}_{-0.02}$	$1.46^{+0.14}_{-0.09}$	$493.2^{+1.3}_{-1.2}$	0	1	0
HD11664	4940±50	2.75±0.14	-0.03±0.04	1.45±0.06	3.74±0.53	4.45±0.55	$2.03^{+0.13}_{-0.03}$	$8.98^{+0.21}_{-0.19}$	$1.63^{+0.02}_{-0.02}$	$1.12^{+0.04}_{-0.19}$	$646.3^{+8.2}_{-7.6}$	0	0.03	0.97
HD116845	5314±50	3.11±0.09	0.01±0.04	1.35±0.04	3.99±0.42	4.88±0.43	$2.60^{+0.04}_{-0.04}$	$8.84^{+0.17}_{-0.17}$	$1.71^{+0.01}_{-0.02}$	$0.53^{+0.01}_{-0.01}$	$528.9^{+1.5}_{-1.6}$	0	1	0
HD116948	5177±50	3.07±0.09	0.05±0.04	1.36±0.04	3.70±0.43	4.14±0.47	$2.42^{+0.06}_{-0.30}$	$8.33^{+0.18}_{-0.15}$	$1.61^{+0.01}_{-0.01}$	$0.65^{+0.33}_{-0.03}$	$528.6^{+118.3}_{-1.6}$	0	0.71	0.29
HD118601	4940±72	3.38±0.15	0.29±0.04	0.92±0.14	2.59±0.43	4.74±0.46	$1.39^{+0.17}_{-0.17}$	$3.49^{+0.74}_{-0.60}$	$0.79^{+0.17}_{-0.16}$	$3.93^{+2.37}_{-1.28}$	$483.0^{+5.2}_{-5.6}$	0	1	0
HD119483	5073±50	2.95±0.12	0.11±0.04	1.25±0.06	3.67±0.47	5.31±0.47	$2.31^{+0.19}_{-0.17}$	$9.45^{+1.00}_{-0.88}$	$1.69^{+0.09}_{-0.09}$	$0.82^{+0.21}_{-0.17}$	$661.8^{+9.1}_{-16.9}$	0	0.14	0.86
HD120	4999±68	2.84±0.16	-0.32±0.04	1.03±0.11	3.70±0.54	3.69±0.58	$1.38^{+0.10}_{-0.10}$	$6.68^{+0.15}_{-0.14}$	$1.38^{+0.02}_{-0.02}$	$2.74^{+0.79}_{-0.55}$	$507.3^{+1.0}_{-1.1}$	0	1	0
HD120144	4996±52	3.14±0.13	0.23±0.04	1.26±0.08	3.15±0.44	4.96±0.46	$2.42^{+0.06}_{-0.07}$	$7.94^{+0.12}_{-0.11}$	$1.54^{+0.01}_{-0.01}$	$0.71^{+0.05}_{-0.04}$	$523.9^{+1.5}_{-1.3}$	0	1	0
HD120301	5263±115	3.06±0.31	0.03±0.06	1.74±0.35	3.99±0.53	3.66±0.97	$1.83^{+0.10}_{-0.12}$	$7.05^{+0.19}_{-0.18}$	$1.42^{+0.02}_{-0.02}$	$1.37^{+0.28}_{-0.17}$	$504.1^{+2.0}_{-1.6}$	0	1	0
HD122568	5123±50	3.04±0.10	0.05±0.04	1.24±0.05	3.62±0.44	3.72±0.49	$2.38^{+0.06}_{-0.10}$	$7.92^{+0.20}_{-0.17}$	$1.57^{+0.02}_{-0.02}$	$0.68^{+0.07}_{-0.04}$	$526.1^{+2.1}_{-1.5}$	0	0.93	0.07
HD122602	4844±50	2.78±0.11	-0.40±0.04	1.18±0.05	3.50±0.50	4.65±0.52	$1.04^{+0.07}_{-0.07}$	$8.23^{+0.13}_{-0.14}$	$1.50^{+0.01}_{-0.01}$	$6.94^{+1.62}_{-1.30}$	$514.1^{+0.8}_{-0.8}$	0	1	0
HD124461	5102±50	3.08±0.10	0.02±0.04	1.24±0.04	3.50±0.43	4.01±0.45	$1.99^{+0.12}_{-0.09}$	$7.78^{+0.18}_{-0.17}$	$1.50^{+0.01}_{-0.02}$	$1.10^{+0.12}_{-0.15}$	$510.1^{+20.8}_{-3.3}$	0	1	0
HD136350	5160±50	3.09±0.12	-0.05±0.04	1.32±0.05	3.61±0.44	5.20±0.47	$2.35^{+0.06}_{-0.15}$	$7.95^{+0.28}_{-0.22}$	$1.59^{+0.02}_{-0.02}$	$0.67^{+0.11}_{-0.04}$	$527.7^{+3.3}_{-1.9}$	0	0.86	0.14
HD148035	4989±50	3.00±0.11	-0.03±0.04	0.96±0.07	3.39±0.45	4.00±0.46	$1.57^{+0.07}_{-0.09}$	$6.54^{+0.14}_{-0.13}$	$1.34^{+0.02}_{-0.02}$	$2.17^{+0.41}_{-0.29}$	$504.4^{+1.2}_{-1.4}$	0	1	0
HD149649	5163±50	2.93±0.11	0.00±0.04	1.27±0.05	3.91±0.47	5.57±0.48	$2.10^{+0.04}_{-0.05}$	$8.55^{+0.13}_{-0.08}$	$1.61^{+0.01}_{-0.01}$	$0.99^{+0.08}_{-0.08}$	$648.5^{+3.3}_{-3.1}$	0	0.01	0.99
HD151220	4741±72	2.67±0.17	0.22±0.04	1.27±0.12	3.56±0.41	3.96±0.46	$0.97^{+0.02}_{-0.02}$	$10.80^{+0.06}_{-0.04}$	$1.64^{+0.01}_{-0.01}$	$12.66^{+0.67}_{-0.85}$	$664.5^{+1.5}_{-4.2}$	0	0	1

Continued on next page

Starname	$T_{\rm eff}$ (K)	$\log g$ (cgs)	[Fe/H] (dex)	ξ_t (kms^{-1})	$v_{\rm mac}$ (kms^{-1})	$v \sin i$ (kms^{-1})	Mass ($M_\odot$)	Radius ($R_\odot$)	$\log L$ ($L_\odot$)	Age (Gyr)	EEP	$P_{\rm MS}$	$P_{\rm RGB}$	$P_{\rm HB}$
HD155046	5035±81	2.85±0.18	-0.09±0.04	0.54±0.24	3.77±0.56	4.28±0.58	$1.60^{+0.09}_{-0.11}$	$8.07^{+0.14}_{-0.14}$	$1.50^{+0.01}_{-0.01}$	$1.97^{+0.48}_{-0.30}$	$512.1^{+1.1}_{-1.3}$	0	1	0
HD157527	5122±52	2.99±0.13	0.15±0.04	1.30±0.07	3.71±0.47	5.70±0.49	$2.61^{+0.07}_{-0.28}$	$9.28^{+0.44}_{-0.48}$	$1.70^{+0.02}_{-0.02}$	$0.55^{+0.26}_{-0.03}$	$530.8^{+136.6}_{-4.1}$	0	0.56	0.44
HD162157	5115±50	3.01±0.10	0.01±0.04	1.24±0.05	3.65±0.44	5.20±0.45	$2.23^{+0.09}_{-0.17}$	$8.03^{+0.24}_{-0.17}$	$1.57^{+0.01}_{-0.02}$	$0.79^{+0.21}_{-0.06}$	$529.3^{+114.6}_{-2.3}$	0	0.7	0.3
HD162984	5179±50	3.18±0.10	0.07±0.04	1.22±0.05	3.50±0.41	5.17±0.42	$2.29^{+0.05}_{-0.06}$	$7.46^{+0.12}_{-0.12}$	$1.51^{+0.01}_{-0.01}$	$0.76^{+0.04}_{-0.03}$	$523.7^{+1.7}_{-1.3}$	0	1	0
HD16665	4696±56	3.01±0.13	0.20±0.04	1.05±0.10	2.82±0.46	5.01±0.47	$1.25^{+0.11}_{-0.11}$	$5.63^{+0.07}_{-0.07}$	$1.14^{+0.02}_{-0.02}$	$5.62^{+2.13}_{-1.39}$	$499.9^{+1.2}_{-0.7}$	0	1	0
HD167108	5090±50	2.96±0.10	0.02±0.04	1.29±0.05	3.68±0.46	5.46±0.48	$2.09^{+0.05}_{-0.04}$	$8.44^{+0.10}_{-0.12}$	$1.60^{+0.01}_{-0.01}$	$1.00^{+0.06}_{-0.08}$	$645.0^{+3.3}_{-1.7}$	0	0.1	0.9
HD167768	5140±50	2.98±0.12	-0.58±0.06	1.69±0.06	3.76±0.46	4.84±0.52	$1.97^{+0.07}_{-0.07}$	$8.70^{+0.17}_{-0.15}$	$1.70^{+0.02}_{-0.02}$	$0.92^{+0.07}_{-0.10}$	$646.4^{+8.8}_{-8.6}$	0	0.05	0.95
HD167936	5121±57	2.82±0.13	-0.10±0.04	0.34±0.23	4.01±0.51	5.70±0.52	$2.24^{+0.12}_{-0.11}$	$9.38^{+0.52}_{-0.43}$	$1.72^{+0.05}_{-0.04}$	$0.80^{+0.15}_{-0.12}$	$666.0^{+3.8}_{-8.8}$	0	0.02	0.98
HD168839	5099±50	3.08±0.10	0.20±0.04	1.27±0.05	3.49±0.42	5.52±0.43	$2.51^{+0.06}_{-0.34}$	$8.66^{+0.15}_{-0.14}$	$1.62^{+0.01}_{-0.01}$	$0.63^{+0.35}_{-0.03}$	$528.1^{+122.4}_{-1.6}$	0	0.71	0.29
HD170105	5062±50	3.02±0.10	0.04±0.04	1.28±0.04	3.52±0.44	5.78±0.45	$2.12^{+0.05}_{-0.07}$	$8.61^{+0.16}_{-0.12}$	$1.60^{+0.01}_{-0.01}$	$1.03^{+0.09}_{-0.10}$	$646.6^{+4.9}_{-3.0}$	0	0.01	0.99
HD171864	5036±50	2.93±0.10	0.14±0.04	1.24±0.05	3.61±0.46	3.87±0.47	$2.54^{+0.04}_{-0.05}$	$8.48^{+0.12}_{-0.11}$	$1.63^{+0.01}_{-0.01}$	$0.60^{+0.02}_{-0.02}$	$527.1^{+1.2}_{-1.2}$	0	0.98	0.02
HD172039	5116±50	3.10±0.12	0.05±0.04	1.38±0.05	3.50±0.44	5.35±0.46	$1.94^{+0.15}_{-0.07}$	$6.94^{+0.18}_{-0.17}$	$1.41^{+0.02}_{-0.02}$	$1.18^{+0.12}_{-0.19}$	$502.8^{+21.2}_{-1.3}$	0	1	0
HD172642	4922±65	2.95±0.15	0.16±0.04	1.02±0.12	3.34±0.50	4.47±0.64	$1.56^{+0.09}_{-0.09}$	$6.48^{+0.21}_{-0.21}$	$1.30^{+0.03}_{-0.03}$	$2.48^{+0.56}_{-0.40}$	$503.4^{+1.5}_{-1.8}$	0	1	0
HD176771	5204±50	3.13±0.12	0.04±0.04	1.29±0.06	3.66±0.44	5.64±0.46	$2.48^{+0.04}_{-0.06}$	$8.29^{+0.14}_{-0.12}$	$1.62^{+0.01}_{-0.01}$	$0.61^{+0.03}_{-0.02}$	$527.7^{+1.4}_{-1.3}$	0	0.97	0.03
HD176830	5024±53	2.56±0.14	-0.26±0.04	1.28±0.06	4.26±0.57	4.71±0.60	$0.89^{+0.01}_{-0.01}$	$10.35^{+0.07}_{-0.05}$	$1.66^{+0.01}_{-0.00}$	$13.23^{+0.20}_{-0.40}$	$658.9^{+1.7}_{-3.6}$	0	0.01	0.99
HD177057	5109±68	3.02±0.17	0.15±0.04	1.27±0.09	3.62±0.51	4.53±0.55	$2.12^{+0.05}_{-0.04}$	$8.49^{+0.16}_{-0.36}$	$1.57^{+0.02}_{-0.04}$	$1.05^{+0.07}_{-0.08}$	$644.1^{+2.8}_{-111.7}$	0	0.2	0.81
HD179120	5146±50	3.19±0.11	0.17±0.04	1.23±0.05	3.41±0.41	3.90±0.47	$2.43^{+0.05}_{-0.06}$	$7.96^{+0.18}_{-0.18}$	$1.56^{+0.02}_{-0.02}$	$0.69^{+0.04}_{-0.03}$	$524.5^{+1.4}_{-1.4}$	0	0.99	0.01
HD181405	4939±58	2.86±0.17	0.09±0.04	1.60±0.08	3.53±0.54	4.69±0.57	$2.08^{+0.04}_{-0.03}$	$8.24^{+0.29}_{-0.29}$	$1.50^{+0.03}_{-0.03}$	$1.10^{+0.03}_{-0.06}$	$524.7^{+6.8}_{-5.6}$	0	0.93	0.07
HD182393	4975±51	3.01±0.13	-0.10±0.04	1.14±0.07	3.34±0.46	3.06±0.62	$1.75^{+0.11}_{-0.11}$	$7.69^{+0.28}_{-0.26}$	$1.49^{+0.03}_{-0.03}$	$1.47^{+0.33}_{-0.22}$	$509.5^{+1.5}_{-1.6}$	0	1	0

Continued on next page

Starname	T_{eff} (K)	$\log g$ (cgs)	[Fe/H] (dex)	ξ_t (kms^{-1})	v_{mac} (kms^{-1})	$v \sin i$ (kms^{-1})	Mass ($M_\odot$)	Radius ($R_\odot$)	$\log L$ ($L_\odot$)	Age (Gyr)	EEP	P_{MS}	P_{RGB}	P_{HB}
HD18278	4638±89	2.98±0.20	0.43±0.04	1.08±0.17	2.83±0.39	5.36±0.39	$1.28^{+0.08}_{-0.07}$	$6.06^{+0.07}_{-0.07}$	$1.16^{+0.01}_{-0.01}$	$5.82^{+1.30}_{-1.13}$	$501.8^{+0.8}_{-0.6}$	0	1	0
HD183249	4794±50	2.86±0.13	0.09±0.04	1.26±0.07	3.25±0.49	4.84±0.50	$1.16^{+0.07}_{-0.08}$	$6.17^{+0.17}_{-0.16}$	$1.22^{+0.02}_{-0.02}$	$6.80^{+1.67}_{-1.21}$	$503.7^{+1.0}_{-1.1}$	0	1	0
HD18416	4907±65	2.92±0.15	-0.17±0.05	1.14±0.10	3.37±0.51	3.69±0.71	$1.36^{+0.09}_{-0.09}$	$7.73^{+0.17}_{-0.17}$	$1.46^{+0.02}_{-0.02}$	$3.24^{+0.81}_{-0.60}$	$511.4^{+1.0}_{-1.0}$	0	1	0
HD185051	4942±51	3.19±0.12	0.16±0.04	0.95±0.10	2.95±0.41	4.89±0.42	$1.60^{+0.09}_{-0.10}$	$5.20^{+0.12}_{-0.12}$	$1.14^{+0.02}_{-0.02}$	$2.26^{+0.49}_{-0.34}$	$495.0^{+1.8}_{-1.9}$	0	1	0
HD185452	4766±55	2.91±0.15	-0.01±0.04	1.27±0.07	3.11±0.50	2.81±0.65	$1.16^{+0.27}_{-0.16}$	$5.91^{+1.45}_{-1.02}$	$1.21^{+0.20}_{-0.16}$	$6.10^{+4.22}_{-3.09}$	$502.4^{+6.5}_{-5.3}$	0	0.97	0.03
HD185490	5109±50	3.17±0.12	-0.22±0.04	1.09±0.06	3.36±0.42	4.86±0.44	$1.15^{+0.07}_{-0.07}$	$4.88^{+0.15}_{-0.14}$	$1.10^{+0.03}_{-0.03}$	$5.37^{+1.23}_{-0.93}$	$495.7^{+1.2}_{-1.1}$	0	1	0
HD185544	5216±50	3.24±0.10	0.15±0.04	1.17±0.05	3.50±0.40	5.44±0.41	$2.08^{+0.08}_{-0.06}$	$5.98^{+0.15}_{-0.14}$	$1.33^{+0.02}_{-0.02}$	$1.04^{+0.08}_{-0.10}$	$509.6^{+5.2}_{-10.9}$	0	1	0
HD186611	5171±53	3.10±0.13	0.02±0.04	1.09±0.08	3.63±0.45	4.52±0.57	$2.15^{+0.07}_{-0.07}$	$8.78^{+0.15}_{-0.21}$	$1.63^{+0.01}_{-0.02}$	$0.95^{+0.12}_{-0.09}$	$653.2^{+3.0}_{-5.2}$	0	0.01	0.99
HD187562	5065±51	2.66±0.14	-0.61±0.05	1.51±0.07	4.16±0.55	4.34±0.69	$1.52^{+0.11}_{-0.12}$	$8.73^{+0.24}_{-0.23}$	$1.63^{+0.02}_{-0.02}$	$1.77^{+0.51}_{-0.32}$	$520.5^{+1.2}_{-1.4}$	0	0.99	0.01
HD188476	5012±51	2.98±0.12	0.17±0.04	1.24±0.07	3.48±0.47	5.10±0.48	$2.31^{+0.08}_{-0.10}$	$7.85^{+0.13}_{-0.12}$	$1.53^{+0.01}_{-0.01}$	$0.78^{+0.09}_{-0.06}$	$525.5^{+2.8}_{-1.8}$	0	1	0
HD188921	5268±66	2.91±0.16	-0.05±0.04	1.09±0.10	4.22±0.53	5.25±0.62	$2.10^{+0.26}_{-0.05}$	$8.40^{+0.19}_{-0.24}$	$1.61^{+0.02}_{-0.02}$	$0.95^{+0.07}_{-0.28}$	$645.2^{+5.1}_{-115.9}$	0	0.28	0.72
HD189365	5149±50	2.96±0.10	-0.00±0.04	1.25±0.04	3.84±0.45	4.64±0.52	$2.10^{+0.04}_{-0.04}$	$8.52^{+0.06}_{-0.07}$	$1.61^{+0.01}_{-0.01}$	$0.99^{+0.07}_{-0.07}$	$647.5^{+2.2}_{-2.4}$	0	0.01	0.99
HD190122	4944±63	2.93±0.15	0.21±0.04	1.23±0.09	3.41±0.51	4.30±0.54	$2.20^{+0.10}_{-0.10}$	$8.08^{+0.34}_{-0.18}$	$1.53^{+0.03}_{-0.02}$	$0.91^{+0.16}_{-0.10}$	$529.2^{+114.3}_{-3.6}$	0	0.79	0.21
HD190896	4796±75	2.86±0.17	-0.02±0.04	1.08±0.13	3.27±0.55	3.70±0.63	$1.00^{+0.06}_{-0.04}$	$5.51^{+0.10}_{-0.09}$	$1.13^{+0.01}_{-0.01}$	$10.55^{+1.74}_{-1.78}$	$501.5^{+0.8}_{-0.8}$	0	1	0
HD191716	5066±50	3.02±0.10	0.04±0.04	1.29±0.04	3.53±0.44	4.23±0.47	$2.08^{+0.04}_{-0.03}$	$8.34^{+0.10}_{-0.09}$	$1.58^{+0.01}_{-0.01}$	$1.00^{+0.04}_{-0.05}$	$644.1^{+1.0}_{-1.9}$	0	0.14	0.86
HD192232	4974±50	3.10±0.11	-0.30±0.04	0.98±0.07	3.18±0.42	3.27±0.47	$0.91^{+0.03}_{-0.02}$	$5.21^{+0.06}_{-0.07}$	$1.12^{+0.01}_{-0.01}$	$12.24^{+0.88}_{-1.33}$	$500.6^{+0.6}_{-0.7}$	0	1	0
HD193359	4880±50	3.09±0.10	0.02±0.04	1.05±0.06	2.99±0.42	4.82±0.43	$1.03^{+0.06}_{-0.05}$	$5.17^{+0.09}_{-0.08}$	$1.08^{+0.01}_{-0.01}$	$9.80^{+1.72}_{-1.59}$	$499.2^{+0.8}_{-0.7}$	0	1	0
HD193407	4965±50	2.94±0.13	-0.04±0.04	1.61±0.05	3.44±0.47	5.97±0.48	$1.89^{+0.10}_{-0.10}$	$7.72^{+0.14}_{-0.13}$	$1.50^{+0.01}_{-0.01}$	$1.20^{+0.18}_{-0.14}$	$508.6^{+6.2}_{-1.3}$	0	1	0
HD193937	4934±50	3.13±0.10	-0.21±0.04	1.03±0.06	3.04±0.41	3.33±0.43	$1.13^{+0.08}_{-0.07}$	$5.18^{+0.08}_{-0.09}$	$1.14^{+0.01}_{-0.01}$	$5.88^{+1.46}_{-1.17}$	$498.0^{+1.1}_{-1.1}$	0	1	0

Continued on next page

Starname	T_{eff} (K)	$\log g$ (cgs)	[Fe/H] (dex)	ξ_t (kms^{-1})	v_{mac} (kms^{-1})	$v \sin i$ (kms^{-1})	Mass ($M_\odot$)	Radius ($R_\odot$)	$\log L$ ($L_\odot$)	Age (Gyr)	EEP	P_{MS}	P_{RGB}	P_{HB}
HD194536	4975±69	3.10±0.18	-0.03±0.04	1.20±0.10	3.18±0.51	4.23±0.72	$1.73^{+0.11}_{-0.10}$	$7.22^{+0.14}_{-0.14}$	$1.43^{+0.02}_{-0.02}$	$1.57^{+0.30}_{-0.24}$	$506.3^{+1.5}_{-1.6}$	0	1	0
HD194898	5170±59	2.90±0.16	0.12±0.05	1.46±0.09	4.00±0.53	4.28±0.85	$2.16^{+0.28}_{-0.06}$	$8.62^{+0.23}_{-0.16}$	$1.61^{+0.02}_{-0.02}$	$0.96^{+0.10}_{-0.31}$	$648.6^{+6.0}_{-119.7}$	0	0.22	0.78
HD195189	5134±50	2.98±0.12	0.04±0.04	1.33±0.05	3.75±0.47	4.17±0.48	$2.14^{+0.31}_{-0.06}$	$8.48^{+0.11}_{-0.21}$	$1.61^{+0.01}_{-0.01}$	$0.93^{+0.10}_{-0.30}$	$645.6^{+4.0}_{-117.6}$	0	0.38	0.62
HD195326	4866±94	2.79±0.23	0.35±0.04	1.44±0.15	3.58±0.45	5.52±0.46	$1.30^{+0.07}_{-0.08}$	$7.80^{+0.10}_{-0.10}$	$1.36^{+0.01}_{-0.01}$	$5.44^{+1.25}_{-0.89}$	$509.8^{+0.6}_{-0.5}$	0	1	0
HD195899	4921±53	2.95±0.13	-0.02±0.04	1.20±0.07	3.34±0.48	3.85±0.53	$1.60^{+0.08}_{-0.09}$	$7.68^{+0.18}_{-0.17}$	$1.46^{+0.02}_{-0.02}$	$2.03^{+0.41}_{-0.28}$	$509.6^{+1.2}_{-1.4}$	0	1	0
HD195980	4654±57	2.77±0.14	0.18±0.04	1.24±0.08	3.19±0.52	5.15±0.53	$1.41^{+0.08}_{-0.09}$	$8.76^{+0.12}_{-0.12}$	$1.49^{+0.01}_{-0.01}$	$3.64^{+0.84}_{-0.59}$	$514.2^{+0.6}_{-0.7}$	0	1	0
HD196248	5182±63	2.90±0.14	-0.03±0.05	0.99±0.12	4.02±0.51	4.57±0.59	$2.16^{+0.12}_{-0.08}$	$8.75^{+0.36}_{-0.30}$	$1.64^{+0.04}_{-0.03}$	$0.91^{+0.11}_{-0.13}$	$653.9^{+6.4}_{-8.6}$	0	0.11	0.89
HD196997	4983±53	2.68±0.14	0.11±0.04	1.30±0.07	3.95±0.54	4.29±0.59	$2.17^{+0.10}_{-0.10}$	$9.06^{+0.29}_{-0.20}$	$1.64^{+0.03}_{-0.02}$	$1.02^{+0.16}_{-0.15}$	$656.0^{+4.0}_{-4.2}$	0	0	1
HD197254	5159±66	3.24±0.17	0.13±0.05	1.31±0.09	3.35±0.47	5.41±0.53	$2.20^{+0.08}_{-0.08}$	$7.42^{+0.24}_{-0.22}$	$1.48^{+0.03}_{-0.03}$	$0.88^{+0.09}_{-0.07}$	$525.0^{+3.2}_{-3.0}$	0	0.99	0.01
HD197579	5128±50	2.93±0.14	-0.07±0.04	1.44±0.06	3.84±0.50	4.18±0.55	$2.07^{+0.04}_{-0.04}$	$8.41^{+0.14}_{-0.14}$	$1.60^{+0.01}_{-0.01}$	$0.99^{+0.05}_{-0.05}$	$644.8^{+3.2}_{-1.5}$	0	0.02	0.98
HD197790	4989±50	2.97±0.11	-0.31±0.04	1.12±0.05	3.44±0.46	5.12±0.48	$1.60^{+0.09}_{-0.10}$	$7.52^{+0.10}_{-0.11}$	$1.49^{+0.01}_{-0.01}$	$1.73^{+0.37}_{-0.25}$	$511.8^{+0.8}_{-0.9}$	0	1	0
HD199554	4948±51	3.09±0.13	-0.02±0.04	1.23±0.07	3.13±0.44	3.74±0.57	$1.63^{+0.09}_{-0.09}$	$7.16^{+0.16}_{-0.15}$	$1.41^{+0.02}_{-0.02}$	$1.93^{+0.35}_{-0.28}$	$506.8^{+1.4}_{-1.6}$	0	1	0
HD2009	4870±50	2.56±0.12	-0.41±0.04	1.24±0.06	3.94±0.56	3.67±0.72	$1.13^{+0.11}_{-0.10}$	$8.21^{+0.52}_{-0.48}$	$1.51^{+0.05}_{-0.05}$	$5.24^{+1.84}_{-1.34}$	$513.6^{+2.0}_{-1.7}$	0	1	0
HD201013	5098±50	2.95±0.09	0.11±0.04	1.32±0.04	3.73±0.45	5.42±0.47	$2.27^{+0.07}_{-0.07}$	$9.14^{+0.13}_{-0.12}$	$1.66^{+0.01}_{-0.01}$	$0.85^{+0.11}_{-0.08}$	$660.2^{+1.3}_{-3.4}$	0	0.09	0.91
HD201846	5177±75	2.94±0.17	-0.18±0.05	1.13±0.14	3.94±0.54	4.03±0.74	$2.15^{+0.09}_{-0.10}$	$9.09^{+0.32}_{-0.32}$	$1.70^{+0.03}_{-0.03}$	$0.87^{+0.15}_{-0.12}$	$659.8^{+6.7}_{-5.0}$	0	0.01	0.99
HD20186	5269±50	2.92±0.12	-0.02±0.04	1.36±0.05	4.20±0.48	4.78±0.65	$2.11^{+0.26}_{-0.05}$	$8.42^{+0.16}_{-0.21}$	$1.61^{+0.02}_{-0.02}$	$0.93^{+0.07}_{-0.27}$	$645.6^{+4.7}_{-116.5}$	0	0.32	0.68
HD202704	5303±54	2.95±0.13	0.18±0.05	1.29±0.07	4.25±0.49	6.85±0.50	$2.72^{+0.03}_{-0.03}$	$9.13^{+0.17}_{-0.15}$	$1.72^{+0.01}_{-0.01}$	$0.51^{+0.01}_{-0.01}$	$527.4^{+1.6}_{-1.6}$	0	1	0
HD202714	5022±50	3.14±0.10	-0.04±0.04	1.13±0.05	3.21±0.41	4.90±0.42	$1.71^{+0.12}_{-0.11}$	$5.90^{+0.11}_{-0.11}$	$1.28^{+0.02}_{-0.02}$	$1.61^{+0.36}_{-0.28}$	$498.9^{+1.7}_{-1.7}$	0	1	0
HD203086	5252±50	3.02±0.12	0.17±0.04	1.30±0.06	3.99±0.46	4.53±0.48	$2.59^{+0.03}_{-0.03}$	$8.29^{+0.15}_{-0.15}$	$1.64^{+0.01}_{-0.02}$	$0.58^{+0.02}_{-0.01}$	$523.8^{+1.6}_{-1.6}$	0	1	0

Continued on next page

Starname	T_{eff} (K)	$\log g$ (cgs)	[Fe/H] (dex)	ξ_t (kms^{-1})	v_{mac} (kms^{-1})	$v \sin i$ (kms^{-1})	Mass ($M_\odot$)	Radius ($R_\odot$)	$\log L$ ($L_\odot$)	Age (Gyr)	EEP	P_{MS}	P_{RGB}	P_{HB}
HD204649	4931±54	2.75±0.15	0.10±0.04	1.46±0.08	3.72±0.54	4.57±0.60	$2.09^{+0.04}_{-0.04}$	$8.56^{+0.16}_{-0.11}$	$1.57^{+0.01}_{-0.01}$	$1.09^{+0.06}_{-0.07}$	$643.3^{+2.7}_{-6.7}$	0	0.15	0.85
HD205588	5081±50	3.09±0.11	0.21±0.04	1.28±0.06	3.43±0.43	4.36±0.46	$2.56^{+0.04}_{-0.05}$	$8.54^{+0.12}_{-0.12}$	$1.62^{+0.01}_{-0.01}$	$0.61^{+0.03}_{-0.02}$	$526.5^{+1.3}_{-1.2}$	0	0.97	0.03
HD206005	4818±50	2.81±0.11	-0.02±0.04	1.20±0.06	3.39±0.49	5.17±0.49	$1.73^{+0.14}_{-0.11}$	$8.93^{+0.22}_{-0.25}$	$1.58^{+0.01}_{-0.01}$	$1.60^{+0.34}_{-0.31}$	$514.2^{+1.9}_{-1.9}$	0	0.94	0.06
HD206757	4856±61	2.67±0.15	-0.12±0.04	1.13±0.09	3.72±0.56	2.99±0.65	$0.89^{+0.01}_{-0.01}$	$10.27^{+0.06}_{-0.05}$	$1.67^{+0.00}_{-0.00}$	$13.12^{+0.27}_{-0.47}$	$660.8^{+0.7}_{-1.0}$	0	0	1
HD207920	5175±50	3.02±0.10	0.02±0.04	1.29±0.04	3.77±0.44	4.56±0.48	$2.59^{+0.05}_{-0.24}$	$9.13^{+0.25}_{-0.21}$	$1.71^{+0.02}_{-0.02}$	$0.53^{+0.18}_{-0.02}$	$531.5^{+131.2}_{-1.7}$	0	0.8	0.2
HD209154	5207±50	3.27±0.10	-0.00±0.04	1.22±0.05	3.41±0.39	5.62±0.42	$2.26^{+0.04}_{-0.04}$	$6.93^{+0.08}_{-0.08}$	$1.48^{+0.01}_{-0.01}$	$0.77^{+0.03}_{-0.02}$	$520.6^{+1.5}_{-1.2}$	0	1	0
HD210070	4891±60	3.02±0.14	-0.12±0.04	1.06±0.10	3.15±0.48	3.35±0.54	$1.90^{+0.02}_{-0.02}$	$6.79^{+0.11}_{-0.14}$	$1.38^{+0.01}_{-0.01}$	$1.32^{+0.02}_{-0.03}$	$500.3^{+0.6}_{-0.9}$	0	1	0
HD21340	4978±50	3.11±0.11	-0.06±0.04	1.07±0.06	3.17±0.42	5.15±0.43	$1.70^{+0.09}_{-0.09}$	$6.19^{+0.06}_{-0.06}$	$1.32^{+0.01}_{-0.01}$	$1.64^{+0.26}_{-0.21}$	$501.0^{+1.4}_{-1.6}$	0	1	0
HD213986	5037±50	3.03±0.12	0.21±0.04	1.19±0.07	3.44±0.45	4.13±0.46	$2.44^{+0.04}_{-0.07}$	$7.76^{+0.25}_{-0.21}$	$1.54^{+0.01}_{-0.01}$	$0.69^{+0.04}_{-0.02}$	$522.5^{+2.5}_{-2.0}$	0	0.94	0.06
HD214941	4916±63	2.81±0.14	0.05±0.04	0.81±0.14	3.58±0.52	4.99±0.55	$2.36^{+0.07}_{-0.09}$	$9.79^{+0.22}_{-0.20}$	$1.74^{+0.02}_{-0.02}$	$0.75^{+0.11}_{-0.08}$	$668.9^{+0.9}_{-2.8}$	0	0.02	0.98
HD215767	4757±58	2.68±0.15	-0.07±0.04	1.32±0.07	3.52±0.55	3.89±0.57	$1.05^{+0.07}_{-0.06}$	$7.80^{+0.15}_{-0.14}$	$1.40^{+0.02}_{-0.01}$	$8.45^{+1.95}_{-1.57}$	$512.0^{+0.9}_{-0.8}$	0	1	0
HD217053	4879±65	2.73±0.16	-0.27±0.04	1.22±0.08	3.65±0.56	3.76±0.60	$1.11^{+0.07}_{-0.07}$	$8.50^{+0.19}_{-0.18}$	$1.51^{+0.02}_{-0.02}$	$6.13^{+1.44}_{-1.15}$	$514.5^{+0.9}_{-1.0}$	0	1	0
HD217365	4700±68	2.99±0.16	-0.02±0.04	0.97±0.12	2.86±0.50	3.49±0.56	$1.10^{+0.08}_{-0.07}$	$5.36^{+0.09}_{-0.09}$	$1.13^{+0.01}_{-0.01}$	$7.47^{+1.73}_{-1.57}$	$499.7^{+0.9}_{-1.2}$	0	1	0
HD217614	5069±50	3.00±0.10	-0.00±0.05	1.23±0.06	3.56±0.45	6.88±0.48	$2.11^{+0.04}_{-0.05}$	$8.56^{+0.11}_{-0.08}$	$1.61^{+0.01}_{-0.01}$	$0.98^{+0.08}_{-0.08}$	$648.9^{+3.0}_{-2.9}$	0	0.03	0.97
HD218120	4862±50	2.54±0.12	-0.43±0.05	1.28±0.06	3.97±0.56	3.23±0.76	$1.10^{+0.07}_{-0.07}$	$9.23^{+0.23}_{-0.22}$	$1.60^{+0.02}_{-0.02}$	$5.63^{+1.40}_{-1.07}$	$517.6^{+0.9}_{-0.9}$	0	1	0
HD219026	4992±50	2.99±0.10	-0.07±0.04	1.15±0.05	3.42±0.44	3.49±0.48	$1.85^{+0.08}_{-0.10}$	$7.67^{+0.10}_{-0.10}$	$1.49^{+0.01}_{-0.01}$	$1.26^{+0.19}_{-0.12}$	$508.5^{+1.4}_{-1.0}$	0	1	0
HD219263	4672±60	2.70±0.15	0.18±0.04	1.32±0.09	3.39±0.39	3.93±0.40	$1.55^{+0.12}_{-0.13}$	$8.66^{+0.29}_{-0.26}$	$1.50^{+0.01}_{-0.01}$	$2.63^{+0.86}_{-0.59}$	$513.4^{+1.7}_{-2.4}$	0	1	0
HD219775	4829±64	2.91±0.16	0.03±0.04	1.23±0.09	3.22±0.52	3.50±0.56	$2.06^{+0.04}_{-0.03}$	$8.95^{+0.19}_{-0.21}$	$1.56^{+0.01}_{-0.01}$	$1.11^{+0.03}_{-0.05}$	$524.3^{+7.4}_{-5.1}$	0	0.96	0.04
HD220864	4977±50	3.13±0.10	0.12±0.04	1.17±0.06	3.12±0.41	4.96±0.42	$1.74^{+0.09}_{-0.09}$	$5.78^{+0.07}_{-0.07}$	$1.25^{+0.01}_{-0.01}$	$1.67^{+0.27}_{-0.20}$	$496.3^{+1.9}_{-1.8}$	0	1	0

Continued on next page

Starname	T_{eff} (K)	$\log g$ (cgs)	[Fe/H] (dex)	ξ_t (kms^{-1})	v_{mac} (kms^{-1})	$v \sin i$ (kms^{-1})	Mass ($M_\odot$)	Radius ($R_\odot$)	$\log L$ ($L_\odot$)	Age (Gyr)	EEP	P_{MS}	P_{RGB}	P_{HB}
HD221059	4772±64	2.59±0.17	-0.03±0.04	1.33±0.08	3.71±0.59	3.75±0.62	$1.37^{+0.12}_{-0.13}$	$8.71^{+0.18}_{-0.17}$	$1.52^{+0.02}_{-0.02}$	$3.44^{+1.43}_{-0.79}$	$514.8^{+0.9}_{-0.9}$	0	1	0
HD22176	5152±60	2.96±0.15	-0.04±0.04	1.23±0.08	3.84±0.50	4.54±0.68	$2.43^{+0.06}_{-0.08}$	$8.31^{+0.28}_{-0.24}$	$1.64^{+0.03}_{-0.03}$	$0.62^{+0.05}_{-0.03}$	$529.2^{+2.5}_{-1.9}$	0	0.89	0.11
HD221897	4656±66	2.66±0.16	0.13±0.04	1.22±0.10	3.39±0.56	3.60±0.63	$1.24^{+0.09}_{-0.09}$	$8.41^{+0.17}_{-0.15}$	$1.45^{+0.02}_{-0.01}$	$5.51^{+1.63}_{-1.10}$	$512.9^{+0.9}_{-0.8}$	0	1	0
HD221921	5071±59	3.02±0.16	0.10±0.05	1.38±0.10	3.53±0.50	4.23±0.82	$2.13^{+0.05}_{-0.07}$	$8.71^{+0.15}_{-0.14}$	$1.60^{+0.01}_{-0.01}$	$1.05^{+0.09}_{-0.10}$	$647.1^{+4.0}_{-3.2}$	0	0.01	0.99
HD222051	4986±50	3.03±0.13	0.06±0.04	1.25±0.07	3.33±0.46	4.84±0.50	$2.11^{+0.06}_{-0.05}$	$8.57^{+0.21}_{-0.14}$	$1.60^{+0.02}_{-0.02}$	$1.03^{+0.08}_{-0.09}$	$647.1^{+5.5}_{-3.0}$	0	0.01	0.99
HD223619	4923±51	2.87±0.12	-0.07±0.04	1.13±0.07	3.48±0.49	3.63±0.60	$1.22^{+0.08}_{-0.08}$	$6.66^{+0.28}_{-0.26}$	$1.31^{+0.04}_{-0.03}$	$4.93^{+1.24}_{-0.94}$	$505.7^{+1.4}_{-1.3}$	0	1	0
HD223700	5092±50	3.07±0.12	0.19±0.04	1.23±0.06	3.49±0.45	4.13±0.46	$2.43^{+0.04}_{-0.05}$	$7.76^{+0.08}_{-0.08}$	$1.54^{+0.01}_{-0.01}$	$0.69^{+0.03}_{-0.02}$	$523.0^{+1.2}_{-1.1}$	0	1	0
HD224485	4871±63	2.67±0.15	-0.66±0.05	1.16±0.08	3.74±0.56	3.26±0.67	$0.93^{+0.07}_{-0.06}$	$7.83^{+0.15}_{-0.14}$	$1.49^{+0.02}_{-0.02}$	$9.07^{+2.24}_{-2.00}$	$513.8^{+1.2}_{-1.0}$	0	1	0
HD2259	4879±50	3.03±0.11	0.10±0.04	1.08±0.07	3.10±0.44	5.00±0.44	$1.62^{+0.08}_{-0.07}$	$5.94^{+0.06}_{-0.06}$	$1.25^{+0.01}_{-0.01}$	$2.07^{+0.32}_{-0.28}$	$499.6^{+1.5}_{-1.7}$	0	1	0
HD22792	4716±50	2.98±0.10	0.08±0.04	1.08±0.06	2.91±0.44	5.09±0.46	$1.12^{+0.07}_{-0.07}$	$5.88^{+0.06}_{-0.06}$	$1.18^{+0.01}_{-0.01}$	$7.51^{+1.74}_{-1.38}$	$502.6^{+0.6}_{-1.2}$	0	1	0
HD23213	5026±61	2.98±0.14	-0.11±0.04	1.10±0.09	3.51±0.49	4.04±0.59	$1.70^{+0.11}_{-0.10}$	$7.78^{+0.34}_{-0.29}$	$1.49^{+0.04}_{-0.03}$	$1.58^{+0.33}_{-0.25}$	$510.3^{+1.7}_{-1.6}$	0	1	0
HD25872	5045±50	3.03±0.12	0.14±0.04	1.27±0.06	3.46±0.45	3.94±0.51	$2.33^{+0.07}_{-0.09}$	$7.81^{+0.19}_{-0.16}$	$1.53^{+0.02}_{-0.02}$	$0.76^{+0.07}_{-0.04}$	$525.2^{+2.5}_{-1.8}$	0	0.95	0.05
HD26120	5043±50	3.08±0.12	0.22±0.04	1.19±0.07	3.37±0.44	4.29±0.50	$2.51^{+0.08}_{-0.34}$	$8.67^{+0.18}_{-0.16}$	$1.61^{+0.01}_{-0.01}$	$0.64^{+0.36}_{-0.04}$	$527.9^{+123.4}_{-1.8}$	0	0.66	0.34
HD270913	4836±88	3.12±0.20	0.43±0.04	1.10±0.17	2.91±0.38	3.83±0.42	$1.65^{+0.17}_{-0.14}$	$6.30^{+0.17}_{-0.17}$	$1.24^{+0.03}_{-0.03}$	$2.36^{+0.83}_{-0.61}$	$500.0^{+2.4}_{-3.3}$	0	1	0
HD274522	5005±61	3.02±0.15	0.15±0.04	1.29±0.08	3.38±0.49	3.91±0.60	$2.04^{+0.06}_{-0.04}$	$7.17^{+0.19}_{-0.19}$	$1.41^{+0.02}_{-0.02}$	$1.14^{+0.07}_{-0.08}$	$510.5^{+9.4}_{-7.6}$	0	1	0
HD27956	4911±50	3.04±0.09	-0.17±0.04	1.09±0.05	3.15±0.42	4.89±0.44	$1.26^{+0.09}_{-0.08}$	$5.92^{+0.07}_{-0.08}$	$1.25^{+0.01}_{-0.01}$	$4.12^{+1.04}_{-0.75}$	$501.9^{+0.7}_{-0.6}$	0	1	0
HD29821	5078±50	3.29±0.10	0.02±0.04	1.16±0.05	3.06±0.38	4.86±0.39	$1.79^{+0.07}_{-0.10}$	$5.57^{+0.08}_{-0.07}$	$1.24^{+0.01}_{-0.01}$	$1.45^{+0.24}_{-0.14}$	$495.1^{+1.8}_{-1.4}$	0	1	0
HD305357	5182±51	3.19±0.10	-0.05±0.05	1.27±0.06	3.55±0.29	6.92±0.31	$1.91^{+0.20}_{-0.23}$	$5.38^{+1.00}_{-0.90}$	$1.26^{+0.15}_{-0.16}$	$1.19^{+0.50}_{-0.27}$	$494.3^{+22.3}_{-5.6}$	0	1	0
HD3303	4827±50	2.92±0.10	-0.25±0.04	1.09±0.05	3.21±0.46	3.84±0.52	$1.18^{+0.10}_{-0.09}$	$6.76^{+0.17}_{-0.16}$	$1.35^{+0.01}_{-0.01}$	$4.99^{+1.61}_{-1.20}$	$506.5^{+1.5}_{-0.9}$	0	1	0

Continued on next page

Starname	$T_{\rm eff}$ (K)	$\log g$ (cgs)	[Fe/H] (dex)	ξ_t (kms^{-1})	$v_{\rm mac}$ (kms^{-1})	$v \sin i$ (kms^{-1})	Mass ($M_\odot$)	Radius ($R_\odot$)	$\log L$ ($L_\odot$)	Age (Gyr)	EEP	$P_{\rm MS}$	$P_{\rm RGB}$	$P_{\rm HB}$
HD34246	4861±73	2.94±0.18	0.12±0.04	1.25±0.11	3.23±0.54	3.87±0.57	$1.71^{+0.10}_{-0.10}$	$7.73^{+0.14}_{-0.13}$	$1.45^{+0.01}_{-0.01}$	$1.77^{+0.34}_{-0.27}$	$507.6^{+1.6}_{-1.9}$	0	1	0
HD40525	5103±59	2.99±0.16	0.09±0.04	1.37±0.07	3.66±0.50	4.18±0.56	$2.23^{+0.07}_{-0.07}$	$8.92^{+0.14}_{-0.12}$	$1.64^{+0.02}_{-0.01}$	$0.89^{+0.12}_{-0.09}$	$655.9^{+3.3}_{-5.6}$	0	0.14	0.86
HD4145	4710±56	2.99±0.13	0.20±0.04	1.01±0.10	2.87±0.46	5.10±0.47	$1.36^{+0.11}_{-0.11}$	$5.99^{+0.18}_{-0.16}$	$1.21^{+0.01}_{-0.01}$	$4.08^{+1.31}_{-0.95}$	$501.8^{+0.9}_{-1.0}$	0	1	0
HD43375	4701±77	2.83±0.19	0.09±0.04	1.20±0.11	3.16±0.57	4.16±0.62	$1.39^{+0.10}_{-0.12}$	$8.98^{+0.13}_{-0.13}$	$1.52^{+0.01}_{-0.01}$	$3.61^{+1.30}_{-0.74}$	$515.3^{+0.8}_{-0.8}$	0	1	0
HD45616	4994±75	3.06±0.20	0.27±0.04	1.44±0.10	3.30±0.55	3.98±0.59	$2.22^{+0.06}_{-0.10}$	$9.08^{+0.13}_{-0.11}$	$1.62^{+0.01}_{-0.01}$	$1.01^{+0.17}_{-0.10}$	$653.3^{+3.0}_{-3.6}$	0	0.01	0.99
HD4737	5244±50	3.20±0.11	0.07±0.04	1.28±0.05	3.64±0.42	6.00±0.43	$2.58^{+0.03}_{-0.03}$	$8.41^{+0.16}_{-0.15}$	$1.68^{+0.01}_{-0.01}$	$0.56^{+0.01}_{-0.01}$	$525.3^{+1.9}_{-2.1}$	0	1	0
HD4952	5109±86	2.96±0.18	-0.29±0.05	0.81±0.23	3.74±0.56	3.90±0.79	$1.78^{+0.11}_{-0.12}$	$6.58^{+0.31}_{-0.27}$	$1.41^{+0.04}_{-0.04}$	$1.24^{+0.25}_{-0.18}$	$506.6^{+2.5}_{-1.9}$	0	1	0
HD5676	4663±54	2.73±0.13	-0.03±0.04	1.10±0.08	3.28±0.52	5.15±0.53	$1.13^{+0.08}_{-0.07}$	$8.02^{+0.11}_{-0.10}$	$1.43^{+0.01}_{-0.01}$	$6.73^{+1.71}_{-1.30}$	$512.2^{+0.8}_{-0.9}$	0	1	0
HD6019	5083±50	3.05±0.09	-0.46±0.05	1.07±0.06	3.52±0.43	4.33±0.46	$1.45^{+0.09}_{-0.10}$	$6.15^{+0.13}_{-0.12}$	$1.35^{+0.02}_{-0.02}$	$2.18^{+0.55}_{-0.37}$	$506.0^{+1.0}_{-1.2}$	0	1	0
HD6030	5073±50	2.94±0.09	-0.02±0.04	1.16±0.05	3.68±0.45	4.94±0.46	$1.46^{+0.08}_{-0.09}$	$5.22^{+0.13}_{-0.13}$	$1.16^{+0.02}_{-0.02}$	$2.71^{+0.61}_{-0.42}$	$497.5^{+1.0}_{-1.2}$	0	1	0
HD6254	4886±50	2.88±0.10	-0.26±0.04	1.09±0.06	3.39±0.46	4.89±0.49	$1.16^{+0.07}_{-0.07}$	$7.12^{+0.13}_{-0.13}$	$1.39^{+0.01}_{-0.01}$	$5.26^{+1.27}_{-0.96}$	$508.4^{+0.9}_{-0.8}$	0	1	0
HD7039	4913±55	2.99±0.14	-0.02±0.04	1.14±0.08	3.25±0.48	3.31±0.61	$1.47^{+0.10}_{-0.10}$	$6.00^{+0.12}_{-0.11}$	$1.26^{+0.02}_{-0.02}$	$2.72^{+0.66}_{-0.49}$	$502.2^{+0.9}_{-1.3}$	0	1	0
HD71464	5503±50	3.03±0.13	0.00±0.05	1.47±0.06	4.73±0.33	6.19±0.40	$2.50^{+0.04}_{-0.04}$	$8.08^{+0.23}_{-0.24}$	$1.69^{+0.03}_{-0.02}$	$0.59^{+0.02}_{-0.02}$	$519.6^{+2.6}_{-2.7}$	0	1	0
HD71562	5066±65	3.02±0.19	0.33±0.04	1.51±0.10	3.58±0.38	4.28±0.41	$2.34^{+0.07}_{-0.09}$	$7.85^{+0.23}_{-0.21}$	$1.50^{+0.02}_{-0.02}$	$0.82^{+0.09}_{-0.06}$	$524.0^{+2.7}_{-1.9}$	0	0.98	0.02
HD73070	4966±50	3.16±0.10	0.05±0.04	1.12±0.05	3.06±0.40	4.94±0.42	$1.56^{+0.07}_{-0.08}$	$6.14^{+0.10}_{-0.09}$	$1.27^{+0.01}_{-0.01}$	$2.32^{+0.40}_{-0.30}$	$501.9^{+1.3}_{-1.6}$	0	1	0
HD7381	4734±69	2.77±0.17	-0.01±0.04	1.24±0.10	3.31±0.56	3.37±0.66	$1.40^{+0.10}_{-0.10}$	$8.83^{+0.18}_{-0.17}$	$1.53^{+0.02}_{-0.02}$	$3.27^{+0.85}_{-0.63}$	$515.3^{+0.8}_{-0.9}$	0	1	0
HD745	5202±50	3.36±0.10	0.02±0.04	1.15±0.05	3.23±0.37	5.17±0.39	$1.88^{+0.04}_{-0.05}$	$5.02^{+0.07}_{-0.07}$	$1.19^{+0.01}_{-0.01}$	$1.28^{+0.07}_{-0.05}$	$490.0^{+1.2}_{-0.9}$	0	1	0
HD74686	4757±57	2.62±0.14	0.06±0.04	1.16±0.08	3.62±0.55	5.25±0.56	$1.52^{+0.12}_{-0.12}$	$8.10^{+0.35}_{-0.32}$	$1.47^{+0.03}_{-0.03}$	$2.56^{+0.81}_{-0.57}$	$511.8^{+1.7}_{-2.0}$	0	1	0
HD74993	5159±50	3.07±0.11	0.20±0.04	1.25±0.06	3.66±0.44	4.22±0.45	$2.46^{+0.04}_{-0.05}$	$8.09^{+0.13}_{-0.12}$	$1.57^{+0.01}_{-0.01}$	$0.67^{+0.03}_{-0.02}$	$524.9^{+1.2}_{-1.2}$	0	0.99	0.01

Continued on next page

Starname	$T_{\rm eff}$ (K)	$\log g$ (cgs)	[Fe/H] (dex)	ξ_t (kms^{-1})	$v_{\rm mac}$ (kms^{-1})	$v \sin i$ (kms^{-1})	Mass ($M_\odot$)	Radius ($R_\odot$)	$\log L$ ($L_\odot$)	Age (Gyr)	EEP	$P_{\rm MS}$	$P_{\rm RGB}$	$P_{\rm HB}$
HD83674	5082±53	3.28±0.12	-0.00±0.04	1.02±0.08	3.10±0.41	4.17±0.43	$1.93^{+0.05}_{-0.06}$	$6.15^{+0.07}_{-0.07}$	$1.34^{+0.01}_{-0.01}$	$1.16^{+0.09}_{-0.05}$	$498.6^{+1.2}_{-0.9}$	0	1	0
HD84804	4849±54	3.11±0.13	0.24±0.04	1.08±0.09	2.91±0.44	3.61±0.46	$1.47^{+0.08}_{-0.09}$	$5.62^{+0.09}_{-0.10}$	$1.16^{+0.01}_{-0.01}$	$3.19^{+0.75}_{-0.50}$	$499.3^{+0.8}_{-1.3}$	0	1	0
HD85885	4876±73	2.94±0.16	0.04±0.04	0.63±0.22	3.26±0.52	6.01±0.53	$2.61^{+0.05}_{-0.06}$	$9.05^{+0.27}_{-0.28}$	$1.71^{+0.02}_{-0.03}$	$0.53^{+0.03}_{-0.02}$	$530.7^{+1.7}_{-1.6}$	0	0.98	0.02
HD92944	4965±50	2.98±0.10	-0.09±0.04	1.18±0.05	3.37±0.44	5.11±0.47	$1.61^{+0.09}_{-0.09}$	$7.83^{+0.22}_{-0.20}$	$1.48^{+0.02}_{-0.02}$	$1.94^{+0.36}_{-0.27}$	$510.8^{+1.2}_{-1.3}$	0	1	0
HD95624	4867±50	2.95±0.11	-0.31±0.04	1.03±0.07	3.23±0.46	4.87±0.49	$1.36^{+0.10}_{-0.10}$	$7.92^{+0.18}_{-0.18}$	$1.50^{+0.02}_{-0.02}$	$2.94^{+0.77}_{-0.60}$	$513.0^{+1.1}_{-1.3}$	0	1	0
HD9567	5006±108	2.90±0.21	0.23±0.06	1.26±0.17	3.60±0.43	6.54±0.48	$2.12^{+0.03}_{-0.02}$	$8.31^{+0.40}_{-0.32}$	$1.50^{+0.04}_{-0.03}$	$1.10^{+0.02}_{-0.04}$	$535.4^{+101.6}_{-2.9}$	0	0.84	0.16
HD96627	5150±50	3.11±0.11	0.08±0.04	1.27±0.05	3.56±0.43	5.45±0.44	$2.14^{+0.29}_{-0.06}$	$8.49^{+0.12}_{-0.18}$	$1.60^{+0.01}_{-0.01}$	$0.96^{+0.09}_{-0.30}$	$645.4^{+4.5}_{-117.5}$	0	0.34	0.67
HD99005	4770±50	2.77±0.10	-0.29±0.04	1.14±0.05	3.38±0.49	4.87±0.49	$1.00^{+0.06}_{-0.06}$	$7.67^{+0.15}_{-0.15}$	$1.42^{+0.02}_{-0.02}$	$8.92^{+1.90}_{-1.67}$	$512.1^{+0.9}_{-0.9}$	0	1	0
HD99330	4827±75	3.06±0.17	0.30±0.04	1.09±0.12	2.95±0.50	4.92±0.50	$1.34^{+0.09}_{-0.09}$	$5.09^{+0.08}_{-0.08}$	$1.07^{+0.01}_{-0.01}$	$4.56^{+1.15}_{-0.84}$	$496.2^{+0.6}_{-0.6}$	0	1	0
HD99783	5209±50	2.98±0.11	0.14±0.04	1.29±0.05	3.94±0.46	5.75±0.48	$2.68^{+0.03}_{-0.03}$	$8.98^{+0.13}_{-0.14}$	$1.72^{+0.01}_{-0.01}$	$0.52^{+0.01}_{-0.01}$	$526.7^{+1.8}_{-1.9}$	0	1	0
HD99891	5175±50	3.06±0.10	0.11±0.04	1.19±0.05	3.72±0.44	5.53±0.45	$2.51^{+0.04}_{-0.04}$	$8.18^{+0.19}_{-0.18}$	$1.61^{+0.02}_{-0.02}$	$0.61^{+0.02}_{-0.02}$	$525.6^{+1.5}_{-1.5}$	0	1	0
TYC1172-588-1	4847±58	2.75±0.14	-0.14±0.04	1.14±0.09	3.55±0.53	3.64±0.62	$1.01^{+0.07}_{-0.06}$	$5.98^{+0.14}_{-0.14}$	$1.22^{+0.02}_{-0.02}$	$9.09^{+2.10}_{-1.73}$	$503.9^{+1.0}_{-1.0}$	0	1	0
TYC5312-953-1	5107±62	3.05±0.14	-0.06±0.04	0.89±0.12	3.56±0.48	5.89±0.57	$1.74^{+0.11}_{-0.13}$	$5.45^{+0.11}_{-0.10}$	$1.24^{+0.02}_{-0.02}$	$1.50^{+0.40}_{-0.23}$	$495.9^{+1.9}_{-1.7}$	0	1	0
TYC5464-59-1	5281±52	3.14±0.13	-0.03±0.04	1.18±0.06	3.84±0.44	4.25±0.46	$2.03^{+0.07}_{-0.06}$	$6.10^{+0.13}_{-0.12}$	$1.37^{+0.02}_{-0.01}$	$1.01^{+0.07}_{-0.08}$	$512.0^{+4.1}_{-12.1}$	0	1	0
TYC6951-496-1	5061±50	3.02±0.11	0.20±0.04	1.24±0.06	3.51±0.45	4.59±0.47	$2.54^{+0.05}_{-0.09}$	$8.57^{+0.14}_{-0.12}$	$1.62^{+0.01}_{-0.01}$	$0.62^{+0.05}_{-0.02}$	$527.1^{+1.7}_{-1.3}$	0	0.88	0.12
TYC8373-756-1	4947±74	2.81±0.18	-0.14±0.05	1.23±0.10	3.65±0.57	3.32±0.76	$1.45^{+0.09}_{-0.10}$	$8.14^{+0.17}_{-0.15}$	$1.50^{+0.02}_{-0.02}$	$2.65^{+0.67}_{-0.46}$	$513.2^{+0.8}_{-0.9}$	0	1	0
TYC8519-263-1	4642±74	2.85±0.17	0.27±0.04	1.16±0.13	3.02±0.53	3.50±0.57	$1.27^{+0.09}_{-0.09}$	$6.73^{+0.12}_{-0.12}$	$1.26^{+0.01}_{-0.01}$	$5.50^{+1.53}_{-1.13}$	$505.4^{+0.8}_{-0.7}$	0	1	0

Bibliography

Aerts C., 2021, Reviews of Modern Physics, 93, 015001

Alonso A., Arribas S., Martínez-Roger C., 1999, A&AS, 140, 261

Arancibia-Rojas E., Zorotovic M., Vučković M., Bobrick A., Vos J., Piraino-Cerda F., 2024, MNRAS, 527, 11184

Aubrey C., Napiwotzki R., 2023, Bulletin de la Societe Royale des Sciences de Liege, 92, 11190

Barlow B. N., Wade R. A., Liss S. E., Østensen R. H., Van Winckel H., 2012, ApJ, 758, 58

Belkacem K., Goupil M. J., Dupret M. A., Samadi R., Baudin F., Noels A., Mosser B., 2011, A&A, 530, A142

Bianchi L., Herald J., Efremova B., Girardi L., Zabot A., Marigo P., Conti A., Shiao B., 2011, Ap&SS, 335, 161

Bovy J., Rix H.-W., Green G. M., Schlafly E. F., Finkbeiner D. P., 2016, ApJ, 818, 130

Brahm R., Jordán A., Espinoza N., 2017, PASP, 129, 034002

Brewer J. M., Fischer D. A., Valenti J. A., Piskunov N., 2016, ApJS, 225, 32

Brown T. M., Gilliland R. L., Noyes R. W., Ramsey L. W., 1991, ApJ, 368, 599

Brown T. M., Sweigart A. V., Lanz T., Landsman W. B., Hubeny I., 2001, ApJ, 562, 368

Casagrande L. et al., 2016, MNRAS, 455, 987

Castellani M., Castellani V., 1993, ApJ, 407, 649

Castelli F., Kurucz R. L., 2003, in Piskunov N., Weiss W. W., Gray D. F., eds, Modelling of Stellar Atmospheres, Vol. 210, p. A20

Chen X., Han Z., Deca J., Podsiadlowski P., 2013, MNRAS, 434, 186

Choi J., Dotter A., Conroy C., Cantiello M., Paxton B., Johnson B. D., 2016, ApJ, 823, 102

Collier Cameron A. et al., 2007, MNRAS, 380, 1230

Copperwheat C. M., Morales-Rueda L., Marsh T. R., Maxted P. F. L., Heber U., 2011, MNRAS, 415, 1381

Cruzalèbes P. et al., 2019, MNRAS, 490, 3158

Cutispoto G., Messina S., Rodonò M., 2001, A&A, 367, 910

Dawson H. et al., 2024, A&A, 686, A25

D'Cruz N. L., Dorman B., Rood R. T., O'Connell R. W., 1996, ApJ, 466, 359

Deca J. et al., 2012, MNRAS, 421, 2798

dos Santos L. A. et al., 2016, A&A, 592, A156

Dotter A., 2016, ApJS, 222, 8

Downes R. A., 1986, ApJS, 61, 569

Feroz F., Hobson M. P., Bridges M., 2009, MNRAS, 398, 1601

Fontaine G., Brassard P., Charpinet S., Green E. M., Randall S. K., Van Grootel V., 2012, A&A, 539, A12

Gaia Collaboration , 2022, VizieR Online Data Catalog: Gaia DR3 Part 3. Non-single stars (Gaia Collaboration, 2022), VizieR On-line Data Catalog: I/357. Originally published in: Astron. Astrophys., in prep. (2022)

Gaia Collaboration et al., 2018, A&A, 616, A10

Gaia Collaboration et al., 2016, A&A, 595, A1

Gallenne A. et al., 2018, A&A, 616, A68

Gandhi P. et al., 2022, MNRAS, 510, 3885

Geier S., 2013, A&A, 549, A110

Geier S., Heber U., 2012, A&A, 543, A149

Girardi L., 2016, ARA&A, 54, 95

Glagolevskij Y. V., 2019, Astrophysical Bulletin, 74, 66

Gray D. F., 2005, The Observation and Analysis of Stellar Photospheres

Green R. F., Schmidt M., Liebert J., 1986, ApJS, 61, 305

Greenstein J. L., Sargent A. I., 1974, ApJS, 28, 157

Griffin R. F., 1967, ApJ, 148, 465

Günther M. N. et al., 2020, AJ, 159, 60

Gustafsson B., Edvardsson B., Eriksson K., Jørgensen U. G., Nordlund Å., Plez B., 2008, A&A, 486, 951

Hagen H. J., Groote D., Engels D., Reimers D., 1995, A&AS, 111, 195

Han Z., Podsiadlowski P., Maxted P. F. L., Marsh T. R., 2003, MNRAS, 341, 669

Han Z., Podsiadlowski P., Maxted P. F. L., Marsh T. R., Ivanova N., 2002, MNRAS, 336, 449

Heber U., 1986, A&A, 155, 33

Heber U., 2016, PASP, 128, 082001

Heber U., Hunger K., Jonas G., Kudritzki R. P., 1984, in Maeder A., Renzini A., eds, Observational Tests of the Stellar Evolution Theory, Vol. 105, p. 223

Hegedűs V., Mészáros S., Jofré P., Stringfellow G. S., Feuillet D., García-Hernández D. A., Nitschelm C., Zamora O., 2023, A&A, 670, A107

Herrero A., Kudritzki R. P., Vilchez J. M., Kunze D., Butler K., Haser S., 1992, in Heber U., Jeffery C. S., eds, The Atmospheres of Early-Type Stars, Vol. 401. p. 21

Hilditch R. W., 2001, An introduction to close binary stars. Cambridge University Press

Hon M. et al., 2021, ApJ, 919, 131

Horne K., 1986, PASP, 98, 609

Houk N., 1978, Michigan catalogue of two-dimensional spectral types for the HD stars

Howell S. B. et al., 2014, PASP, 126, 398

Humason M. L., Zwicky F., 1947, ApJ, 105, 85

Kjeldsen H., Bedding T. R., 1995, A&A, 293, 87

Lei Z., He R., Németh P., Zou X., Xiao H., Yang Y., Zhao J., 2023, ApJ, 953, 122

Lindegren L. et al., 2018, A&A, 616, A2

Luo Y.-P., Németh P., Liu C., Deng L.-C., Han Z.-W., 2016, ApJ, 818, 202

Markarian B. E., Lipovetsky V. A., Stepanian J. A., Erastova L. K., Shapovalova A. I., 1989, Soobshcheniya Spetsial'noj Astrofizicheskoj Observatorii, 62, 5

Martig M. et al., 2015, MNRAS, 451, 2230

Maxted P. F. L., Heber U., Marsh T. R., North R. C., 2001, MNRAS, 326, 1391

Morton T. D., 2015, isochrones: Stellar model grid package, Astrophysics Source Code Library, record ascl:1503.010

Napiwotzki R. et al., 2001, Astronomische Nachrichten, 322, 411

Napiwotzki R., Karl C. A., Lisker T., Heber U., Christlieb N., Reimers D., Nelemans G., Homeier D., 2004, Ap&SS, 291, 321

Østensen R. H., Van Winckel H., 2012, in Astronomical Society of the Pacific Conference Series, Vol. 452, Kilkenny D., Jeffery C. S., Koen C., eds, Fifth Meeting on Hot Subdwarf Stars and Related Objects, p. 163

Paczynski B., Eggleton P., Mitton S., Whelan J., 1976, in IAU Symp., Vol. 73, p. 75

Pavlovskii K., Ivanova N., 2015, MNRAS, 449, 4415

Paxton B., Bildsten L., Dotter A., Herwig F., Lesaffre P., Timmes F., 2011, ApJS, 192, 3

Pelisoli I., Vos J., Geier S., Schaffenroth V., Baran A. S., 2020, A&A, 642, A180

Popham R., Narayan R., 1991, ApJ, 370, 604

Queloz D. et al., 2001, The Messenger, 105, 1

Recio-Blanco A. et al., 2023, A&A, 674, A29

Ricker G. R. et al., 2015, Journal of Astronomical Telescopes, Instruments, and Systems, 1, 014003

Robin A. C., Reylé C., Derrière S., Picaud S., 2003, A&A, 409, 523

Salaris M., Cassisi S., Schiavon R. P., Pietrinferni A., 2018, A&A, 612, A68

Sargent W. L. W., Searle L., 1968, ApJ, 152, 443

Schaffenroth V., Pelisoli I., Barlow B. N., Geier S., Kupfer T., 2022, A&A, 666, A182

Setiawan J., Pasquini L., da Silva L., Hatzes A. P., von der Lühe O., Girardi L., de Medeiros J. R., Guenther E., 2004, A&A, 421, 241

Sneden C., Bean J., Ivans I., Lucatello S., Sobeck J., 2012, MOOG: LTE line analysis and spectrum synthesis, Astrophysics Source Code Library, record ascl:1202.009

Soto M. G., Jenkins J. S., 2018, A&A, 615, A76

Soto M. G., Jones M. I., Jenkins J. S., 2021, A&A, 647, A157

Stark M. A., Wade R. A., 2003, AJ, 126, 1455

Stassun K. G., Torres G., 2018, ApJ, 862, 61

Stepanian J. A., 2005, Revista Mexicana de Astronomía y Astrofísica„ 41, 155

Sweigart A. V., 1997, ApJ, 474, L23

Sweigart A. V., Brown T. M., Lanz T., Landsman W. B., Hubeny I., 2002, in Astronomical Society of the Pacific Conference Series, Vol. 265, van Leeuwen F., Hughes J. D., Piotto G., eds, Omega Centauri, A Unique Window into Astrophysics, p. 261

Taylor J. H., Fowler L. A., McCulloch P. M., 1979, Nature, 277, 437

Taylor M. B., 2005, in Astronomical Society of the Pacific Conference Series, Vol. 347, Shopbell P., Britton M., Ebert R., eds, Astronomical Data Analysis Software and Systems XIV, p. 29

Tkachenko A. et al., 2020, A&A, 637, A60

Ulrich R. K., 1986, ApJ, 306, L37

Uzundag M., Jones M. I., Vučković M., Vos J., Bobrick A., Paladini C., 2022, A&A, 668, A89

Valle G., Dell'Omodarme M., Prada Moroni P. G., Degl'Innocenti S., 2024, arXiv e-prints, arXiv:2408.14900

van Leeuwen F., 2007, A&A, 474, 653

Vos J., Bobrick A., Vučković M., 2020, A&A, 641, A163

Vos J., Németh P., Vučković M., Østensen R., Parsons S., 2018, MNRAS, 473, 693

Vos J., Östensen R., Van Winckel H., 2014, in Astronomical Society of the Pacific Conference Series, Vol. 481, van Grootel V., Green E., Fontaine G., Charpinet S., eds, 6th Meeting on Hot Subdwarf Stars and Related Objects, p. 265

Vos J. et al., 2012, A&A, 548, A6

Vos J., Østensen R. H., Marchant P., Van Winckel H., 2015, A&A, 579, A49

Vos J., Østensen R. H., Németh P., Green E. M., Heber U., Van Winckel H., 2013, A&A, 559, A54

Vos J., Østensen R. H., Vučković M., Van Winckel H., 2017, A&A, 605, A109

Vos J., Vučković M., Chen X., Han Z., Boudreaux T., Barlow B. N., Østensen R., Németh P., 2019, MNRAS, 482, 4592

Warfield J. T. et al., 2021, AJ, 161, 100

Webbink R. F., 1984, ApJ, 277, 355

Wisotzki L., Koehler T., Groote D., Reimers D., 1996, A&AS, 115, 227

Wright E. L. et al., 2010, AJ, 140, 1868

Yu J., Hekker S., Bedding T. R., Stello D., Huber D., Gizon L., Khanna S., Bi S., 2021, MNRAS, 501, 5135

Yu J., Khanna S., Themessl N., Hekker S., Dréau G., Gizon L., Bi S., 2023, ApJS, 264, 41

Zhou J. et al., 2024, ApJS, 271, 17